INSTITUTO SUPERIOR DE ENGENHARIA DO PORTO
MESTRADO EM ENGENHARIA MECÂNICA




OTIMIZACAO ESTRUTURAL DE UMA BIELA DE MOTOR UTILIZANDO METODOS DE OTIMIZACAO TOPOLOGICA SEM MALHA

JOÃO TIAGO TOMÁS OLIVEIRA
outubro de 2025

POLITÉCNICO
DO PORTO

ISEP INSTITUTO SUPERIOR DE ENGENHARIA DO PORTO

STRUCTURAL OPTIMIZATION OF AN ENGINE ROD USING A MESHLESS METHOD TOPOLOGY OPTIMIZATION FRAMWORK

João Tiago Tomás Oliveira

Dissertation to fulfil the requirements to obtain the Master degree in Mechanical Engineering, with a specialization in Mechanical Constructions

Supervisor: Professor Doutor Jorge Américo de Oliveira Pinto Belinha
Co-supervisor: Professor Doutor Daniel do Espírito Santo Rodrigues

Jury:
President: Professor Doutor Hernâni Miguel Reis Lopes
Examiner: Doutor Luís Daniel Costa Ramalho
Supervisor: Professor Doutor Jorge Américo de Oliveira Pinto Belinha

Porto, September 2025

Abstract

In recent years, meshless methods have gained significant attention in the scientific community, undergoing substantial methodological advancements. These methods have emerged as a promising alternative to traditional finite element methods, particularly for problems involving complex geometries and large deformations. They address some of the shortcomings of the Finite Element Method approach (FEM), such as mesh dependency and difficulties in handling severe mesh distortion. This dissertation investigates the potential of combining meshless methods with topology optimization techniques for the design of lightweight and efficient structural components. The study focuses on two specific formulations, the Radial Point Interpolation Method (RPIM) and the Natural Neighbour Radial Point Interpolation Method (NNRPIM) combined with a Bi-directional Evolutionary Structural Optimization (BESO) algorithm, which are compared against FEM. First, benchmark examples were addressed, allowing to understand the performance and reliability of the meshless methods formulations. Then, an engine rod was analysed and structurally optimized using the meshless topology optimization framework. The results show that meshless methods are capable of producing optimized results very close with the FEM, permitting to consider meshless methods an alternative technique to FEM.

KEYWORDS: Finite Element Method; Meshless Methods; Structural Optimization; Radial Point Interpolation Method (RPIM); Natural Neighbour Radial Point Interpolation Method (NNRPIM)

Resumo

Nos últimos anos, os métodos sem malha têm ganho atenção significativa na comunidade científica, passando por avanços substanciais. Estes métodos surgiram como uma alternativa promissora aos métodos tradicionais dos elementos finitos, particularmente para problemas que envolvem geometrias complexas e grandes deformações. Estes métodos corrigem algumas das limitações do Método dos Elementos Finitos (FEM), como a dependência da malha e as dificuldades em lidar com grandes distorções de malha. Esta dissertação investiga o potencial da combinação de métodos sem malha com técnicas de otimização topológica para o projeto de componentes estruturais leves e eficientes. O estudo concentra-se em duas formulações específicas, o Radial Point Interpolation Method (RPIM) e o Natural Neighbour Radial Point Interpolation Method (NNRPIM) combinados com um algoritmo Bi-directional Evolutionary Structural Optimization (BESO), que são comparados com o FEM. Primeiro foram abordados exemplos de referência, que permitem compreender o desempenho e a fiabilidade das formulações dos métodos sem malha. De seguida, foi analisado uma biela de um motor foi analisada e otimizada estruturalmente utilizando métodos de otimização topológica combinados com métodos sem malha. Os resultados mostram que os métodos sem malha são capazes de produzir resultados otimizados muito próximos dos obtidos com o FEM, permitindo considerá-los como uma técnica alternativa ao FEM.

PALAVRAS-CHAVE: Método de Elementos Finitos, Métodos sem Malha, Otimização Estrutural, Radial Point Interpolation Method (RPIM); Natural Neighbour Radial Point Method (NNRPIM)

Index

Figures Index

Tables Index

Acronyms and Symbols

Acronyms

AESO	Additive Evolutionary Structural Optimization
BESO	Bi-directional Evolutionary Structural Optimization
DR	Decrease Ratio
EFGM	Element Free Galerkin Method
ESO	Evolutionary Structural Optimization
FE	Finite Element
FEM	Finite Element Method
FEMAP	Finite Element Modelling And Postprocessing
FEMAS	Finite Element and Meshless Analysis Software
GAs	Genetic Algorithms
MLPG	Meshless Local Petrov-Galerkin method
MLS	Moving Least Squares
MM	Meshless Method
MQ-RBF	Multiquadratic Radial Basis Function
NN	Natural Neighbour
NNRPIM	Natural Neighbour Radial Point Interpolation Method
PCM	Point Collocation Method
PDEs	Partial Differential Equations
PIM	Point Interpolation Method
RBF	Radial Basis Function
RKPM	Reproducing Kernel Particle Method
RPI	Radial Point Interpolation
RPIM	Radial Point Interpolation Method
SED	Strain Energy Density
SIMP	Solid Isotropic Material with Penalization
SPH	Smooth Particle Hydrodynamics
VM	Von Mises

Symbols

$(r_{ij})_{\xi}$	$\Phi_{\xi}(\mathbf{x}_I)$ MQ-RBF partial derivatives
$\tilde{\sigma}_e^{vm}$	Von Mises stress approximation for void elements
$\widehat{\omega}_1$	Cartesian integration weight
Γ_t	Natural boundaries

Γ_u	Essential boundaries
$\Phi_\xi(\mathbf{x}_I)$	Interpolation function for general direction ξ
$\bar{\mathbf{t}}$	External forces vector
$\mathbf{u}_s$	Vector of the nodal parameters
A_Ω	Domains's area
A_{cel}	Integration cell area
A_{iso}	Isoparametric cell area
E_i	Young modulus in material direction i
G_{ij}	Elastic shear modulus in distortion plane O_{ij}
V_i	Voronoï cell
W_{ext}	Work done by external forces
W_{int}	Work done by internal forces
$a_i(\mathbf{x}_I)$	RBF coefficient
$b_j(\mathbf{x}_I)$	PBF coefficient
c_{er}	Evolutionary rate
c_{rr}	Rejection ratio
$\boldsymbol{f}_b$	Global body vector
$\boldsymbol{f}_t$	External force vector
ν_{ij}	Poisson's ratio in distortion plane O_{ij}
σ_e^{vm}	Element von Mises stress
σ_{max}^{vm}	Critical or maximum von Mises stress
$\Phi(x_I)$	Interpolation function
Ω	Domain
$\mathbf{B}(\boldsymbol{x}_I)$	Deformation matrix
$\mathbf{P}$	Polynomial basis matrix
$\mathbf{R}$	RBF matrix
$\mathbf{b}$	Body forces vector
$\mathbf{p}(\mathbf{x}_I)$	Polynomial basis function
$\mathbf{r}(\mathbf{x}_I)$	Radial basis function
V	Voronoï diagram
c	MQ-RBF shape parameter
m	Number of monomials
p	MQ-RBF shape parameter
$u(x)$	Field function
$\boldsymbol{K}$	Global stiffness matrix
$\boldsymbol{c}$	Material constitutive matrix

$\boldsymbol{u}$	Global displacement field
$\varepsilon(\boldsymbol{x}_l)$	Deformation vector
$\boldsymbol{\sigma}$	Stress

1. Introduction

1.1. Contextualization and Background

The rapid advancement of simulation techniques has revolutionized the way complex problems and understood and solved. Methods such has Finite Element Method (FEM), and Meshless Methods (MM) have emerged as powerful tools for addressing challenges across a variety of fields and industries. These methods help predicting the behaviour of complex systems allowing engineers to make more informed decisions leading to more efficient and better solutions, which would be unfeasible in the past. While these methods are important and powerful tools on their own, their potential is maximized when paired with topology optimization techniques. Topology optimization plays a critical role by generating optimal designs based on specific performance criteria, minimizing material use while maintaining structural integrity. When paired with meshless methods, this process becomes even more powerful, providing engineers with the freedom to push the boundaries of conventional design. Topology Optimization is a shape optimization technique that finds the optimal solution for a given set of loads, restraints and conditions. This technique removes redundant material, resulting in a geometry that meets all structural requirements but with less material. However, these resulting geometries are often very complex with organic shapes that are very difficult to manufacture. Due to advancements in manufacturing technologies, such as 3D printing, it is now possible to create complex and organic geometries that push the boundaries of the optimal design.

1.2. Motivation

The growing demand for lightweight, high-performance structures has placed a spotlight on topology optimization as a critical tool in structural design. Traditional optimization techniques, often paired with FEM, face significant limitations in generating and analysing highly complex organic geometries. These limitations become particularly evident when applied to additive manufacturing, which thrives on the ability to fabricate intricate designs.

Meshless methods, with their inherent flexibility and adaptability, present a unique opportunity to overcome these challenges. By integrating meshless techniques with topology optimization, this research aims to unlock the full potential of additive manufacturing, paving the way for innovative designs and efficient material usage. Furthermore, reducing material consumption not only decreases production costs but also has a significant positive impact on the environment, aligning with the growing need for sustainable and resource-conscious engineering practices.

1.3. Objectives

The primary goal of this dissertation is to evaluate the applicability and performance of meshless methods, comparing them to the well-established Finite Element Method (FEM). The study aims to:

- Validate the accuracy and convergence behaviour of FEM, RPIM, and NNRPIM through benchmark problems.
- Investigate the influence of parameters such as mesh density and decrease ratio on the optimization results.
- Investigate the influence of parameters such as mesh density and decrease ratio on the optimization results.
- Apply the method to a practical engineering case study and evaluate its potential in real-world applications.

1.4. Structure

The present dissertation is split into five different chapters: Introduction, Meshless Methods, Structural Optimization, Numerical Applications and Conclusions.

In Chapter 1, Introduction, a brief description of the theme is given as well as the motivation behind it and its objectives.

Chapter 2, Meshless Methods, provides a review of the state of the art of meshless methods and its history and development, focusing on the theoretical foundations and practical implementation of the Radial Point Interpolation Method (RPIM) and the Natural Neighbour Radial Point Interpolation Method (NNRPIM). The general procedure of meshless methods is explained. Then, the fundamental concepts and mathematical formulations are presented for RPIM and NNRPIM.

Chapter 3, Structural Optimization, delves into structural optimization techniques, firstly a state of the art is presented, then an overview is provided of different methods, such as the Evolutionary Structural Optimization (ESO) method, the Bi-directional Evolutionary Structural Optimization (BESO), and the Solid Isotropic Material with Penalization (SIMP) method.

Chapter 4, Numerical Applications, contains the practical work developed in this dissertation. This chapter begins with a convergence study to validate the accuracy of the numerical methods and then, benchmark problems from the literature are then addressed to compare the results obtained with the different methods against reference solutions. Finally, the methodology is extended to an industrially relevant case study.

Chapter 5, Conclusions, summarizes the main results of the work, highlighting the general findings and remarks. It also discusses the limitations encountered during the study and outlines directions for future research, with emphasis on the potential of meshless methods in structural optimization and their integration with advanced optimization techniques and manufacturing processes.

2. Meshless Methods

This chapter provides a review of meshless methods. It begins by outlining the historical development of these methods. The introductory concepts underlying the formulation of RPIM and NNRPIM are then introduced. Key aspects, including numerical integration, nodal connectivity, and shape function construction, are described.

2.1. Introduction to Meshless Methods

Meshless methods have been a focus of interest in recent years, especially in the engineering community. Searching in the database "Web of Knowledge" [1] for the keywork "meshless methods" allows to obtain Figure 1, which illustrates the increasing trend in the number of publications per year. Meshless methods can overcome some of FEM shortcomings like the high cost in creating the mesh, low accuracy of the stress field, difficulty in adaptive analysis, limitation in the analyses of some non-linear problems (such as domains under large deformations and fracture analyses). Meshless methods use a set of nodes scattered within the problem domain to represent the problem domain and its boundaries; these nodes do not form a mesh meaning it is not required any pre information about the relationship between themselves.

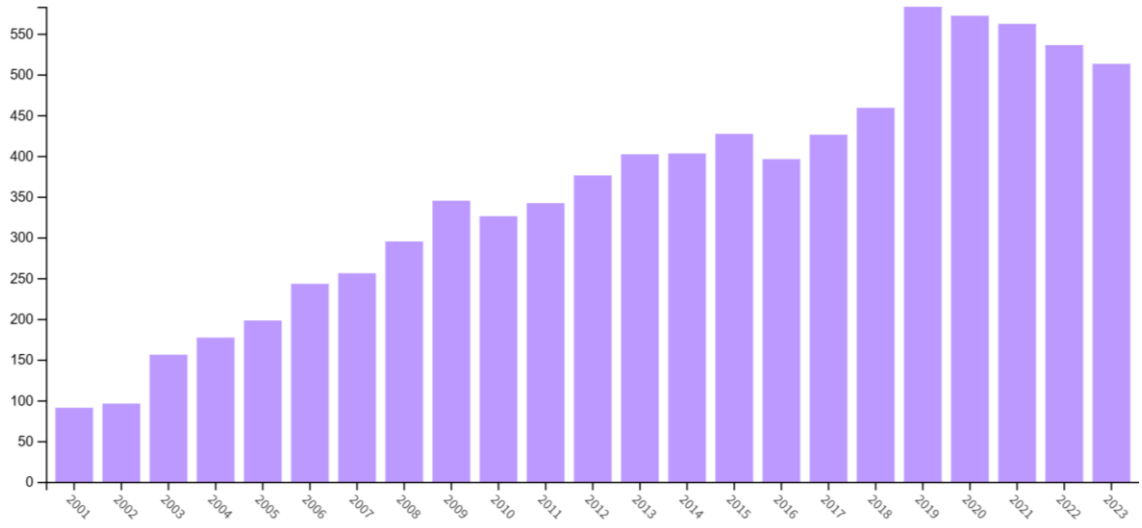

Figure 1 - Number of publications per year on meshless methods [1]

Meshless methods can be categorized into two primary categories based on their treatment of governing equations, there are strong form methods that solve partial equations (PDEs) directly

obtaining the exact solution, unfortunately it is very difficult to solve for practical engineering problems that are by nature highly complex. The weak form methods in contrast to the strong form, employ variational principles to approximate PDE solutions producing robust and accurate results, particularly for complex boundary conditions.

Meshless methods can be traced back to 1977 when Lucy [2] and Gingold and Monaghan [3] proposed a Smooth Particle Hydrodynamics (SPH) method that was used for modelling astrophysical phenomena without boundaries, such as exploding stars and dust clouds [4]. This method did not attract much attention has it was not able to consistently satisfy the conditions for many problems. An appealing feature of this method is its adaptive nature which helps it to prevent SPH formulation from the random distribution of particles and also that helps handling large deformation problems [5]. This method was later further developed and served as a basis for other meshless methods. The Element Free Galerkin method (EFGM) [6] was developed in the 1990s to overcome different problems with multiple meshless methods, especially around boundaries. It used the Moving Least Squares (MLS) approach to improve accuracy and flexibility, gaining popularity for solving solid mechanics problems, including those with large deformations and crack propagation. For solid mechanics problems, some of the SPH numerical problems were identified and corrected, and a correction function was proposed to overcome inconsistency problems originating in a more stable method known as Reproducing Kernel Particle Method (RKPM) [5]. Radial Basis Function (RBF) Method proposed by Kansa [7], [8] in 1991 introduced a simple and accurate way to solve partial differential equations (PDEs) with fast convergence and high adaptability to problems with complex geometries. Meshless Local Petrov-Galerkin (MLPG) Method introduced by Atluri and Zhu [9] in 1998 eliminated the need for background cells and of numerical integration, allowed greater flexibility in selecting trial and test functions. Point Collocation Method (PCM) [10] developed based on reproducing kernel approximation offers inherent multi-resolution capability for error estimation and simplified boundary condition implementation. Its ease of use made it a practical choice for various fluid flow and solid mechanics problems.

2.2. Radial Point Interpolation Method (RPIM)

The RPIM [11] originated from the Point Interpolation Method (PIM) [12], a technique that consisted in constructing polynomial interpolants based only on a group of arbitrarily distributed points. A key feature of PIM is its ability to satisfy the Kronecker delta property, which simplifies the enforcement of essential boundary conditions. However, this technique possesses certain numerical issues, for instance the perfect alignment of nodes produces singular solutions in the interpolation function construction.

To overcome these issues, radial basis functions (RBFs) were incorporated in PIM, resulting in the RPIM. Unlike polynomial PIM, RPIM provides greater stability and flexibility when dealing with arbitrary and irregular nodal distributions. It effectively addresses the singularity problem associated with polynomial interpolants and facilitates the construction of shape functions for three-dimensional domains [13].

RPIM employs the concept of an influence domain to establish nodal connectivity. This approach ensures that each node interacts with its neighbours within a defined radius or domain, enhancing the accuracy of the interpolation. Additionally, RPIM uses a nodal independent background integration mesh for numerical integration, ensuring compatibility with various problem geometries while maintaining computational efficiency. The use of this background mesh contradicts the concept of "pure" meshless methods, meaning that this method is not considered a true meshless method.

2.3. Natural Neighbour Radial Point Interpolation Method (NNRPIM)

The Natural Neighbour Radial Point Interpolation Method (NNRPIM) [14] is the product of the combination of the Radial Point Interpolation (RPI) with the natural neighbour's geometric concept. In this method the "influence domain" is replaced with the "influence cell" concept, to obtain the influence-cells the NNRPIM relies on geometrical and mathematical constructions such as the Voronoï diagrams [15] and the Delaunay tessellation [16]. By employing Voronoï cells, a set of influence cells is generated based on an unstructured distribution of nodes. The Delaunay triangles, which are the duals of the Voronoi cells, are used to create a node-dependent background mesh for the numerical integration of the NNRPIM interpolation functions. Since the integration mesh is entirely dependent on the nodal distribution, NNRPIM can be regarded as a truly meshless method.

2.4. Standard Meshless Method Procedure

Most meshless methods follow a standard sequence of steps; the first one is representing the problem's domain and its boundary using sets of nodes scattered in the problem domain and its boundary. These nodes, often called field nodes, carry the values of the field variables. The nodal discretization can follow either a regular or irregular pattern, as shown in Figure 2. The performance of the method depends on the density of the nodal discretization; a fine nodal discretization leads to more accurate results at the cost of more computational power required. As a good practice, locations with domain discontinuities where stress concentrations are expected should have a higher nodal density to ensure good result accuracy.

The second step is the function interpolation/approximation, since there is no mesh, the field variable at any point within the problem domain is interpolated using function values at field nodes within a small local support domain [17]. For this purpose, a background mesh is constructed nodal dependent or independent, nevertheless the integration mesh has to match the size of the domain [6].

For numerical integration, different integration meshes can be used, a common approach is the Gauss-Legendre integration mesh, as in used in FEM. A different way to integrate weak form equations is the use of nodal integration, which resorts to Voronoï diagrams to obtain the integration weight on each node. Using nodal integration usually leads to a decrease in accuracy, making it necessary to implement a stabilization mesh and therefore increasing computational cost.

Having the nodal distribution defined and the integration mesh constructed, it is possible to proceed to the next step by imposing the nodal connectivity. There are several approaches used in meshless methods to impose nodal connectivity, influence domains are commonly used in methods like RPIM, and influence cells are used in NNRPIM. Afterward the system equations are formed; the discrete equations of a Meshless Method can be formulated using the shape functions and strong or weak form system equation.

The final step is solving the global system of equations. This involves employing numerical techniques to compute the solution for the field variables, completing the meshless method procedure.

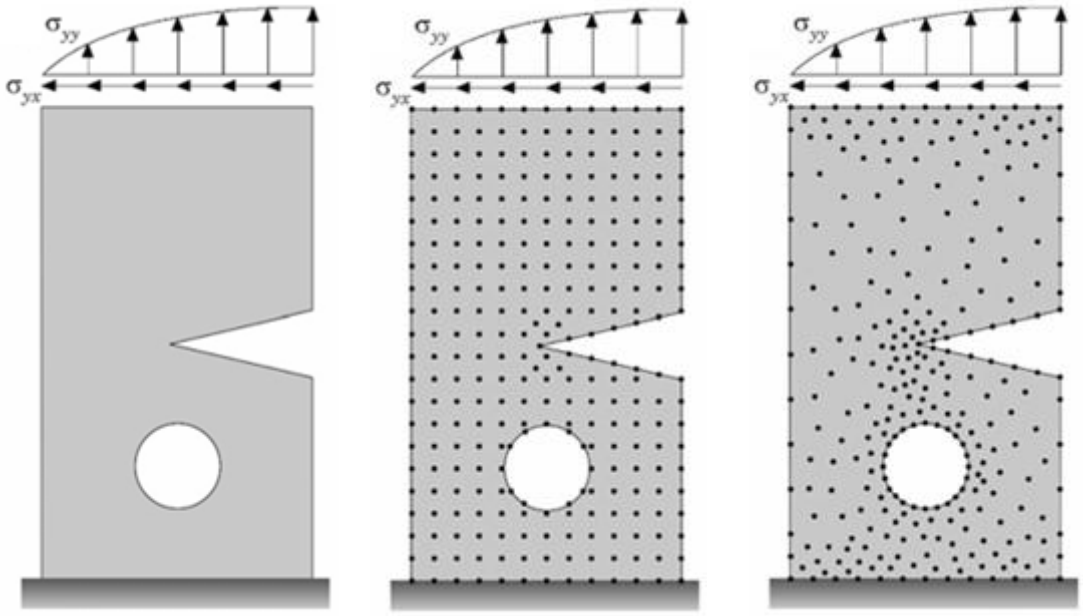

Figure 2- a) Solid domain b) Regular nodal discretization c) Irregular nodal discretization [18]

2.5. Nodal Connectivity

Nodal connectivity is an important step in meshless methods, it defines the relationships between nodes across the problem domain. Unlike the finite element method, which relies on element-based connectivity, meshless methods establish connectivity through concepts like influence domains, influence cells, and natural neighbours. This subchapter explores the nodal connectivity approaches used in the Radial Point Interpolation Method (RPIM) and the Natural Neighbour Radial Point Interpolation Method (NNRPIM).

2.5.1. RPIM Nodal Connectivity

In the Radial Point Interpolation Method (RPIM), nodal connectivity is established through the influence domain concept, where the nodal connectivity is obtained by the overlap of the

influence domain of each node. The size and shape of these influence domains play a crucial role in the performance and results of the meshless method. Ideally all influence domains should contain the same number of nodes.

Influence domains can be constructed one of two ways, shown in Figure 3. Either by a fixed number of neighbouring nodes or a fixed area around each node. Each method has its own implications and distinct trade-offs, depending on the problem being addressed.

Using a fixed number of neighbouring nodes, as shown in Figure 3 (c), ensures that every influence domain contains the same number of nodes, providing consistent interpolation order throughout the domain, however, it can result in irregularly shaped and sized influence domains in areas with uneven nodal distribution, these inconsistencies may compromise the uniformity of the interpolation process.

The other approach is using a fixed influence area, as is shown in Figure 3 (a) and (b). In this approach, a fixed area from each node is defined, and all nodes within this radius are considered part of the influence domain. It produces more regular and predictable influence domains, especially useful in cases with highly variable nodal densities, but can result in different influence domains containing a different number of nodes, especially in sparsely populated regions.

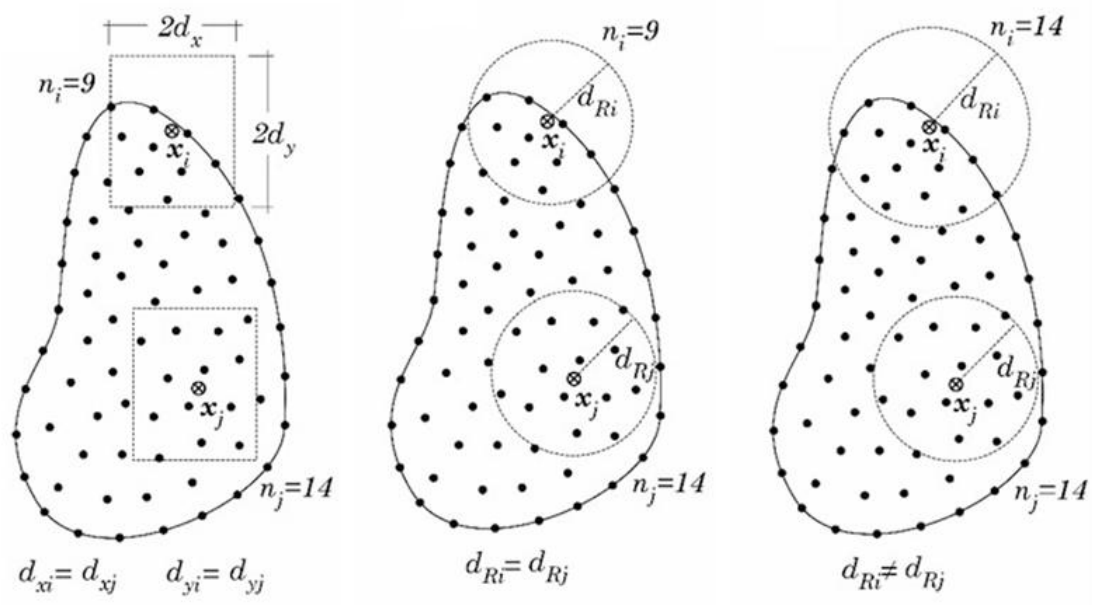

Figure 3 - (a) Fixed rectangular shaped influence-domain. (b) Fixed circular shaped influence-domain. (c) Flexible circular shaped influence-domain [18]

2.5.2. NNRPIM Nodal Connectivity

To obtain the influence-cells the NNRPIM relies on geometrical and mathematical constructions such as the Voronoï diagrams [15] and the Delaunay tessellation [16].

Consider a space domain Ω discretized by the nodal set $\boldsymbol{N} = \{n_1, n_2, \dots, n_N\}$, the Voronoï diagram $\boldsymbol{V}$, of $\boldsymbol{N}$ is formed by a set of sub-regions V_i, each sub-region is associated to a respective node, and each node n_i will have its respective sub-region V_i, hence, the Voronoï diagram is defined by $\boldsymbol{V} = \{V_1, V_2, \dots, V_N\}$. Any point in the interior of V_i is closer to the node n_i than any other node belonging to the domain. The Voronoï cells does not overlap or leave gaps between each other, meaning that the sum of the volume of all Voronoï cells is equal to the total volume of the domain:

$$\Omega = \sum_{i=1}^{N} V_i \therefore \boldsymbol{V} = \Omega \tag{2.1}$$

The nodal connectivity is established by the natural neighbour concept, the natural neighbours of each cell $\boldsymbol{x}_i$ are the other cells that share edges (2D) or faces (3D) with the cell $\boldsymbol{x}_i$. There are two kinds of influence cells, first degree influence cells and second-degree influence cells. First-degree influence cells are formed by cell $\boldsymbol{x}_i$ and its natural neighbours. Second-degree influence cells are formed by the same way as the first-degree influence cells plus the natural neighbours of the natural neighbours of the cell. Both types of influence cells can be visualized in Figure 4, highlighting their construction and spatial relationships.

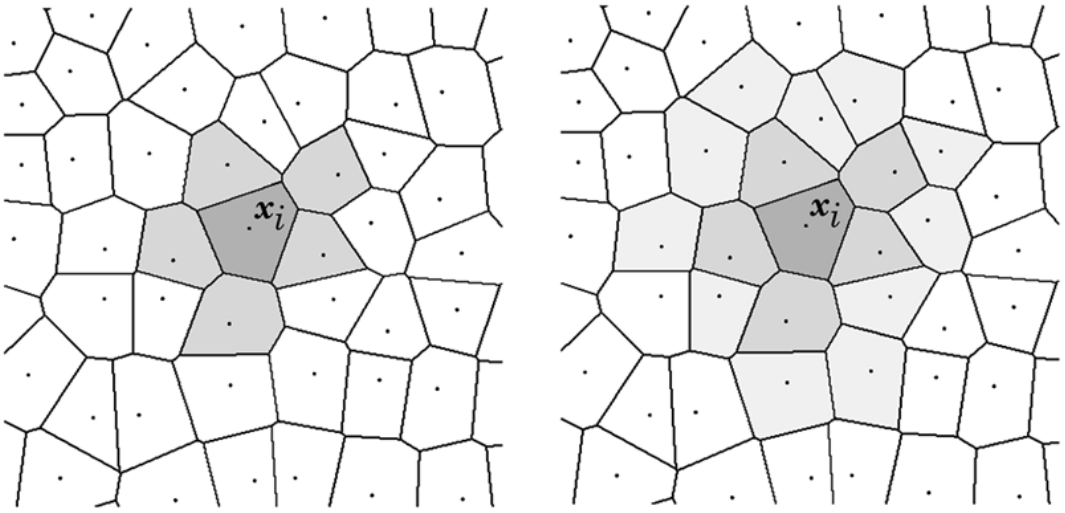

(a) (b)

Figure 4 - Voronoï diagram of a given nodal discretisation. (a) First-degree influence cell. (b) second-degree influence cell [19]

2.6. Numerical Integration

This subchapter looks at the numerical integration approaches used in the Radial Point Interpolation Method (RPIM) and in the Natural Neighbour Radial Point Interpolation Method (NNRPIM).

2.6.1. RPIM Integration

The classic formulation of the Radial Point Interpolation Method (RPIM) employs the Gauss–Legendre quadrature integration scheme to perform the numerical integration of the governing integrodifferential equations [15], [19]. To help this process, the problem domain is discretized into a set of regular integration cells. Then, each integration cell is transformed into an isoparametric square using a parametric transformation (isoparametric mapping). Once the transformation is done, integration points are placed within the isoparametric square according to the Gauss–Legendre scheme [18], [20]. This procedure is illustrated in Figure 5.

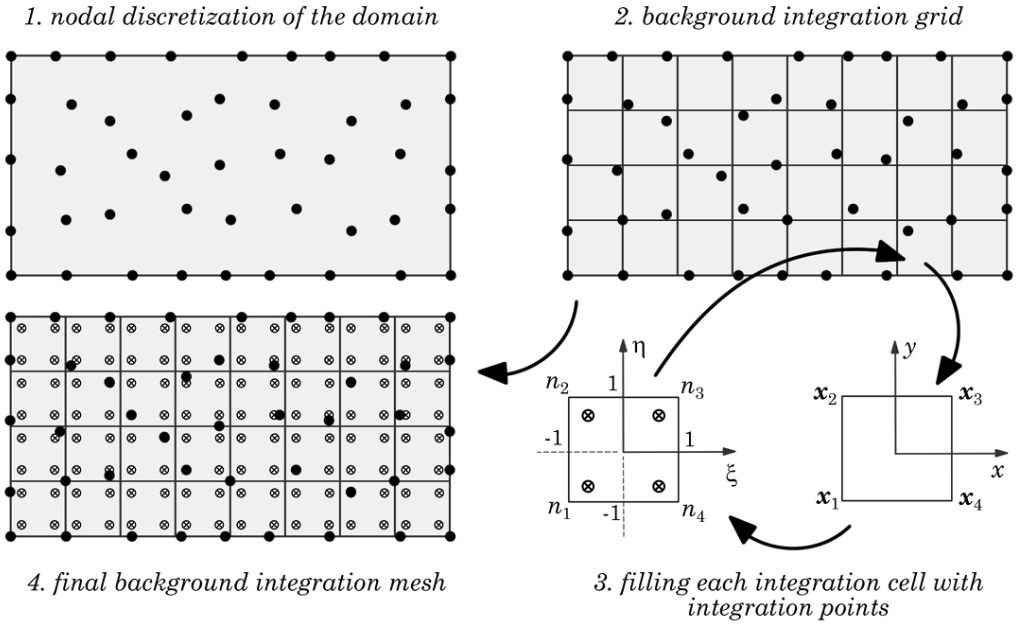

Figure 5 - Integration scheme for the RPIM using a rectangular domain and a regular background [21]

It is possible to retrieve the Cartesian coordinates of the integration points from their isoparametric coordinates with (2.2).

$$\mathbf{x_I} = \begin{Bmatrix} x_I \\ y_I \end{Bmatrix} = \begin{bmatrix} \mathbf{N}(\xi_I, \eta_I)^{\mathrm{T}} \\ \mathbf{N}(\xi_I, \eta_I)^{\mathrm{T}} \end{bmatrix} \cdot \begin{bmatrix} \mathbf{x}_1^{\mathrm{T}} \\ \mathbf{x}_2^{\mathrm{T}} \\ \mathbf{x}_3^{\mathrm{T}} \\ \mathbf{x}_4^{\mathrm{T}} \end{bmatrix} = \begin{bmatrix} N_1 & N_2 & N_3 & N_4 \\ N_1 & N_2 & N_3 & N_4 \end{bmatrix} \cdot \begin{bmatrix} x_1 & y_1 \\ x_2 & y_2 \\ x_3 & y_3 \\ x_4 & y_4 \end{bmatrix} \tag{2.2}$$

Where $\mathbf{N}(\xi, \eta) = \{N_1(\xi, \eta), N_2(\xi, \eta), N_3(\xi, \eta), N_4(\xi, \eta)\}^{\mathrm{T}} = \{N_1, N_2, N_3, N_4\}^{\mathrm{T}}$. The generic equation of $N_i(\xi, \eta)$ is defined as

$$N_i(\xi, \eta) = \frac{1}{4} \cdot (1 + \hat{\xi}_i \cdot \xi) \cdot (1 + \hat{\eta}_i \cdot \eta) \tag{2.3}$$

And assuming the following $\hat{\xi}_i$ and $\hat{\eta}_i$

$$\begin{cases} \Xi = \{\hat{\xi}_1, \hat{\xi}_2, \hat{\xi}_3, \hat{\xi}_4\} = \{-1, -1, 1, 1\} \\ \mathbf{H} = \{\hat{\eta}_1, \hat{\eta}_2, \hat{\eta}_3, \hat{\eta}_4\} = \{-1, 1, 1, -1\} \end{cases} \tag{2.4}$$

The ratio of between the number of integration points and nodes used to discretize the problem domains is a recurring topic in the literature [18], [20], [22]. When the nodes are coincident with the quadrilateral vertices, a 2 × 2 integration point scheme per integration cell is enough [18].

$$\begin{Bmatrix} \xi_1 \\ \eta_1 \\ \omega_1 \end{Bmatrix} = \begin{Bmatrix} \frac{-1}{\sqrt{3}} & \frac{-1}{\sqrt{3}} & \frac{1}{\sqrt{3}} & \frac{1}{\sqrt{3}} \\ \frac{-1}{\sqrt{3}} & \frac{1}{\sqrt{3}} & \frac{1}{\sqrt{3}} & \frac{-1}{\sqrt{3}} \\ 1 & 1 & 1 & 1 \end{Bmatrix} \tag{2.5}$$

Then, the Cartesian integration weight of each integration point can be obtained with

$$\widehat{\omega}_1 = \frac{A_{cel}}{A_{iso}} \cdot \omega_1 \tag{2.6}$$

Where A_{cel} is the total area of the integration cell, and A_{iso} the total area of the isoparametric cell, which is $A_{iso} = 2 \times 2 = 4$.

Thus, a function $f(x, y)$, defined within a quadrilateral domain Ωh, can be integrated using a Gauss–Legendre integration scheme with 2 × 2 = 4 integration points:

$$F = \int_{\Omega_h} f(x, y)\, d\Omega_h = \sum_{\mathrm{I}=1}^{4} f(x_\mathrm{I}, y_\mathrm{I}) \cdot \widehat{\omega}_\mathrm{I} \tag{2.7}$$

Assuming that the Cartesian coordinates $\boldsymbol{x}_\mathrm{I} = \{x_\mathrm{I}, y_\mathrm{I}\}^\mathrm{T}$ and integration weights $\widehat{\omega}_\mathrm{I}$ of the integration points are calculated using Equations (2.2) and (2.6), respectively.

This process is repeated for each integration cell, and the problem's domain is discretised with a cloud of n_Q integration points that forms the background integration mesh. Because the background integration cells are coincident with the problem's domain, the domain area can be calculated with $A_\Omega = \sum_{\mathrm{I}=1}^{n_Q} \widehat{\omega}_\mathrm{I}$.

2.6.2. NNRPIM Integration

After forming the Voronoï diagram, a background set of integration points can be constructed. As shown in Figure 6, Voronoï cells can be subdivided into quadrilaterals. The Gauss-Legendre quadrature integration scheme is then used to define the position and weight of each integration point inside the quadrilateral [19].

The procedure involves several steps, first, each quadrilateral of a given Voronoï cell V_i is mapped into a unit isoparametric square, This transformation allows for the distribution of integration points within the isoparametric square according to the Gauss–Legendre integration scheme [18].

Then, the centre of the geometric shape of each sub-division is determined, after that the middle points on the quadrilateral edges are defined creating another sub-division. The Gauss-

Legendre quadrature is then applied to obtain the integration points in each sub-division filling each one with $k \times k$ integration points.

After obtaining the respective the integration points location and weight, the isoparametric coordinates of the integration points are converted back to Cartesian coordinates.

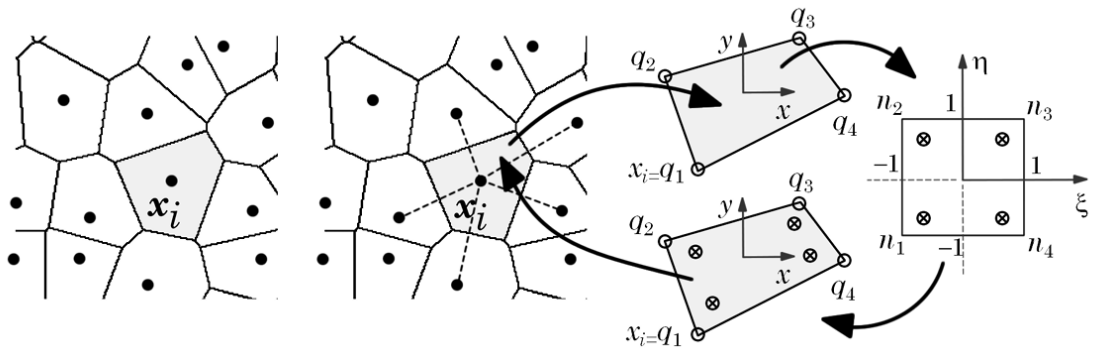

Figure 6 - Generic procedure for the construction of the background set of integration points based on the Voronoï diagram [19]

To perform the numerical integration, considered the function $F(x)$ defined in domain Ω. The global integration can be expressed as a sum,

$$\int_{\Omega} \boldsymbol{F}(\boldsymbol{x})\, d\Omega = \sum_{i=1}^{n_g} \widehat{w}_i \boldsymbol{F}(\boldsymbol{x}_i) \tag{2.8}$$

Where $\widehat{w}_i$ is the weight of the integration point $\boldsymbol{x}_i$.

2.7. Shape Functions

Shape functions approximate or interpolate the field variable values between discrete points scattered across the domain, enabling the representation of field variables across the domain. By defining how each node influences the field variable at any point in the domain, shape functions ensure the continuity and accuracy of the numerical solution. Both RPIM and NNRPIM apply the same shape function techniques, which relies on radial basis functions (RBFs) and polynomial basis functions (PBFs).

The shape functions are constructed using the radial point interpolating technique. To understand its construction, consider a 2D domain, in which a field function $\boldsymbol{u}(\boldsymbol{x})$ is discretised with N nodes: $\boldsymbol{X} = \{x_1, x_2, \dots, x_N\} \in \mathbb{R}^2$. Then, for a given integration point $\boldsymbol{x}_\mathrm{I} \in \mathbb{R}^2 \wedge \boldsymbol{x}_\mathrm{I}$, its interpolated value $\boldsymbol{u}(\boldsymbol{x}_I)$ can be obtained with

$$\boldsymbol{u}(\mathbf{x}_I) = \{\boldsymbol{r}(\boldsymbol{x}_I)^\mathrm{T}, \boldsymbol{p}(\boldsymbol{x}_I)^\mathrm{T}\} \begin{Bmatrix} \mathbf{a} \\ \mathbf{b} \end{Bmatrix} \tag{2.9}$$

Where $\boldsymbol{r}(\boldsymbol{x}_I) = \{r_1(\boldsymbol{x}_I), \dots, r_n(\boldsymbol{x}_I)\}^\mathrm{T}$ is a radial basis function (RBF), $\boldsymbol{p}(\boldsymbol{x}_I)$ is a polynomial basis function $\boldsymbol{p}(\boldsymbol{x}_I) = \{p_1(\boldsymbol{x}_I), \dots, p_m(\boldsymbol{x}_I)\}^\mathrm{T}$ with m monomials, and $a_i(\mathbf{x}_I)$ and $b_j(\mathbf{x}_I)$ are nonconstant coefficients of $\boldsymbol{r}(\mathbf{x}_I)$ and $\boldsymbol{p}(\mathbf{x}_I)$, respectively, which are defined as $\boldsymbol{a}(\boldsymbol{x}_I) = \{a_1(\boldsymbol{x}_I), \dots, a_n(\boldsymbol{x}_I)\}^\mathrm{T}$ and $\boldsymbol{b}(\boldsymbol{x}_I) = \{b_1(\boldsymbol{x}_I), \dots, b_m(\boldsymbol{x}_I)\}^\mathrm{T}$.

The inclusion of the polynomial basis function improves the stability of shape functions. For instance, the inclusion of a polynomial of order k ensures C^k consistency and allows the RPIM to pass the standard patch test. Still, due to the increase of computational cost of adding high-order polynomials, it is more usual to include low order polynomial basis, such as constant polynomial basis $(\boldsymbol{p}(\boldsymbol{x}_I) = \{1, x_I, y_I\}^{\mathrm{T}}, m = 3)$, or quadratic polynomial basis $(\mathbf{p}(\boldsymbol{x}_I) = \{1, x_I, y_I, x_I^2, x_I \cdot y_I, y_I^2\}^{\mathrm{T}}, m = 6)$.

The preliminary works on the RPIM [11], [22] recommend the use of Multiquadratic Radial Basis Function (MQ-RBF), which was initially proposed by Hardy [23]. Later, Belinha [18] proposed a modification to the MQ-RBF to account for the spatial dimension of the problem's domain:

$$r_j(\mathbf{x}_i) = r_{ij} = (d_{ij}^2 + (\widehat{\omega}_I \cdot c)^2)^p = \left(\left(\sqrt{(x_j - x_i)^2 + (y_j - y_i)^2}\right)^2 + (\widehat{\omega}_I \cdot c)^2\right)^p \tag{2.10}$$

MQ-RBF shape parameters are defined by c and p. For 2D analyses, the original RPIM literature recommends $c = 1.42$ and $p = 1.03$. However, posterior works have shown that there are other suitable values for c and p. In the work of Belinha [18], through the optimisation of the Kronecker delta property of the 2D RPI shape functions, it was discovered that c should be close to zero, but not zero, and p should be close to one, but not one [18], where the following MQ-RBF shape parameters were found to be suitable: $c = 10^{-4}$ and $p = 1 - 10^{-4}$. The results documented in the literature [18] show that these alternative values for the shape parameters make it possible to reproduce highly complex variable fields and to achieve accurate and stable results.

In the seminal works on the RPIM [11], [22], it was found that to obtain a unique solution, the following equality has to be imposed in order to allow a unique solution:

$$\sum_{i=1}^{n} p_j(\boldsymbol{x}_i) a_i(\boldsymbol{x}_i) = 0 \tag{2.11}$$

With $j = \{1,2, \dots, m\}$. Consequently, a new equation matrix can be established by combining equation (2.9) with (2.11):

$$\begin{bmatrix} \boldsymbol{R} & \boldsymbol{P} \\ \boldsymbol{P}^T & \mathbf{0} \end{bmatrix} \begin{Bmatrix} \boldsymbol{a} \\ \boldsymbol{b} \end{Bmatrix} = \boldsymbol{G} \begin{Bmatrix} \boldsymbol{a} \\ \boldsymbol{b} \end{Bmatrix} = \begin{Bmatrix} \boldsymbol{u}_s \\ \mathbf{0} \end{Bmatrix} \tag{2.12}$$

where the vector of the nodal parameters $\mathbf{u}_s$ is defined as

$$\boldsymbol{u}_s = \{u_1, u_2, \dots, u_n\}^{\mathrm{T}} \tag{2.13}$$

The RBF Matrix $\boldsymbol{R}$ can be computed with

$$\boldsymbol{R} = \begin{bmatrix} r_{11} & r_{12} & \cdots & r_{1n} \\ r_{21} & r_{22} & \dots & r_{2n} \\ \vdots & \vdots & \ddots & \vdots \\ r_{n1} & r_{n2} & \cdots & r_{nn} \end{bmatrix} \tag{2.14}$$

And the polynomial basis matrix $\boldsymbol{P}$ can be obtained with

$$\boldsymbol{P} = \begin{bmatrix} p_1(\boldsymbol{x}_1) & p_2(\boldsymbol{x}_1) & \cdots & p_m(\boldsymbol{x}_1) \\ p_1(\boldsymbol{x}_2) & p_2(\boldsymbol{x}_2) & \dots & p_m(\boldsymbol{x}_2) \\ \vdots & \vdots & \ddots & \vdots \\ p_1(\boldsymbol{x}_n) & p_2(\boldsymbol{x}_n) & \cdots & p_m(\boldsymbol{x}_n) \end{bmatrix} \tag{2.15}$$

Because $\boldsymbol{R}$ is a symmetric matrix, moment $\boldsymbol{G}$ is symmetric as well. Resolving (2.12) makes it possible to obtain

$$\begin{Bmatrix} \boldsymbol{a} \\ \boldsymbol{b} \end{Bmatrix} = \boldsymbol{G}^{-1} \cdot \begin{Bmatrix} \boldsymbol{u}_s \\ \boldsymbol{0} \end{Bmatrix} \tag{2.16}$$

Finally, replacing the nonconstant values, $\{\boldsymbol{a}, \boldsymbol{b}\}^{\mathrm{T}}$, of Equation (2.16) in Equation (2.9), the interpolation of $\mathbf{x}_I$ is obtained:

$$\boldsymbol{u}(\boldsymbol{x}_I) = \{\boldsymbol{r}(\boldsymbol{x}_I)^T, \boldsymbol{p}(\boldsymbol{x}_I)^T\} \cdot \boldsymbol{G}^{-1} \cdot \begin{Bmatrix} \boldsymbol{u}_s \\ \boldsymbol{0} \end{Bmatrix} = \{\boldsymbol{\Phi}(\boldsymbol{x}_I), \boldsymbol{\Psi}(\boldsymbol{x}_I)\} \cdot \begin{Bmatrix} \boldsymbol{u}_s \\ \boldsymbol{0} \end{Bmatrix} \tag{2.17}$$

Where the interpolation function of $\boldsymbol{x}_I$ is represented by $\boldsymbol{\Phi}(\boldsymbol{x}_I)$:

$$\{\boldsymbol{\Phi}(\boldsymbol{x}_I), \boldsymbol{\Psi}(\boldsymbol{x}_I)\} = \{\boldsymbol{r}(\boldsymbol{x}_I)^T, \boldsymbol{p}(\boldsymbol{x}_I)^T\} \cdot \mathbf{G}^{-1} = \{\phi_1(\boldsymbol{x}_I), \dots, \phi_n(\boldsymbol{x}_I), \psi_1(\boldsymbol{x}_I), \dots, \psi_m(\boldsymbol{x}_I)\} \tag{2.18}$$

The integrodifferential equations ruling elasticity require the calculation of the partial derivates of $\boldsymbol{\Phi}(\boldsymbol{x}_I)$, which can be computed (for general direction ξ) with

$$\boldsymbol{\Phi}_{\xi}(\boldsymbol{x}_I) = \left\{\boldsymbol{r}(\boldsymbol{x}_I)_{\xi}^{\mathrm{T}}, \boldsymbol{p}(\boldsymbol{x}_I)_{\xi}^{\mathrm{T}}\right\} \cdot \mathbf{G}^{-1} \tag{2.19}$$

Where the corresponding MQ-RBF partial derivatives are obtained with

$$(r_{ij})_{\xi} = 2 \cdot p \cdot \left(d_{ij}^2 + c^2\right)^{p-1} \cdot \left(\xi_j - \xi_i\right) \tag{2.20}$$

Radial point interpolating functions satisfy the partition of unity and possess the Kronecker delta property, allowing to directly impose boundary conditions [18].

2.8. Elasticity Theory

The principle of virtual work is employed to derive the global system of equations. Consider a solid domain Ω, bounded by a surface, which includes natural and essential boundaries denoted by Γ_t and Γ_u, respectively. The solid domain movement is constrained along Γ_u, while it is subjected to body forces $\boldsymbol{b}$ and external forces $\bar{\boldsymbol{t}}$ acting on Γ_t. By applying the principle of virtual work, which equates the work done by external forces to the work done by internal forces $W_{int} = W_{ext}$ the following relationship can be established:

$$\int_{\Omega} \delta\boldsymbol{\varepsilon}^T \cdot \boldsymbol{\sigma} \cdot d\Omega = \int_{\Omega} \delta\boldsymbol{u}(\boldsymbol{x}_I)^T \cdot \boldsymbol{b} \cdot d\Omega + \int_{\Gamma_t} \delta\boldsymbol{u}(\boldsymbol{x}_I)^T \cdot \bar{\boldsymbol{t}} \cdot \mathbf{d}\Gamma \tag{2.21}$$

It is possible to interpolate both displacement components $\{u, v\}$ simultaneously:

$$\boldsymbol{u}(\boldsymbol{x}_l) = \begin{Bmatrix} u(\boldsymbol{x}_I) \\ v(\boldsymbol{x}_I) \end{Bmatrix} = \boldsymbol{H}(\boldsymbol{x}_l) \cdot \boldsymbol{u} = \begin{bmatrix} \phi_1(\boldsymbol{x}_I) & 0 & \cdots & \phi_n(\boldsymbol{x}_I) & 0 \\ 0 & \phi_1(\boldsymbol{x}_I) & \cdots & 0 & \phi_1(\boldsymbol{x}_I) \end{bmatrix} \cdot \begin{Bmatrix} u_1 \\ v_1 \\ \vdots \\ u_n \\ v_n \end{Bmatrix} \tag{2.22}$$

Consequently, the deformation vector can be represented as:

$$\boldsymbol{\varepsilon}(\boldsymbol{x}_l) = \boldsymbol{L} \cdot \boldsymbol{u}(\boldsymbol{x}_l) = \begin{bmatrix} \dfrac{\partial}{\partial x} & 0 \\ 0 & \dfrac{\partial}{\partial y} \\ \dfrac{\partial}{\partial y} & \dfrac{\partial}{\partial x} \end{bmatrix} \cdot \boldsymbol{\Phi}(\boldsymbol{x}_l) \cdot \boldsymbol{u} = \boldsymbol{B}(\boldsymbol{x}_I) \cdot \boldsymbol{u} = \boldsymbol{B}(\boldsymbol{x}_I) \cdot \begin{Bmatrix} u_1 \\ v_1 \\ \vdots \\ u_n \\ v_n \end{Bmatrix} \tag{2.23}$$

Making it possible to obtain the deformation matrix $\mathbf{B}(\boldsymbol{x}_I)$:

$$\boldsymbol{B}(\boldsymbol{x}_l) = \begin{bmatrix} \dfrac{\partial \Phi_1(\boldsymbol{x}_I)}{\partial x} & 0 & \cdots & \dfrac{\partial \Phi_n(\boldsymbol{x}_I)}{\partial x} & 0 \\ 0 & \dfrac{\partial \Phi_1(\boldsymbol{x}_I)}{\partial y} & \cdots & 0 & \dfrac{\partial \Phi_n(\boldsymbol{x}_I)}{\partial y} \\ \dfrac{\partial \Phi_1(\boldsymbol{x}_I)}{\partial y} & \dfrac{\partial \Phi_1(\boldsymbol{x}_I)}{\partial x} & \cdots & \dfrac{\partial \Phi_n(\boldsymbol{x}_I)}{\partial y} & \dfrac{\partial \Phi_n(\boldsymbol{x}_I)}{\partial x} \end{bmatrix} \tag{2.24}$$

The stress can be calculated at the integration point $\boldsymbol{x}_I$ assuming Hooke's law:

$$\boldsymbol{\sigma}(\boldsymbol{x}_I) = \boldsymbol{c}(\boldsymbol{x}_I) \cdot \boldsymbol{\varepsilon}(\boldsymbol{x}_I) = \boldsymbol{c}(\boldsymbol{x}_I) \cdot \boldsymbol{B}(\boldsymbol{x}_I) \cdot \boldsymbol{u} \tag{2.25}$$

Where $\boldsymbol{c}(\boldsymbol{x}_I)$ is the material constitutive matrix of integration point $\boldsymbol{x}_I$, which for a 2D problem can be defined for plane stress or plane stress assumptions [24]. Thus, considering plane stress, it can be defined as:

$$\boldsymbol{c} = \frac{E_2}{1 - \alpha_1 \cdot v_{21}^2} \begin{bmatrix} \alpha_1 & \alpha_1 \cdot v_{21}^2 & 0 \\ \alpha_1 \cdot v_{21}^2 & 0 & 0 \\ 0 & 0 & \alpha_2 \cdot (1 - \alpha_1 \cdot v_{21}^2) \end{bmatrix} \tag{2.26}$$

And assuming plane strain, the constitutive matrix can be written as:

$$\boldsymbol{c} = \frac{E_2}{\alpha_3 \cdot \alpha_4} \begin{bmatrix} \alpha_3 \cdot (1 - \alpha_1 \cdot v_{21}^2) & \alpha_1 \cdot v_{21} \cdot \alpha_3 & 0 \\ \alpha_1 \cdot v_{21} \cdot \alpha_3 & 1 - v_{12}^2 & 0 \\ 0 & 0 & \alpha_2 \cdot (1 - \alpha_1 \cdot v_{21}^2) \end{bmatrix} \tag{2.27}$$

Where $\alpha_1 = E_1/E_2$, $\alpha_2 = G_{12}/E_2$, $\alpha_3 = 1 + v_{12}$, and $\alpha_4 = 1 - v_{12} - 2 \cdot \alpha_1 v_{21}^2$. The directional mechanical properties E_i, G_{ij}, and v_{ij} are defined as follows: E_i is the Young modulus in material direction i, and G_{ij}, and v_{ij} are the elastic shear modulus and Poisson's ratio in the material distortion plane O_{ij}, respectively.

Thus, with the substitution of stress and strain vectors in (2.21) the following expression is obtained:

$$\int_{\Omega} \delta(\boldsymbol{B}(\boldsymbol{x}_l) \cdot \mathbf{u})^T \cdot (\mathbf{c}(\boldsymbol{x}_l) \cdot \boldsymbol{B}(\boldsymbol{x}_l) \cdot \mathbf{u}) \cdot d\Omega = \int_{\Omega} \delta(\boldsymbol{H}(\boldsymbol{x}_l) \cdot \mathbf{u})^T \cdot \boldsymbol{b} \cdot d\Omega + \int_{\Gamma_t} \delta(\boldsymbol{H}(\boldsymbol{x}_l) \cdot \mathbf{u})^T \cdot \bar{\boldsymbol{t}} \cdot \boldsymbol{d\Gamma} \tag{2.28}$$

Considering small strains ($\delta\mathbf{B}(\boldsymbol{x}_1) = 0$ and $\delta\mathbf{H}(\boldsymbol{x}_1) = 0$), the expression can be simplified:

$$\int_{\Omega} \mathbf{u}^T \boldsymbol{B}(\boldsymbol{x}_l)^T \cdot \mathbf{c}(\boldsymbol{x}_l) \cdot \boldsymbol{B}(\boldsymbol{x}_l) \cdot \mathbf{u} \cdot d\Omega + \int_{\Omega} \delta\mathbf{u}^T \boldsymbol{H}(\boldsymbol{x}_l)^T \cdot \boldsymbol{b} \cdot d\Omega + \int_{\Gamma_t} \delta\mathbf{u}^T \cdot \boldsymbol{H}(\boldsymbol{x}_l) \cdot \bar{\boldsymbol{t}} \cdot \mathrm{d}\Gamma \tag{2.29}$$

$$\delta\mathbf{u}^T \int_{\Omega} \boldsymbol{B}(\boldsymbol{x}_l)^T \cdot \mathbf{c}(\boldsymbol{x}_l) \cdot \boldsymbol{B}(\boldsymbol{x}_l) \cdot d\Omega \cdot \mathbf{u} = \delta\mathbf{u}^T \int_{\Omega} \boldsymbol{H}(\boldsymbol{x}_l)^T \cdot \boldsymbol{b} \cdot d\Omega + \delta\mathbf{u}^T \int_{\Gamma_t} \boldsymbol{H}(\boldsymbol{x}_l)^T \cdot \bar{\boldsymbol{t}} \cdot \mathrm{d}\Gamma \tag{2.30}$$

Leading to the final system of equations:

$$\boldsymbol{K} \cdot \boldsymbol{u} = \boldsymbol{f}_b + \boldsymbol{f}_t \tag{2.31}$$

Which makes it possible to calculate the unknown global displacement field:

$$\boldsymbol{u} = \boldsymbol{K}^{-1}\boldsymbol{f}_b + \boldsymbol{f}_t \tag{2.32}$$

Where $\boldsymbol{K}$ is the global stiffness matrix

$$\boldsymbol{K} = \int_{\Omega} \boldsymbol{B}(\boldsymbol{x}_l)^T \cdot \mathbf{c}(\boldsymbol{x}_l) \cdot \boldsymbol{B}(\boldsymbol{x}_l) \cdot d\Omega \cdot \mathbf{u} = \sum_{l=1}^{N_Q} \boldsymbol{B}(\boldsymbol{x}_l)^T \cdot \mathbf{c}(\boldsymbol{x}_l) \cdot \boldsymbol{B}(\boldsymbol{x}_l) \cdot \widehat{\omega}_l \cdot h(\boldsymbol{x}_l) \tag{2.33}$$

The external force vector $\boldsymbol{f}_t$ and global body vector $\boldsymbol{f}_b$ can be defined as:

$$\boldsymbol{f}_t = \int_{\boldsymbol{\Gamma_t}} \boldsymbol{H}(\boldsymbol{x}_l)^T \cdot \bar{\boldsymbol{t}} \cdot d\Gamma = 0 = \sum_{l=1}^{N_Q} \boldsymbol{H}(\boldsymbol{x}_j)^T \cdot \bar{\boldsymbol{t}} \cdot \widehat{\omega}_j \tag{2.34}$$

$$\boldsymbol{f}_b = \int_{\boldsymbol{\Omega}} \boldsymbol{H}(\boldsymbol{x}_l)^T \cdot \boldsymbol{b} \cdot d\Omega = \sum_{l=1}^{N_Q} \boldsymbol{H}(\boldsymbol{x}_l)^T \cdot \mathbf{b} \cdot \widehat{\omega}_j \cdot h(\boldsymbol{x}_l) \tag{2.35}$$

3. Structural Optimization

This chapter provides a review of the state of structural optimization. It highlights the most used optimization algorithms and goes into the historical development of optimization methods. Subsequently, an overview of the application of meshless methods in optimization is presented. Lastly, recent practical applications of structural optimization are examined, demonstrating its effectiveness as an engineering tool.

3.1. State of the Art

In recent years, structural optimization has become a topic of significant interest and as undergone through a remarkable development within the academic community [25], [26], [27], as well as in industry [28]. This growing interest is reflected in the substantial increase in the number of publications over the year as shown in Figure 7. The upward trend in published articles highlights the continuous advancements in optimization techniques, the development of more efficient computational tools, and the expanding range of practical applications. This surge in attention also underscores the recognition of structural optimization as a crucial tool for improving performance, reducing material usage, and enabling innovative designs across various engineering disciplines.

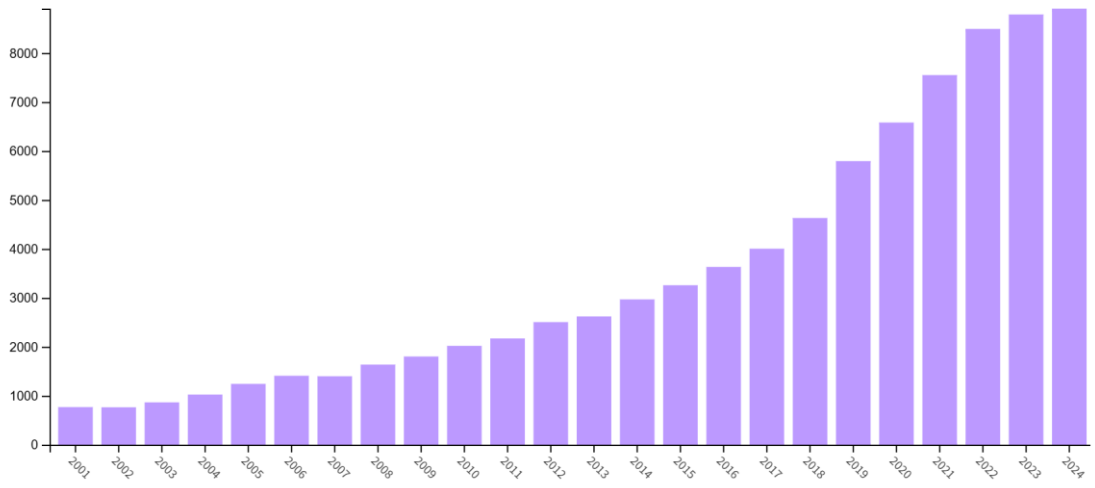

Figure 7 - Number of publications per year on structural optimization [1]

Structural optimization seeks to determine the ideal distribution of material within a specified design domain to either maximize or minimize specific objectives while satisfying one or more design constraints. A common design scenario involves minimizing structural compliance, or equivalently maximizing stiffness, subject to a constraint on material volume usage. A typical structural optimization problem is illustrated in Figure 8.

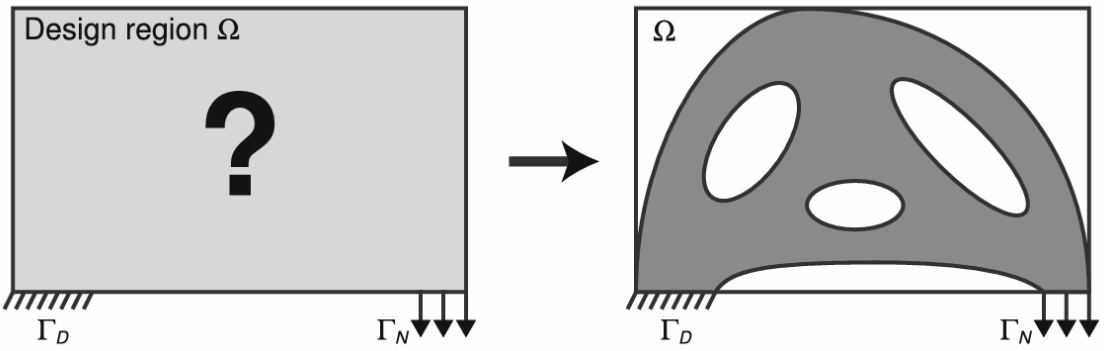

Figure 8 - Illustration of typical structural topology optimization [29]

The development of structural optimization methods has been a dynamic field, evolving significantly over the past decades [30]. The initial concept of layout optimization was introduced by A. G. M. Michell in 1904 [31], due to limitations this work was purely academic and did not have any application. Michell's work was left untouched until the 1950s where it was picked up by a number of different researchers, such as Hill [32], Heyman [33], Heyman and Prager [34], Foulkes [35], Drucker and Shield [36], Livesley [37], Prager [34], [38], Prager and Shield [39], Onat et al. [40] and Hemp [41]. They introduced methods including linear programming techniques and developed approaches to calculate optimal configurations based on plastic collapse mechanisms. These efforts helped identify conditions for optimal designs, though they were still limited by mathematical complexity and practical constraints. In the 1960s, techniques like linear programming and plastic design principles were added to the field of shape optimization to solve problems for beams, plates, and trusses. These studies refined the understanding of how materials should be distributed in structures to achieve maximum efficiency under various loading conditions. Techniques to determine strain fields with graphical construction were developed by Chan [42]. Cox [43] revealed some interesting examples of single-stress structures and applications of Maxwell's theorem. Marcal and Prager [44] give the optimization of a beam using a volume cost function that was later generalized to arbitrary one and two-dimensional plastic structures by Prager and Shield [45]. A program to solve framework optimization problems using the "simplex method", a linear programming technique, was developed by Dantzig [46]. Despite these advancements, the applications remained confined to simplified models and lacked the computational power necessary for real-world implementation. The 1960s and 1970s decades saw significant advancements, driven by the development of computational tools. During this period, Rozvany and Prager extended Michell's optimization principles to beams, grillages, and multi-component systems under various load conditions. The 1980s marked an era for structural optimization with the introduction of methods that could handle more complex geometries and real-world applications, among these were the homogenization method by Bendsøe and Kikuchi [47], the

Solid Isotropic Material with Penalization (SIMP) method [48], [49], [50], one of the most widely used techniques in structural optimization.

This area of research has been very active since, with several methods being developed, in literature several non-gradient based algorithms have been applied to structural optimization. Such methods include Genetic Algorithms (GAs) [51], [52], [53], [54], Artificial Immune Algorithms [55] and many others. However, these said methods did not gain significant acceptance due to the difficulty to ensure structural connectivity. One technique gained widespread popularity despite the shortcomings, the Evolutionary Structural Optimization (ESO) method, with wide range of applications in different areas [30].

There are three different types of structural optimization problems, sizing, shape and topology optimization [56]. Sizing optimization focuses on modifying the dimensions of structural elements, such as cross-sectional areas or thicknesses, while keeping the overall geometry and connectivity unchanged. Shape optimization changes the geometry without altering the underlying topology. At last, topological optimization takes a broader approach and has maximum flexibility to change the design and determine the optimum material configuration. A key advantage of topology optimization compared to shape or sizing optimizations lies in its ability to determine the structural topology or material layout within the design domain without any prior assumptions.

3.2. Evolutionary Structural Optimization Method (ESO)

The ESO (Evolutionary Structural Optimization) method [57] is a topology optimization technique used to design efficient structures by iteratively removing material from a given design domain where they are deemed inefficient or unnecessary based on certain optimization criteria, such as low stress, strain energy, or sensitivity. This approach seeks to find the optimal material distribution for a structure that meets specific performance criteria, such as minimizing weight while ensuring adequate strength and stiffness. The ESO method has been adapted to address different design objectives using heuristic or empirical criteria, which may not be either based on sensitivity analysis [58].

The ESO method has found applications in a different number of topology optimization problems such as buckling load [59], frequency [60], temperature [61] or a combination of the above [62], and has proven itself to be an useful tool for engineers to discover different structurally efficient geometries during the conceptual stage of the project [60].

In the original ESO proposition [57], the stress level of each element is determined by comparing the element von Mises stress σ_e^{vm} with a stipulated critical or maximum von Mises stress of the whole structure σ_{max}^{vm}.

The von Mises stress σ_e^{vm} for a general state of stress is given by:

$$\sigma_e^{vm} = \sqrt{\frac{1}{2}[(\sigma_{11} - \sigma_{22})^2 + (\sigma_{22} - \sigma_{33})^2 + (\sigma_{33} - \sigma_{11})^2] + 3(\sigma_{12}^2 + \sigma_{23}^2 + \sigma_{31}^2)} \quad (3.36)$$

Elements with von Mises stress lower the threshold are deleted or removed from the model based on a previously defined rejection ratio (c_{rr}).

$$\sigma_e^{vm} < c_{rr} \cdot \sigma_{max}^{vm} \tag{3.37}$$

The cycle of finite element analysis and element removal is reiterated using the same rejection ratio until a steady state is reached, in this state there are no more elements satisfying this deletion threshold. The rejection ratio can then be increased according to a defined evolutionary rate c_{er}.

$$c_{rr}^{new} = c_{rr}^{old} + c_{er} \tag{3.38}$$

The iteration process is then repeated until a new steady state is reached, ending when reaching a desired optimum state.

ESO is classified as a heuristic method, it uses trial and error approach rather than relying on mathematical techniques, and its key limitations reflect the characteristics of heuristic methods. One of the main limitations of this method is that it does not guarantee convergence to a globally optimal solution, meaning that they can often result in a suboptimal solution. Another limitation of this method is the irreversibility of material removal, meaning that the material removed cannot be restored in the next iterations, due to this limitation if a material is removed prematurely, it can have a negative impact on the way the iteration evolves limiting the final design. This issue becomes more manifest in highly complex geometries where the optimal design is not clear and where it may be challenging to predict in advance which material elements will be important for structural integrity and which ones can be removed without consequences. As ESO only removes elements and those removed ones cannot be brought back in the later iterations, an oversized initial design area is required to ensure that the final design is represented by adequate elements. In some structures the optimization is misled because of an inappropriately defined initial area [63]. Hence, while the ESO method often produces a significantly improved solution compared to the initial design there is no guarantee that the design is optimal. Research by Li et al. [64] and McKeown [65] has demonstrated that a fully stressed design obtained with the ESO method is equivalent with the stiffness criterion.

3.3. Bidirectional ESO Method (BESO)

The Bi-Directional Evolutionary Structural Optimization (BESO) method [66] is an extension of the Evolutionary Structural Optimization (ESO) combined with an additive evolutionary structural optimisation (AESO) algorithm. Unlike the ESO approach, which only removes material from an oversized initial design, BESO allows both the removal and addition of material to alleviate high stress areas, this bi-directional ability resolves some of the limitations of ESO method. One key advantage of BESO is the flexibility in choosing the initial design, any configuration that meets the loading and boundary conditions can be used as the starting point. Quite often, it is convenient to use the simpler designs connecting the loads and supports, making the initial model more straightforward and more efficient [67].

In BESO algorithm, the elements with the lowest von Mises stresses are removed satisfying the first criterion in (3.39) and void elements near the highest von Mises stress regions are switched

on as solid elements satisfying the second equation in (3.39), where $\tilde{\sigma}_e^{vm}$ is the von Mises stress approximation for void elements.

$$\begin{cases} \sigma_e^{vm} < c_{rr} \cdot \sigma_{max}^{vm} \longrightarrow element\ removal \\ \tilde{\sigma}_e^{vm} > c_{ir} \cdot \sigma_{max}^{vm} \longrightarrow element\ addition \end{cases} \tag{3.39}$$

The early development of the ESO and BESO methods lacked theorical rigor and neglected important topology optimization problems, such as existence of solution, mesh-dependency, checker-board and local optimum, etc [68]. Over the years efforts have been made to overcome some of these shortcomings, Li et al. [69] solved the checkerboard problem by averaging the sensitivity number of an element with the neighbouring elements; a perimeter constraint to the BESO method was introduced by Yang et al. [70], Kim et al. [71], [72] introduced cavity control techniques into the BESO method, and fixed grids have been introduced to the BESO method with the aim of reducing computational cost [73], [74].

3.4. Solid Isotropic Material with Penalization (SIMP)

The Solid Isotropic Material with Penalization (SIMP) method is one of the most broadly utilized approaches in topology optimization. It was introduced in the late 1980s and early 1990s and has become a keystone in the field of shape optimization due to its simplicity, effectiveness, and compatibility with computational methods like FEM.

In this method discrete variables are replaced by continuous variables such as material densities, that iteratively guide the solution to a discrete solid/void solution. This process relies on an interpolation function, that explicitly interprets the continuous design variables as the material density of each element. Penalty methods are then utilized to force solutions to suitable “0/1”, “black/white”, or “solid/void” topologies.

A shape optimization study [75] was applied to a robot arm using the SIMP method with FEM achieving significant improvements in performance and efficiency. The arm’s weight was reduced by 55.6% while still maintaining structural rigidity. Additionally, the first natural frequency was increased from 105.93Hz to 123.34Hz enhancing the dynamic stability of the robot. These results demonstrate the effectiveness of the application of the SIMP method on an industrial case.

3.5. Shape Optimization and FEM

Being the most established numerical technique, the FEM has been extensively applied for shape optimization since early 1970s [76], [77]. However, several issues arise from the use of FEM, issues inherently related to mesh-based methods like mesh distortion that result from large shape variations and inconsistent geometry description for design. These issues motivated the development of more robust numerical techniques.

The first shape optimization methods based on FEM used coordinates of boundary nodes of FE mesh as design variables [78]. This method possesses several problems, such as increased number of design variables translates to more computational power requirements and

unfeasible and irregular geometric shapes that do not have any value. During the 1980s and 90s, several techniques were developed to lighten these issues, like the popular design element concept [79], [80], [81], [82], polynomial equations [83], [84], [85], spline representation i.e. Bezier, B-spline, Cubic spline [80], [86], [87] and natural design variables – fictitious loads [88], [89]. Filter methods and regularization techniques are used for gradient-based optimization schemes to solve the problem of impractical geometric shapes generated by this method and ensuring smooth gradient fields and smooth geometry updates, these techniques can be categorized into geometrical and mechanical approaches. Some of these methods are: In-plane and out-of plane regularization [90], [91], [92], vertex morphing [93] and Traction method (H^1 *gradient method*) [92], [93], [94].

3.6. Shape Optimization and Meshless Methods

There is literature that provides evidence of successful applications of meshless methods in shape optimization problems. These methods possess numerous features that make them appropriate numerical analysis techniques for shape optimization problems [95]:

Meshless Methods deal with field variable approximation and numerical integration independently. Unlike FEM, where shape functions are constructed at element level natural coordinates and later transformed to the global Cartesian coordinates, meshless shape functions are constructed using only nodal points and its associated support domains at the global Cartesian coordinates directly without defining elements/ mesh. By this means Meshless Methods are free from mesh distortion and remeshing issue. The background cell structure/mesh is only used for numerical integration purpose, and it does not influence the solution accuracy when it gets distorted. The only condition is that the cells remain convex with positive Jacobian [96]. The meshless shape functions produce higher order field variable continuity (both primary and secondary) improving design sensitivity analysis in gradient-based shape optimization technique and overall solution accuracy [97]. Uneven node placement, which is a frequent occurrence in shape optimization problems, has little effect on meshless solutions [6]. There is literature that supports the successful application of EFGM and RKPM methods in various shape optimization problems such as linear elastic, thermoelastic, structure dynamics and frictional contact problems [95].

3.6.1. Structural Optimization using RPIM

A research work documented in the literature combined the RPIM with the SIMP to carry out a topology optimization design for a continuum structure [98].

The case study used to validate the proposed method was a cantilever beam fixed on the left side with a concentrated load F applied at the middle of the right side as show in Figure 9. The results of the optimization are shown in Figure 10. For comparison, the results obtained with RPIM and SIMP method are shown in Figure 10 (a), the results obtained by FEM are shown in Figure 10 (b) and the results obtained by FEM with sensitivity filtering are shown in Figure 10 (c). The results obtained demonstrates that the method successfully eliminates checkerboard patterns.

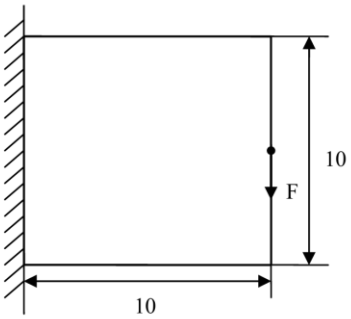

Figure 9 - Cantilever beam problem [98]

(a) (b) (c)

Figure 10 - Optimization results of cantilever beam. (a) optimization result by RPIM, (b) optimization result by FEM, (c) optimization result by FEM with sensitivity filtering [98]

In another study, RPIM was combined with a hard-kill evolutionary algorithm [99]. The object on study was a cantilever beam subjected to a point load as illustrated in Figure 11.

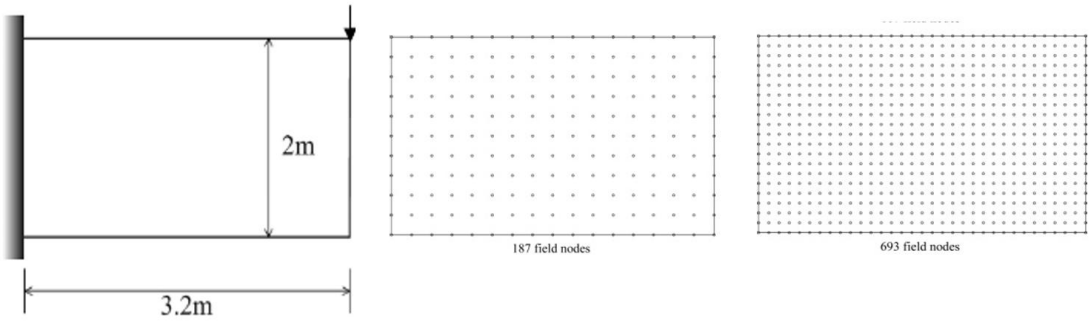

Figure 11 - Cantilever beam [99]

Two different numbers of field nodes with the same number of background cells were used to investigate the effect of the number of field nodes on topology optimization. The results of the test are exhibited in Figure 12 for different iterations, on the left, the results with 187 field nodes are presented, and on the right with 693 field nodes.

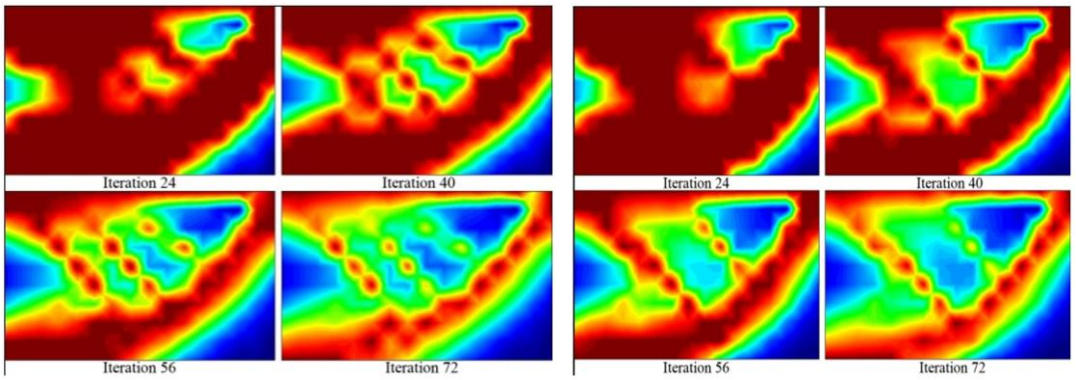

Figure 12- Cantilever beam, effect of the number of field nodes: (left) 187 field nodes, (right) 693 field nodes [99]

After comparing and analysing the results, it can be concluded that the use of a larger number of field numbers with the same number of background cells produces a clearer solution with less noise.

Another case study was conducted, this time with the same number of field nodes but with different number of background cells. The results are illustrated in Figure 13. From the results it is found that the use of more background cells while maintaining the same number of field nodes can lead to more noise.

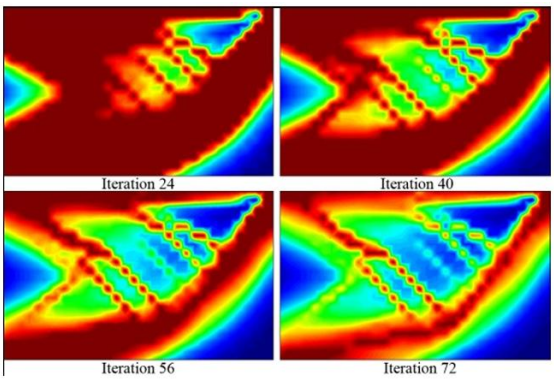

Figure 13 - Cantilever beam topological optimization with more background cells results [99]

A simple supported beam was used to conduct a study on the effects of removing rate. In this study it was investigated a range of removing rates from N=0.01 to N=0.04. The results are shown in Figure 14. From the final topology it is shown that the use of a smaller removing rate triggered more noise.

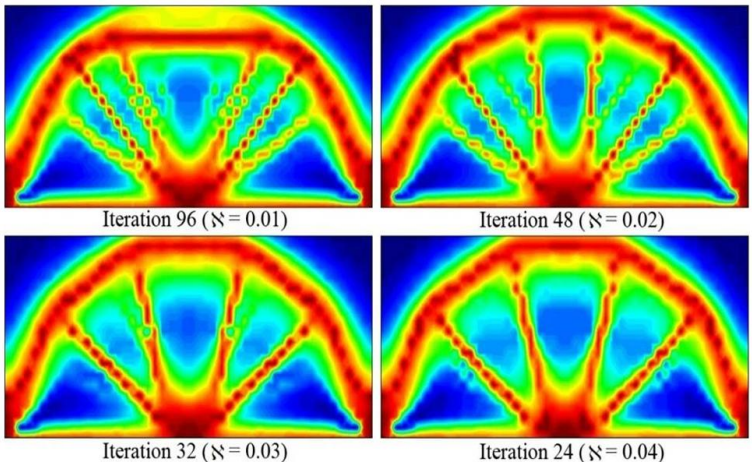

Figure 14 - Effects of removing rate on topological optimization [99]

3.6.2. Structural Optimization using NNRPIM

Despite the significant advantages of the NNRPIM and advancements in computational mechanics, the application of meshless methods on topology optimization remains relatively underexplored. To showcase the capabilities of NNRPIM in topology optimization several benchmark examples were solved, along with a practical application on an automotive component [100]. In the first benchmark a study on a cantilever beam subjected to a point load was conducted. Since the optimal result for this case study is well known in literature, this application allows to assess the validity of the proposed algorithm. Different parameters were used with to evaluate their impact on the result, several analysis combining various nodal discretization were used, and regarding the topology optimization algorithm, the von Mises (VM) and Strain Energy Density (SED) criterions and Decrease Ratio (DR) of 2%, 3%, 4% were considered. The resulting topology for each analysis is presented in Figure 15, where it is shown the results for discretization with 693 nodes and 4131 nodes.

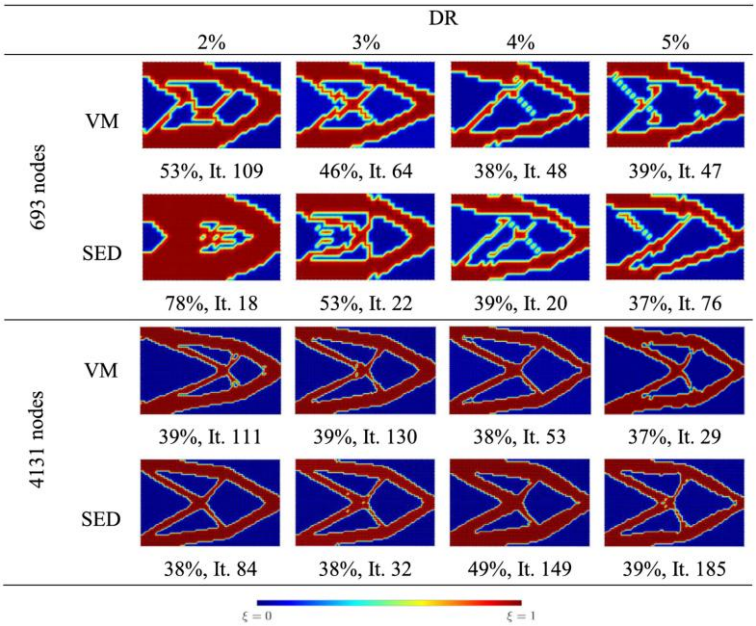

Figure 15 - Topology optimization analyses results [100]

The results show that finer nodal discretization results in more stable and well-defined topologies, closely resembling those reported in the literature. The same topology optimizations were made using second-order influence cells. The results, shown in Figure 16, indicate that first-order natural neighbours (NN) produce smoother contours when compared to second-order natural neighbours, suggesting their preference in the NNRPIM formulation in topology optimization.

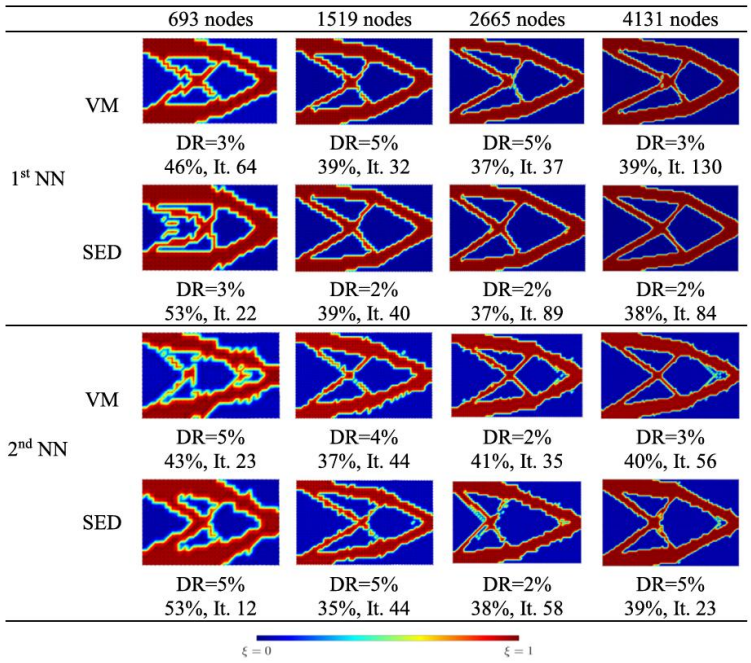

Figure 16 - First-order influence cell vs Second-order influence cell [100]

The same problem was solved using irregular nodal discretization obtaining similar results but with some perturbations due to the irregular nature of the field nodes distribution.

Another benchmark test used in was the “L” shaped bracket problem. Similarly with the first test, different parameters were used. As the first test it was concluded that a denser discretization achieves more accurate and optimal results. The test was also set up with irregular nodal distributions to demonstrate the proficiency of the algorithm with success, the results can be seen in Figure 17.

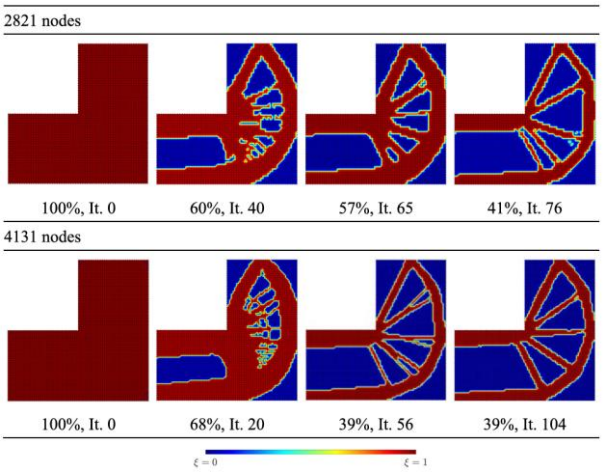

Figure 17 - Topology optimization results for a "L" bracket [100]

Another case study involved a brake pedal, a relatively more complex shape when compared with the previously analysed cases, the geometry of the problem is illustrated in Figure 18. The method once again proved its effectiveness in topology optimization, achieving a 36% volume reduction, resulting in an increase of stiffness to weight ratio of 25.2%, the results of the topological optimization can be seen in Figure 19.

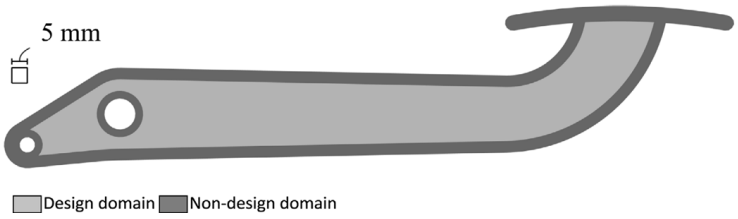

Figure 18 - Brake pedal design and non-design domains considered in the topology optimization problem [100]

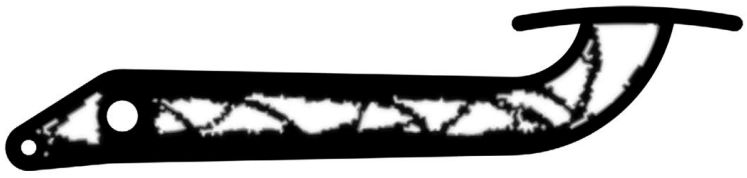

Figure 19 - Algorithm solution [100]

4. Numerical Applications

This chapter presents the practical work carried out in the scope of this dissertation. The main objective of the thesis is to evaluate the performance of different numerical methods FEM, RPIM, and NNRPIM when applied to structural optimization problems. First a convergence study was performed to validate the accuracy of the numerical methods. Next, a set of benchmark problems from literature were studied, allowing a comparison between the obtained topologies with well-established reference solutions. In the end, the methodology is extended to an industrial application. All simulations were performed using the software provided FEMAS (Finite Element and Meshless Analysis Software: cmech.webs.com). The meshes used in the analyses were generated in FEMAP student edition v2412 (Finite Element Modelling And Postprocessing) and subsequently imported into FEMAS to conduct numerical simulations.

4.1. Introductory Convergence Study

An introductory convergence study is carried out using a benchmark example of a cantilever beam in order to validate the accuracy and efficiency of the proposed numerical methods. The study aims to assess the performance and reliability of the RPIM and NNRPIM methods by comparing their results with those obtained using the well-established and widely validated Finite Element Method (FEM) and the analytical solution. For each method, the domain is discretized with different levels of refinement, allowing the convergence behaviour to be evaluated. Convergence is evaluated by analysing the displacement and stress distribution under mesh refinement or nodal density increment.

The benchmark example consists of a two-dimensional cantilever beam subjected to a distributed load at its free end (Figure 20). The dimensions of the beam are $L = 2\ m$ for the length and $D = 1\ m$ for the height. The material properties are: $E = 1000GPa$ and $\nu = 0.3$. A distributed load of $P = 1\ N/m$ is applied along the free end of the cantilever. The analytical solutions for the displacement and stress fields can be found in the literature [18].

Convergence is measured by calculating the relative error of the displacement and stress against the analytical solution. The relative error is calculated using the following expression:

$$Error\ (\%) = \frac{v_{numerical} - v_{analytical}}{v_{analytical}} \tag{4.40}$$

Vertical displacement can be calculated with the following expression:

$$v(x) = \frac{2 \cdot P}{E \cdot D^3}\left[x^2 \cdot (3L - x) + 3\nu \cdot (L - x) \cdot y^2 + x \cdot (4 + 5\nu) \cdot \frac{D^2}{4}\right] \tag{4.41}$$

Normal stress can be calculated with:

$$\sigma_{xx}(x) = -\frac{P \cdot (L - x) \cdot y}{I} \tag{4.42}$$

And shear stress with:

$$\tau_{xy}(y) = -\frac{P \cdot D^2}{8 \cdot I} \cdot \left(1 - \frac{4y^2}{D^2}\right) \tag{4.43}$$

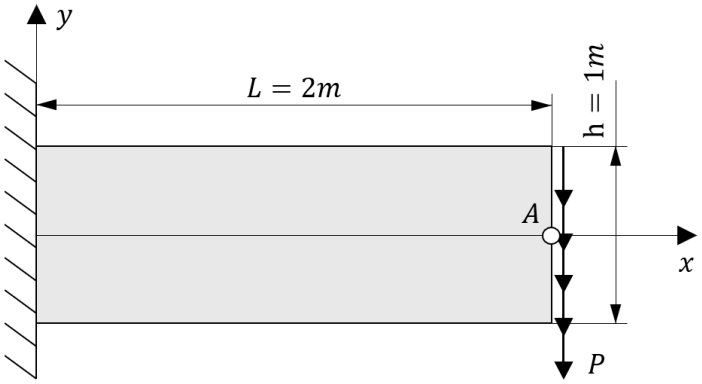

Figure 20 - Cantilever beam problem

The cantilever analysis was solved using a 2D simplification. The problem is formulated within the framework of linear elasticity, assuming small deformations and plane stress conditions.

For the FEM analysis four node quadrilateral elements were used. For the RPIM influence domains with 16 nodes where used, the following parameters were used: RPI-MQRBF c = 1.42; RPI-MQRBF p = 1.03. Regarding the NNRPIM second degree influence domains were used with full integration. The following parameters for the RPI-MQRBF were used: c = 0.0001; p = 0.9999

The analysis was conducted using regular meshes composed of 8385, 2145, 561, 153, 45, and 15 nodes. Vertical displacement values were taken at point A. Additionally, the normal stress long $y = D/2$, and the shear stress at $x = L/2$ were recorded and analyzed.

The convergence results for the vertical displacement at point A and the corresponding error with respect to the analytical solution are presented in Figure 21. Figure 21 (a) illustrates the displacement values obtained using FEM, RPIM, and NNRPIM for increasing nodal resolutions, while Figure 21 (b) displays the relative error for each method.

The data shows that all methods converge towards the analytical solution. However, RPIM and NNRPIM exhibit a slightly higher convergence rate than FEM. For lower node counts, the FEM results are relatively less accurate, showing greater deviation from the analytical displacement. In contrast, RPIM and NNRPIM results quickly stabilize near the analytical solution, even with a

coarser discretization. Despite the superior convergence rates, RPIM and NNRPIM present significantly larger errors than FEM at the lowest nodal resolution.

The error plot further confirms this observation. RPIM and NNRPIM exhibit very similar convergence behaviour, with nearly overlapping error curves. This indicates that both methods achieve comparable accuracy at each level of refinement. FEM starts with a higher initial error and shows a slower reduction rate, requiring a substantially larger number of nodes to reach the same level of accuracy as the meshless methods.

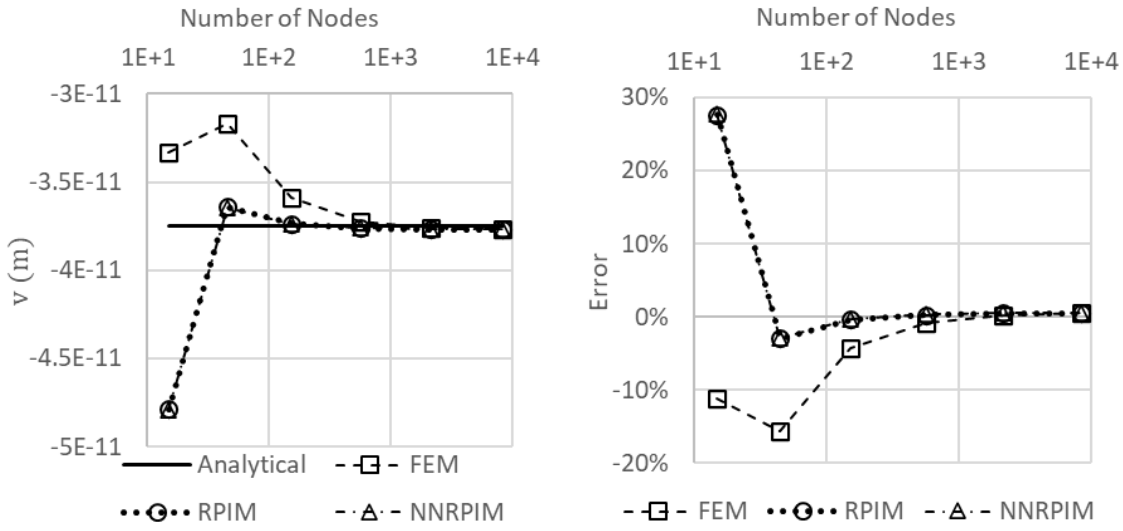

(a) (b)

Figure 21 - (a) vertical displacement at point A; (b) vertical displacement error

The convergence behaviour of the stress fields was also examined. Specifically, the normal stress σ_{xx} was evaluated along the horizontal centerline $y = D/2$ (Figure 22), and the shear stress τ_{xy} was evaluated along the vertical $x = L/2$ (Figure 23). The stress results reveal similar trends to those observed in the displacement analysis. As the number of nodes increases, all methods converge toward smooth and stable stress distributions.

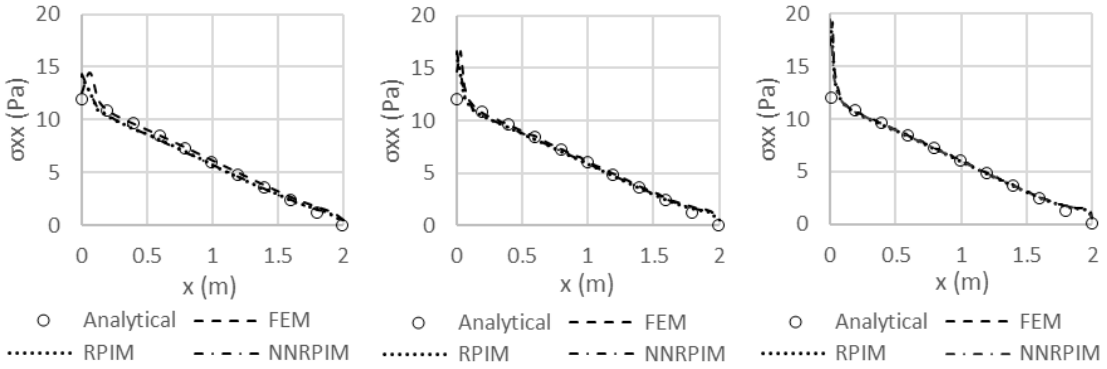

(a) (b) (c)

Figure 22 – Normal stress along x for y = D/2: (a) 561 nodes; (b) 2145 nodes; (c) 8285 nodes

For shear stress all methods capture the overall parabolic results that were expected, with all methods having similar results when comparing with the analytical solution.

The FEM method shows a deviation from the analytical at the midpoint point $y = 0$ when using a coarse mesh, in contrast, both RPIM and NNRPIM have a smoother and closely follow the analytical solution even when using lower nodal densities.

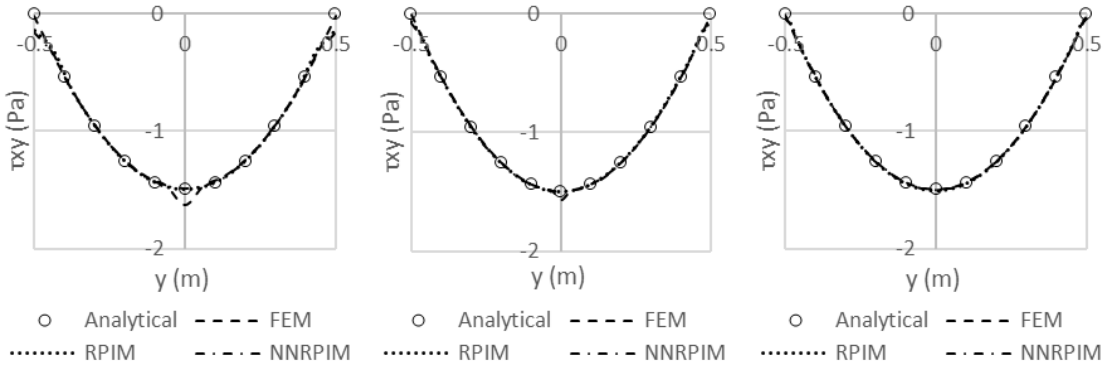

(a) (b) (c)

Figure 23 - Shear stress along y for x = L/2: (a) 561 nodes; (b) 2145 nodes; (c) 8285 nodes

4.2. Structural Optimization Benchmark

In this section, a structural optimization method is combined with the previous numerical methods (FEM, RPIM and NNRPIM) to evaluate their performance in structural optimization problems. To evaluate the performance and accuracy of the methods, benchmark examples found in literature were selected as reference cases. These benchmarks provide a known optimal solution that can used as a basis for comparing with the results obtained in the simulations. This study aims to investigate the influence of the mesh on the final design, as well as the impact the of the algorithm parameters on the different numerical methods. In the end, this study aims to demonstrate the effectiveness and practicality of the proposed structural optimization methods.

4.2.1. Michell-type Structure with a Simple Support and Roller Support

The first benchmark problem considered in this study is based on a Michell-type structure, illustrated in Figure 24. The domain consists of a rectangular area with dimensions 10 m in length and 5 m in height. Boundary conditions include a simple support on the left corner and a roller support on the right corner. The structure is subjected to a vertical point load F applied at the center of the bottom edge. The mechanical properties of the material are $E = 1GPa$ and $\nu = 0.3$.

Due to the geometric and loading symmetry of the problem, the computational model can be simplified by analysing only half of the structure. This reduction is achieved by introducing a vertical symmetry plane that divides the domain. Appropriate symmetry constraints are applied along this plane to ensure the mechanical behaviour of the simplified model remains equivalent to the full structure. This approach reduces computational cost while preserving accuracy.

To study the influence of the mesh, the problem was solved with meshes with 20x20, 40x40 and 80x80 nodes. To avoid stress concentrations the boundary conditions and the force were applied to multiple nodes instead of a singular point.

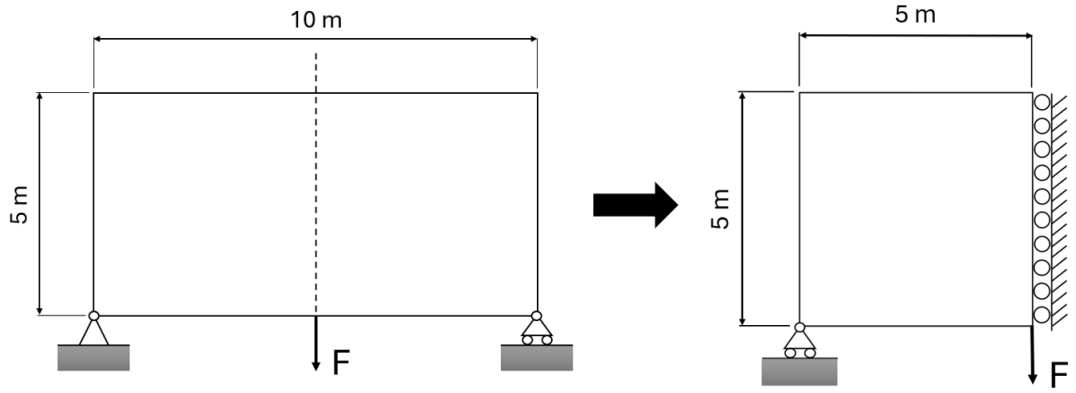

Figure 24 - Michell-type structure with a simple support and roller support

For the structural optimization, an isotropic material model was considered, and the optimization was carried out using the hard-kill method, an approach where elements with low stress are completely removed turning them into voids. The Effective Von Mises stress was adopted as the structural criterion to guide the material removal process. To investigate the influence of algorithmic parameters on the optimization outcome, two different values for the decrease ratio were tested: 5% and 10%. One of the objectives of this study is to evaluate how variations in this parameter affect the convergence and the resulting structural topology. By comparing the final optimized designs obtained for different decrease ratios and numerical methods, it is possible to gain insight into the sensitivity of the optimization algorithm and the robustness of each numerical formulation.

The optimal design for this benchmark problem, as reported in the literature, is shown in Figure 25. This solution serves as a reference configuration that shows the ideal material distribution under the given loading and boundary conditions, making it a valuable benchmark for evaluating the performance of the different numerical and optimization methods. By comparing the results obtained through FEM, RPIM, and NNRPIM with this reference solution, it becomes possible to assess the accuracy of the final topology and the capability of each method to capture the essential structural features of the optimal design.

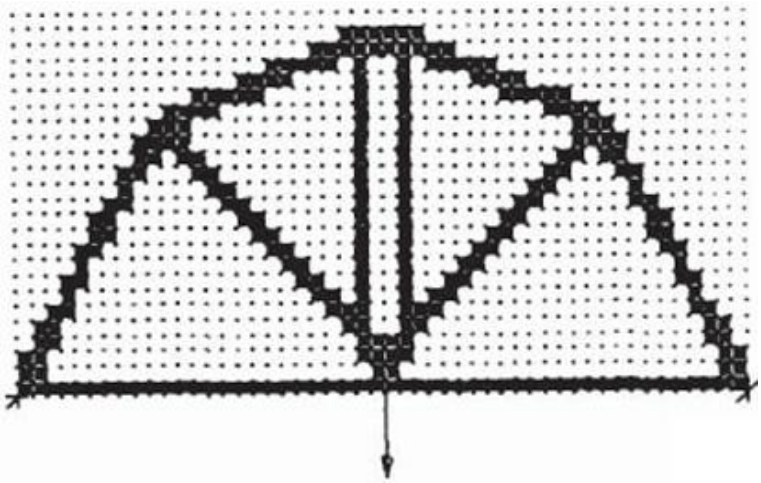

Figure 25 - Optimal topology for Michell type structure with one simple support and one roller *[27]*

The results obtained from the structural optimization simulations conducted using the FEM, RPIM and NNRPIM are presented in Figure 26, Figure 27 and Figure 28 respectively. Each simulation was carried out with varying mesh densities and decrease ratios of 5% and 10%. This approach enables a thorough analysis of how these parameters affect the final topology and the convergence behaviour of the simulations.

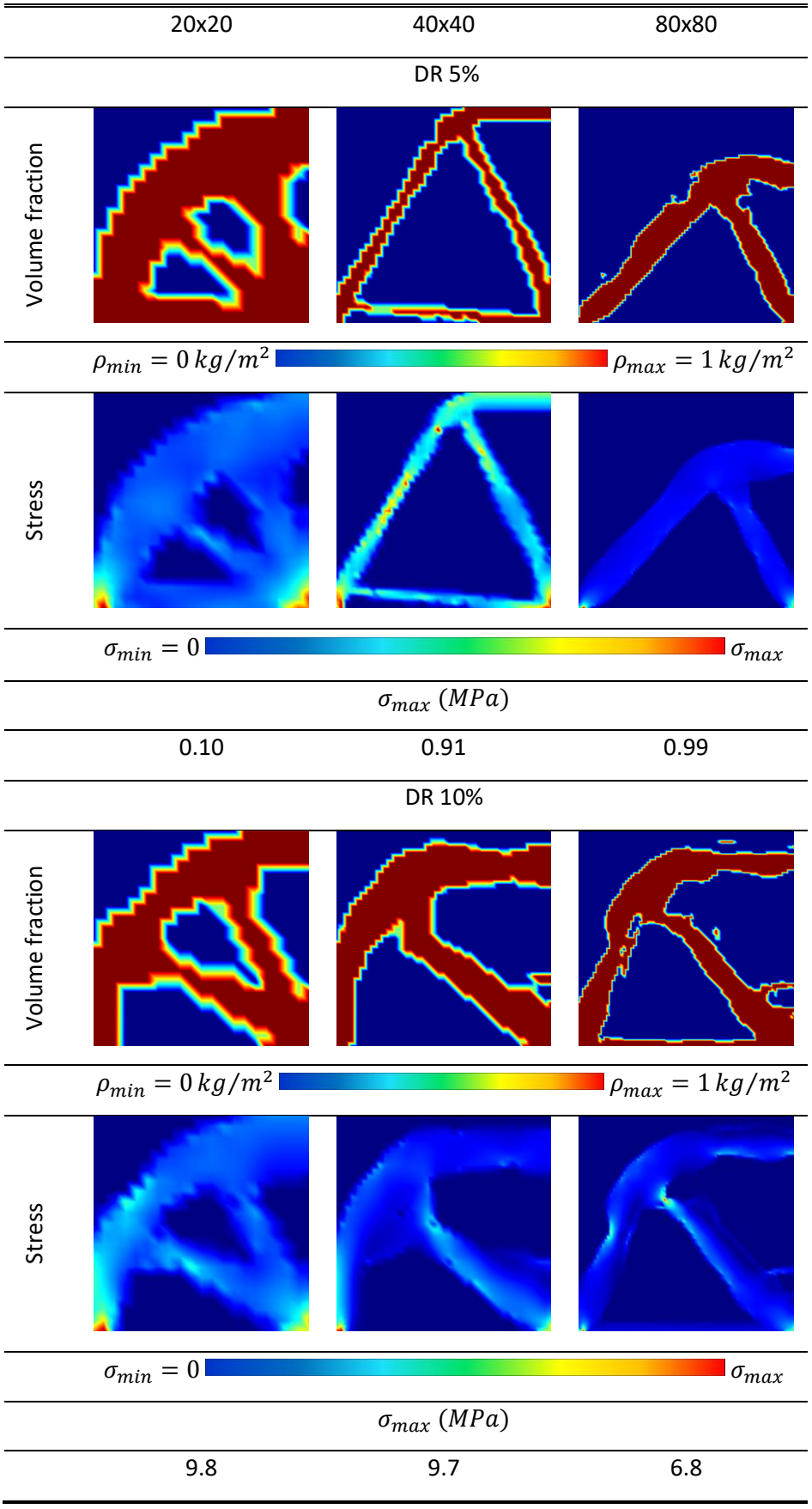

Figure 26 - FEM results for a Michell type structure with one simple support and one roller

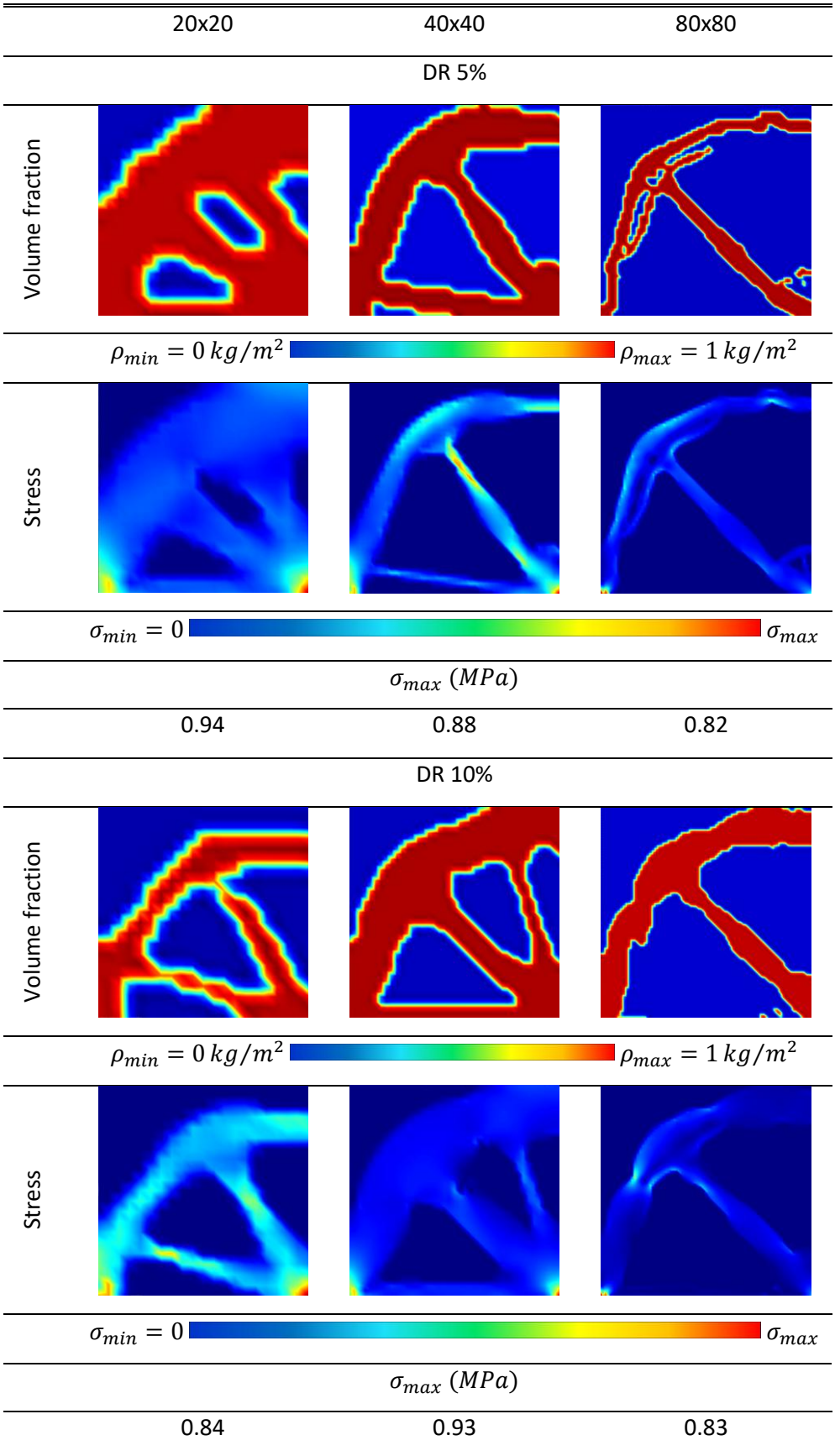

Figure 27 - RPIM results for a Michell type structure with one simple support and one roller

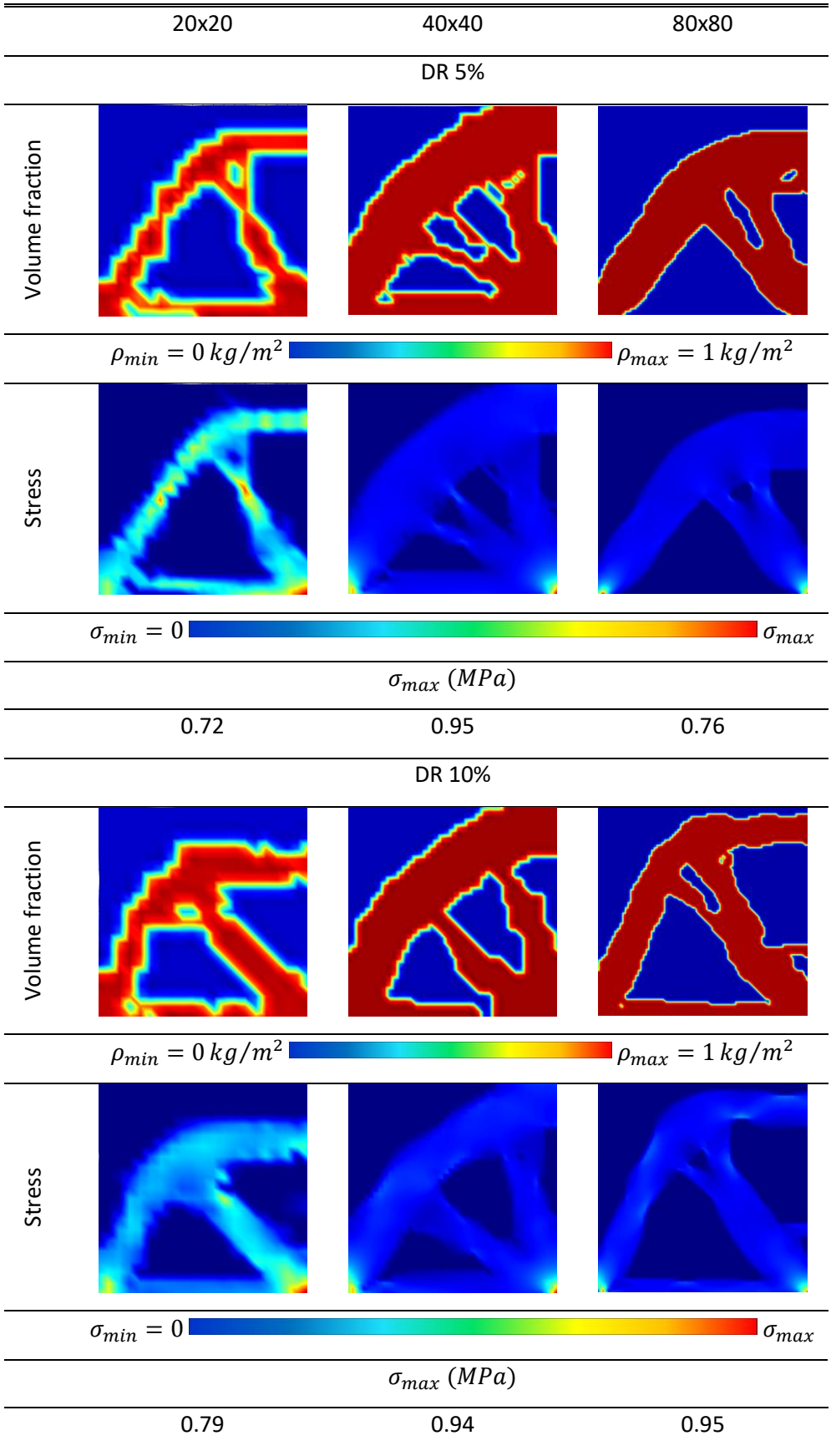

Figure 28 - NNRPIM results for a Michell type structure with one simple support and one roller

The benchmark study was conducted using FEM, RPIM, and NNRPIM methods, with two different decrease ratios (DR) of 5% and 10%, and mesh resolutions of 20×20, 40×40, and 80×80. An analysis of the results indicates no clear pattern emerges regarding which method or DR consistently produces the best solutions.

In some cases, the optimized topologies closely resembled the reference solution found in the literature, successfully reproducing the main structural features of the optimal designs confirming the capability. However, other simulations failed to reproduce these features accurately, resulting in suboptimal or non-ideal material distributions. These discrepancies can be attributed to the chosen decrease ratio and optimization parameters directly affected the rate of material removal, occasionally producing premature convergence to non-ideal solutions. While the reference optimal design reported in the literature typically exhibits a horizontal member, an inclined member, and a vertical member, some of the solutions obtained in this study deviate from this configuration, showing either additional or fewer members. The presence of multiple designs with different geometries may suggest that there are multiple near-optimal solutions capable of satisfying the conditions of the problem, highlighting the non-uniqueness of the optimal topology.

Good results were obtained for all mesh refinements, even with the coarser ones the algorithm was able to approximate the expected topology. But naturally, the solutions obtained with coarser meshes present a lower resolution making the geometry features appear less detailed and defined; however, the essential structural characteristics are still captured.

Interestingly, many of the designs obtained with the finest mesh (80×80) lack the lower member that is present in the reference optimal design. This is somewhat unexpected, as higher mesh resolution would typically be expected to yield results closer to the theoretical optimum. Only the NNRPIM method with a 10% DR, and FEM with a 10% DR, preserved this lower member.

4.2.2. Michell-type Structure with Two Simple Supported Ends

To further investigate the influence of boundary conditions on the structural optimization results, a variation of the first benchmark problem was considered. The setup is identical to the Michell-type structure previously analysed, with the same geometry, loading, and symmetry assumptions. However, instead of using one simple support and one roller support, the structure is now supported by two simple supports, one at each lower corner, this problem is illustrated in Figure 29.

This small but significant change in the boundary conditions alters the way loads are transferred through the structure, potentially influencing the optimal material distribution. As with the original configuration, symmetry was exploited to reduce the computational domain, and equivalent symmetry constraints were applied along the vertical midline.

The objective of this second case is to assess how sensitive the optimization results are to support conditions and to evaluate the robustness of each numerical method (FEM, RPIM, and NNRPIM) under slightly different structural constraints. The optimal design for this benchmark problem, as reported in the literature, is shown in Figure 30.

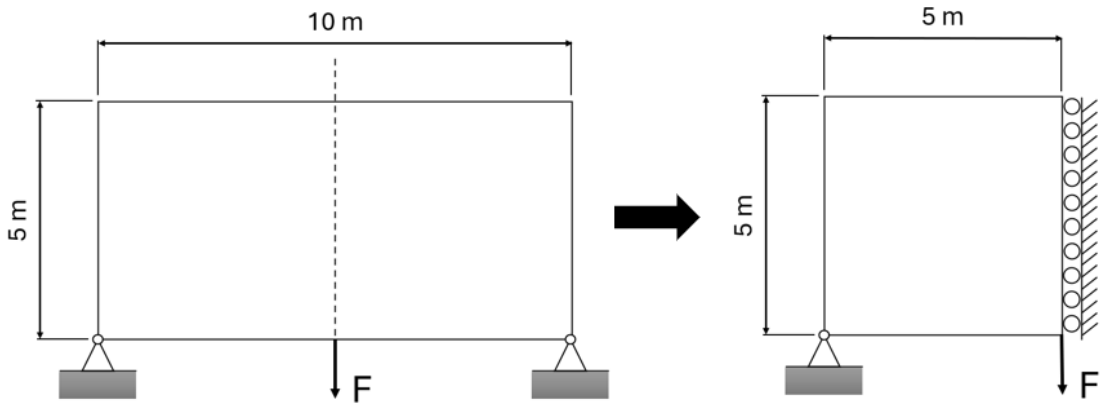

Figure 29 - Michell-type structure with two simple supports

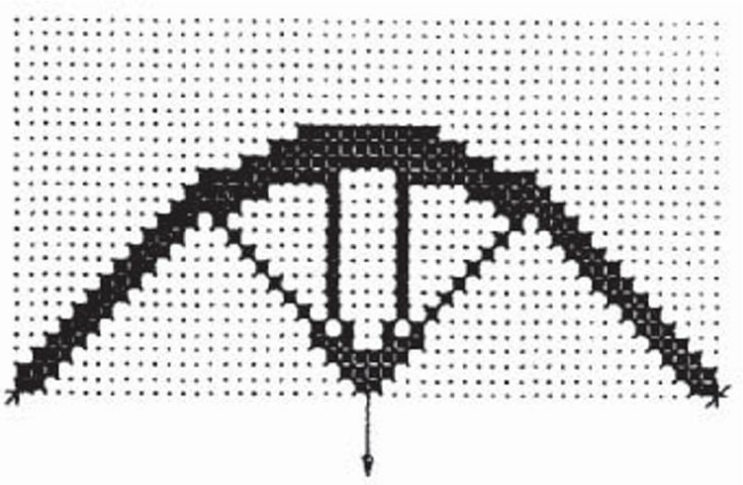

Figure 30 - Optimal topology for a Michell type structure with two simple supports [27]

As in the previous case, simulations were carried out using different mesh densities, decrease ratios and performed using FEM, RPIM and NNRPIM. The results obtained are presented in Figure 31, Figure 32 and Figure 33 respectively.

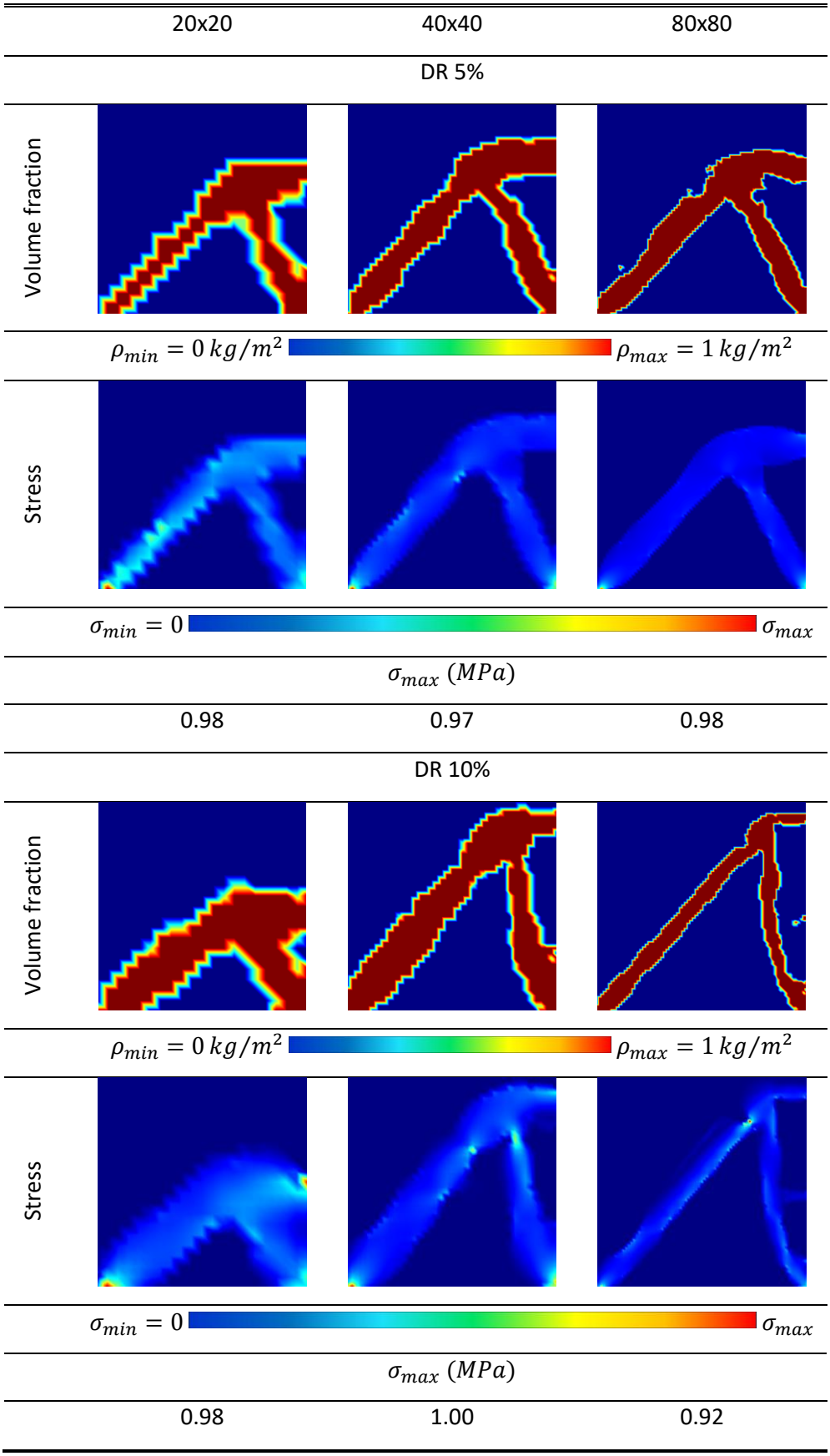

Figure 31 - FEM results for a Michell type structure with two simple supports

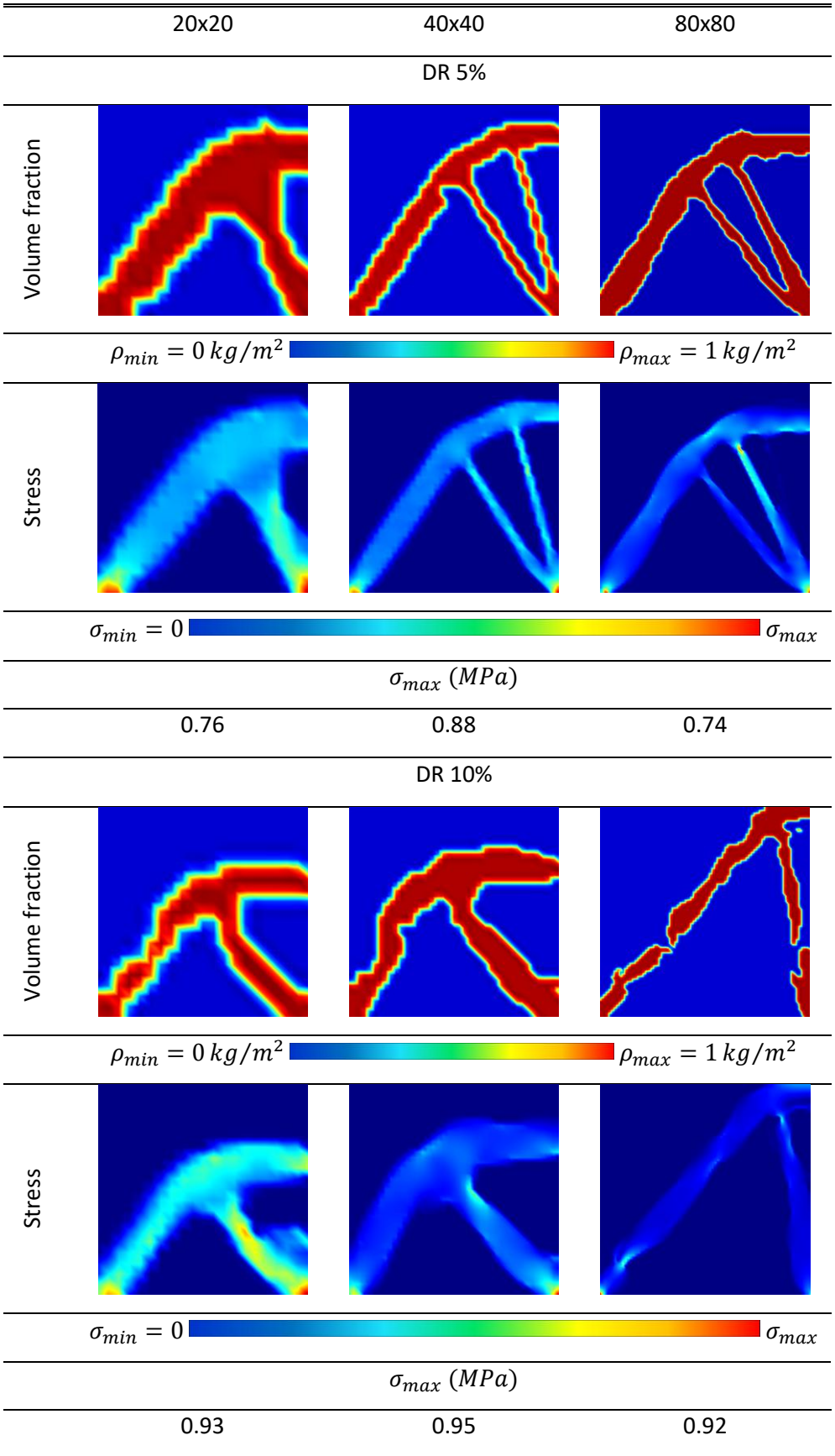

Figure 32 - RPIM results for a Michell type structure with two simple supports

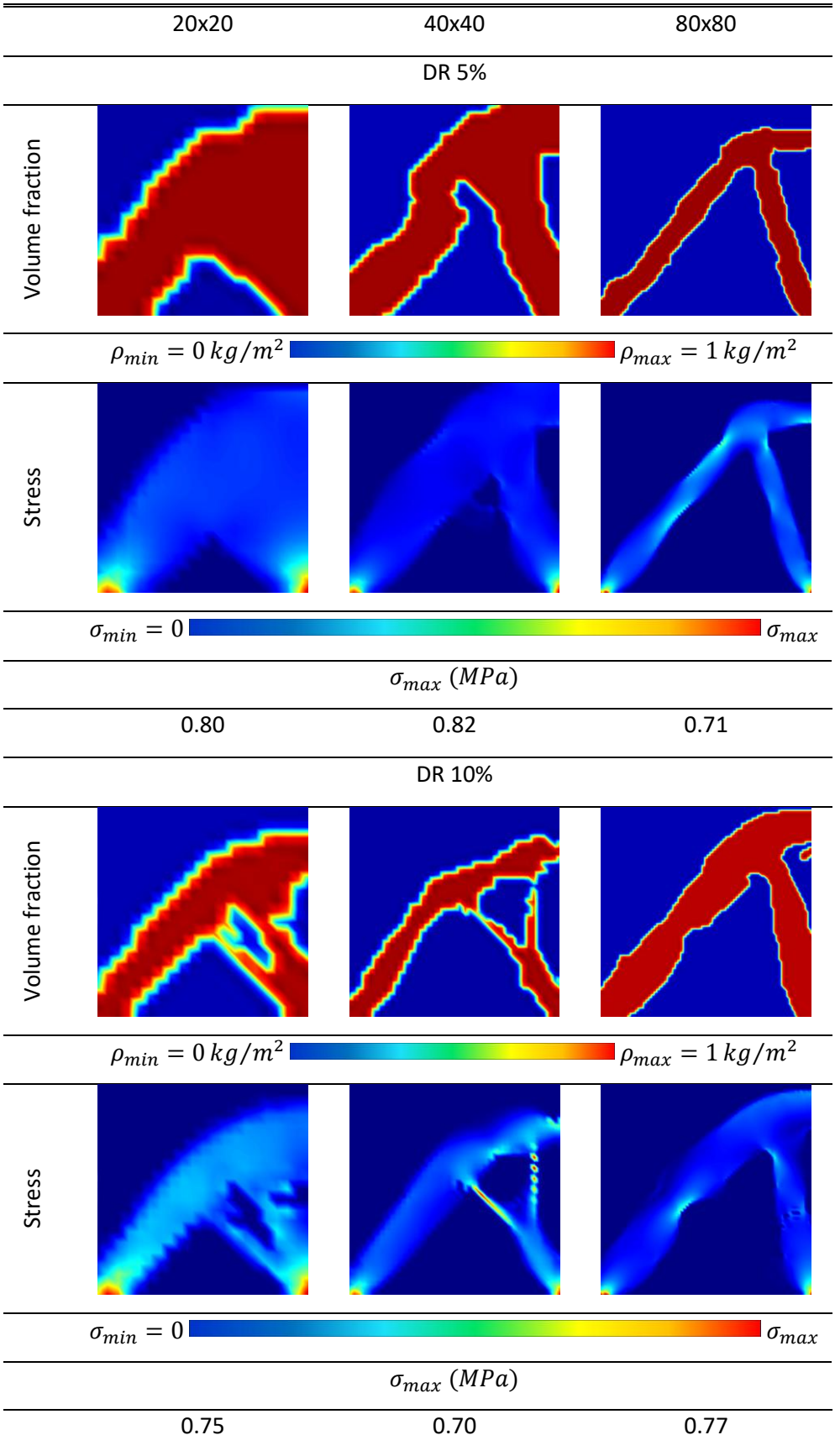

Figure 33 - NNRPIM results for a Michell type structure with two simple supports

The analysis of the second benchmark problem reveals trends that are consistent with those found in the first case. As expected, finer meshes produced results that were more well defined with sharper geometry with a closer resemblance to the reference geometry depicted in the literature. Coarser meshes on the other hand, sometimes failed to capture the geometry clearly, resulting in blurred or incomplete designs, as it can be observed in FEM DR10% and in NNRPIM 5%.

In this case, unlike the first benchmark problem, the variation between the different numerical methods and parameters was less pronounced. Most of the obtained topologies converged towards similar designs, differing mainly in the angles and thickness of structural members. Almost all solutions closely approached the optimal reference solution, which for this problem no longer includes the lower horizontal member present in the first case.

Nonetheless, some deviations can be observed, in the RPIM solutions with 40×40 and 80×80 discretizations and DR 5% presented two inclined members instead of a single member found in most of the other solutions. NNRPIM 40x40 with DR 10% also presents a unique solution, the inclined member splits in 2 other members making an Y shape.

4.2.3. Structural Validation and Performance Assessment

After obtaining the structural optimization results, a set of structural designs were created based on the topologies generated during the simulations. These designs were not strictly identical to the raw optimization outputs of the simulations, as the direct results often contain unrealistic geometries with numerous discontinuities and fragmented material regions. To generate feasible and manufacturable designs, the interpreted topologies were manually refined to ensure continuity and structural integrity while preserving the essential load paths identified in the optimization process.

The selection of geometries for this validation phase followed two main criteria. First, designs that visually appeared to perform better and were closer to the bibliographic solution. Second, a deliberate effort was made to include a variety of topological layouts, representing different design "families" that emerged across the optimization results. This approach allows for a comparative analysis not only of performance, but also of how distinct topological strategies influence stiffness, stress distribution, and material efficiency.

During the post-processing of the geometries, an additional constraint was applied: all designs were adjusted to have approximately the same optimized area, and consequently, similar estimated mass. This ensures that the comparison of mechanical performance, particularly stiffness, is not biased by differences in material quantity.

The refined geometries were then imported into FEMAP, where a finite element mesh was generated for each design. Subsequently, the meshed models were exported and analysed in FEMAS, where static simulations were performed under the same loading and boundary conditions as those used in the optimization phase.

From these simulations, the stress fields were extracted and compared with those obtained in the original optimized solutions to evaluate how well the reconstructed geometries retained

the mechanical performance characteristics. Additionally, the vertical displacement at a selected reference point, the reference point used is show in Figure 34.

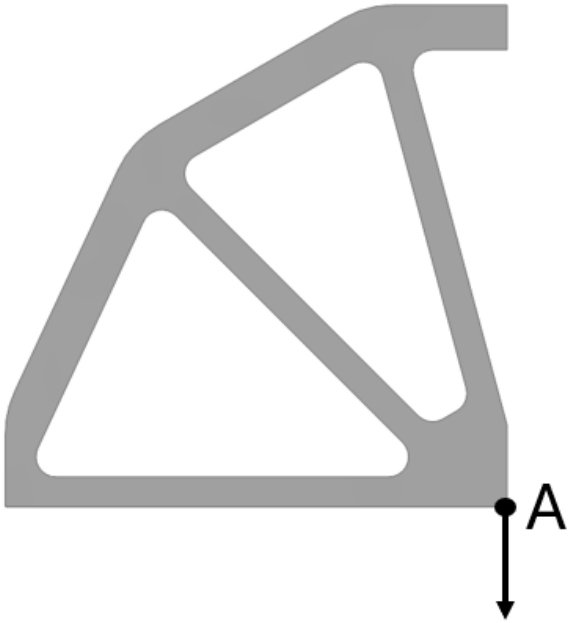

Figure 34 - Reference Point used for Vertical Displacement

The stiffness was calculated as the ratio between the applied force and the measured vertical displacement:

$$k = \frac{F}{u_v} \tag{4.44}$$

Where F is the applied force and u_v is the vertical displacement at point A. To compare the performance of each design independently of its mass, the specific stiffness was calculated as:

$$k_n = \frac{k}{m} = \frac{F}{u_v \cdot m} \tag{4.45}$$

Where m is the mass of the structure. This metric allows a comparison of the efficiency of each structure in terms of stiffness per unit of mass.

80x80 FEM DR10%	40x40 RPIM DR10%	80x80 RPIM DR10%	80x80 NNRPIM DR10%
Geometry			
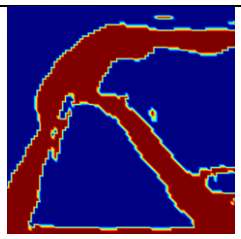	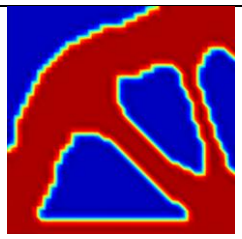	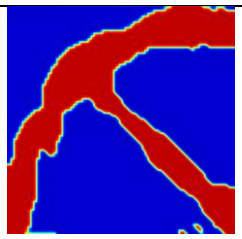	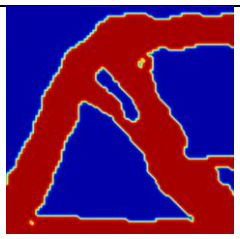
$\rho_{min} = 0\,kg/m^2$  $\rho_{max} = 1\,kg/m^2$			
Post Processed Geometries			
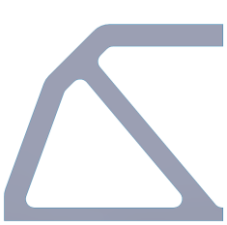	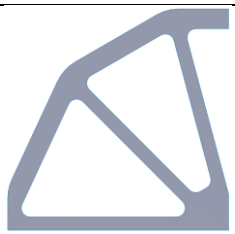		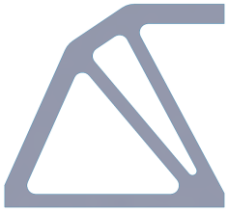
Stress Field			
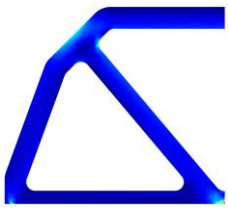	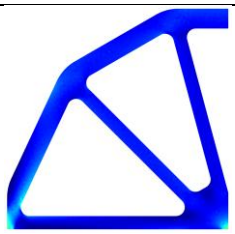	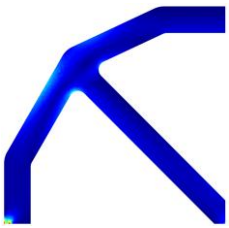	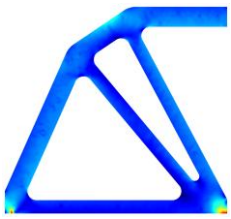
$\sigma_{min} = 0$  σ_{max}			
$\sigma_{max}\ (MPa)$			
0.72	0.75	0.87	0.76
Mass (kg)			
7.08	7.60	7.08	7.45
Vertical Displacement at point A (mm)			
-2.252E-05	-3.903E-05	-1.430E-04	-3.796E-05
Specific Stiffness [(N/m)/kg]			
6.272E+03	3.371E+03	9.877E+02	3.536E+03

Figure 35 - Structural optimization for the structure with a Simple Support and Roller Support

The specific stiffness values obtained from the validated geometries show a clear variation depending on the numerical method used during the topology optimization phase. Despite all geometries being adjusted to have similar mass, the resulting stiffness-to-mass ratio differs significantly across the designs.

These differences are not surprising given the visual disparity between the topologies. Even after post-processing, the designs exhibit significant variations in geometry, which directly affect the stiffness characteristics.

Across the simulations the stress distribution is very homogeneous, with a big percentage of the area indicating low stress intensity. This uniformity suggests that the material is efficiently distributed across the structure.

From this comparison the FEM based design stands out as the one with highest stiffness followed by 40x40 RPIM 0.10 and 80x80 NNRPIM 0.10 that have similar stiffnesses. As expected, the 80×80 RPIM 0.10 design shows the lowest stiffness, aligning with its greater visual deviation from the optimal patterns described in the literature.

Overall, the results confirm that stiffness is highly sensitive to geometric configuration, and not necessarily to the numerical method alone. Individual design quality and interpretation have a strong influence on final performance.

80x80 FEM DR5%	80x80 RPIM DR5%	80x80 NNRPIM DR5%
Geometry		
	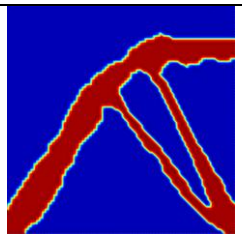	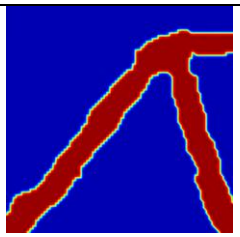
$\rho_{min} = 0\ kg/m^2$  $\rho_{max} = 1\ kg/m^2$		
Post Processed Geometries		
		
Stress Field		
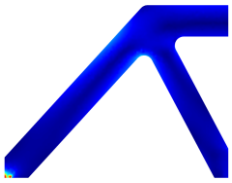	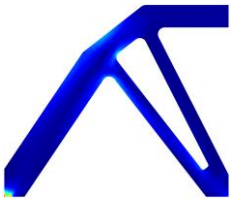	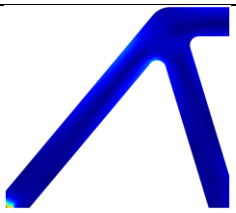
σ_{min}  σ_{max}		
$\sigma_{max}\ (MPa)$		
0.81	0.77	0.86
Mass (kg)		
6.38	6.62	6.88
Vertical Displacement at point A (mm)		
-5.023E-04	-3.157E-04	-7.196E-04
Specific Stiffness [(N/m)/kg]		
3.120E+02	4.785E+02	2.020E+02

Figure 36 - Structural optimization for the structure with two simple supports

The results reveal that the RPIM-based design achieved the highest specific stiffness, followed by FEM, and finally NNRPIM. The stress fields again appear relatively uniform, with most of the structures displaying low stress intensities. However, in this case, the differences in the geometry particularly in the RPIM design, which introduces two diagonal members seem to have provided a more efficient load path, resulting in a higher stiffness-to-mass ratio.

4.3. Structural Optimization of an Engine Rod

Structural optimization algorithms can be used in numerous industrial applications and mechanical designs, where the goal is often to reduce the component weight and cost while maintaining performance. One particularly relevant example is the optimization of an engine connecting rod, a critical component subjected to cyclic loading and strict design constraints. In this section, a practical study is conducted on the structural optimization of a connecting rod. Engine rods are typically made from high strength materials such as steel alloys or aluminium. In this study, the connecting rod is assumed to be made from structural steel, and typical material properties were selected for the simulations. The following material properties were considered: $E = 200GPa$; $\nu = 0.3$; $\sigma_y = 750MPa$. The initial rod geometry was designed in SolidWorks and then imported to FEMAP, where the mesh was created, that model was the imported to FEMAS, where the structural optimization was performed.

Three distinct optimization strategies were defined, each with different design domains, that is, regions were the algorithm is free to add and remove material, and non-design regions, where the area must be preserved due to functional or manufacturing constraints. This approach allows for a comparative analysis of how the restriction of the design domain affects the final topological result. The different strategies can be seen in Figure 37.

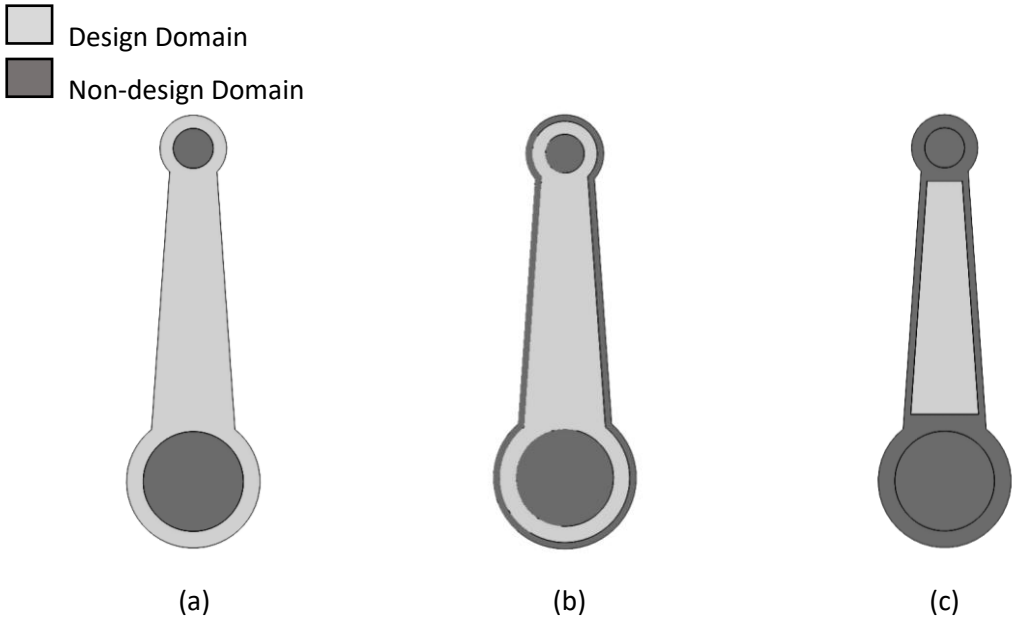

Figure 37 - Optimization strategies with different design domains

For all three design domain, a comparable mesh refinement was used to ensure consistency across the simulations. The element size was kept constant, which results in similar mesh density for all cases. The generated meshes contained: 4175 nodes and 8014 elements for case (a), 4969 nodes and 9588 elements for case (b), and 4064 nodes and 7792 elements for case (c). This ensures that the observed differences in the optimized results arise primarily from the definition of the design and non-design domains rather than from mesh discretization effects.

Figure 38 illustrates the engine rod problem, including its main dimensions and forces applied and boundary conditions. To simulate the connection to the crankshaft, the internal surface of the lower ring is constrained. Multiple nodes along this surface were constrained in both u and v directions. The load is applied at the upper ring where the piston is connected, this load has two components: F_x and F_y. Since the connecting rod is subject to rotating motion in a real engine, the direction and magnitude of the forces vary dynamically. To approximate this effect, different loading configurations were used: the vertical force F_y is fixed at 1 N, while the horizontal component F_x varies incrementally from 0 to 0.5 N in steps of 0.1 N as shown in Table 1.

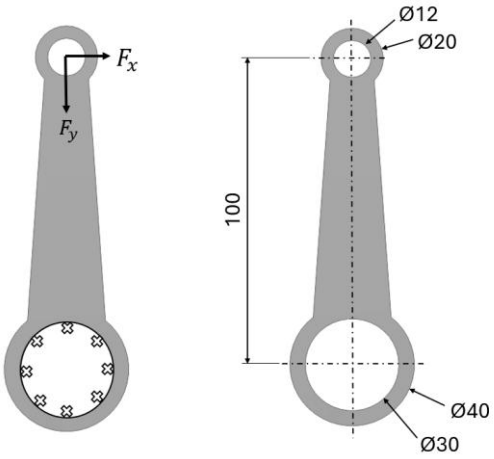

Figure 38 - Engine rod design problem

Table 1 - Engine rod loading configuration

Load case	$F_x\ (N)$	$F_y\ (N)$
1	0	1
2	0.1	1
3	0.2	1
4	0.3	1
5	0.4	1
6	0.5	1

The optimization simulations of the engine rod were carried out using the three numerical methods under study: FEM, RPIM, and NNRPIM. For each method, a DR of 10% was used. The optimization results obtained from these simulations are summarized in Figure 39, Figure 40

and Figure 41 for each method respectively and design domain (a), Figure 42, Figure 43 and Figure 44 for each method respectively and design domain (b) and Figure 45, Figure 46 and Figure 47 for each method respectively and design domain (c).

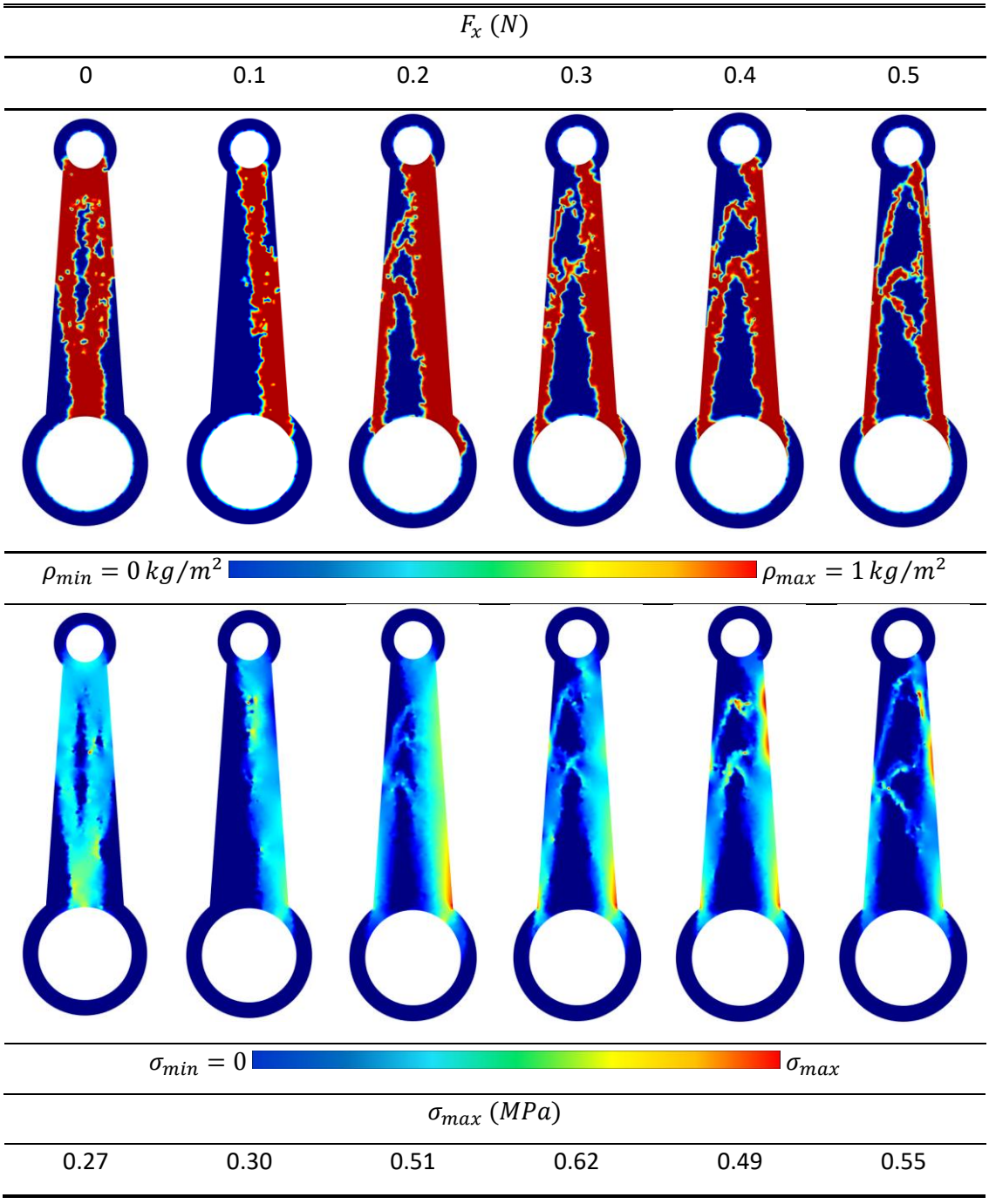

Figure 39 - (a) FEM - Engine rod optimization using strategy (a) and FEM

$F_x\ (N)$					
0	0.1	0.2	0.3	0.4	0.5
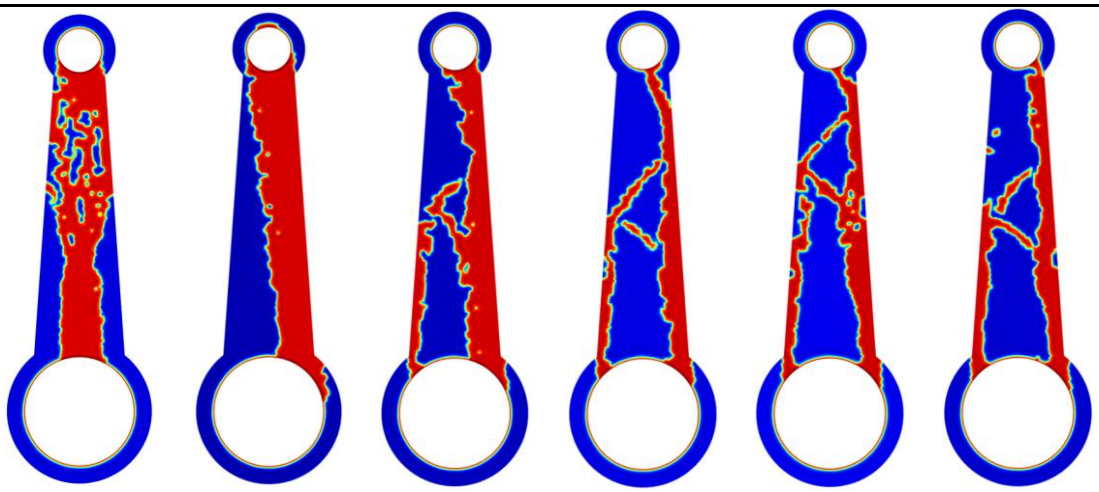					
$\rho_{min} = 0\ kg/m^2$  $\rho_{max} = 1\ kg/m^2$					
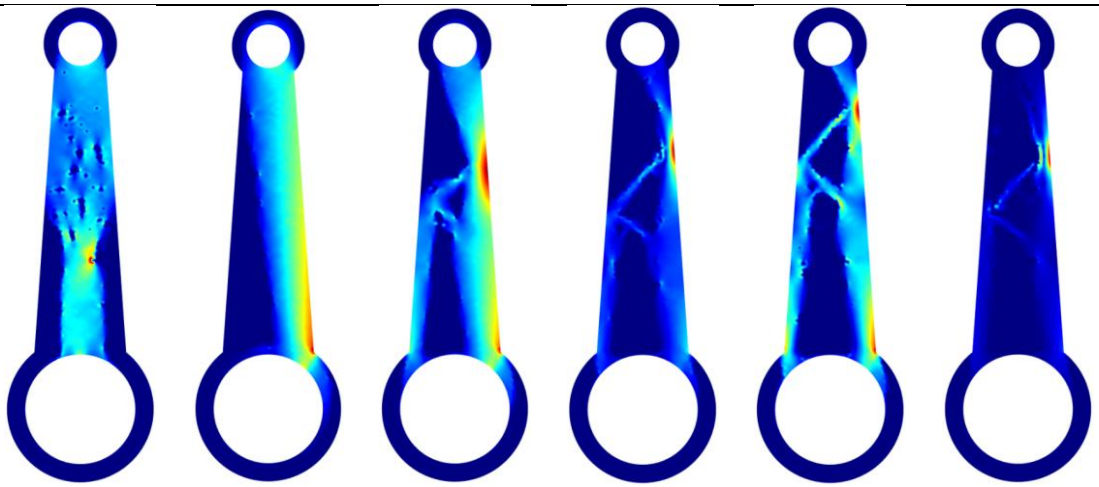					
$\sigma_{min} = 0$  σ_{max}					
$\sigma_{max}\ (MPa)$					
0.39	0.36	0.56	0.50	0.59	0.53

Figure 40 - (a) RPIM - Engine rod optimization using strategy (a) and RPIM

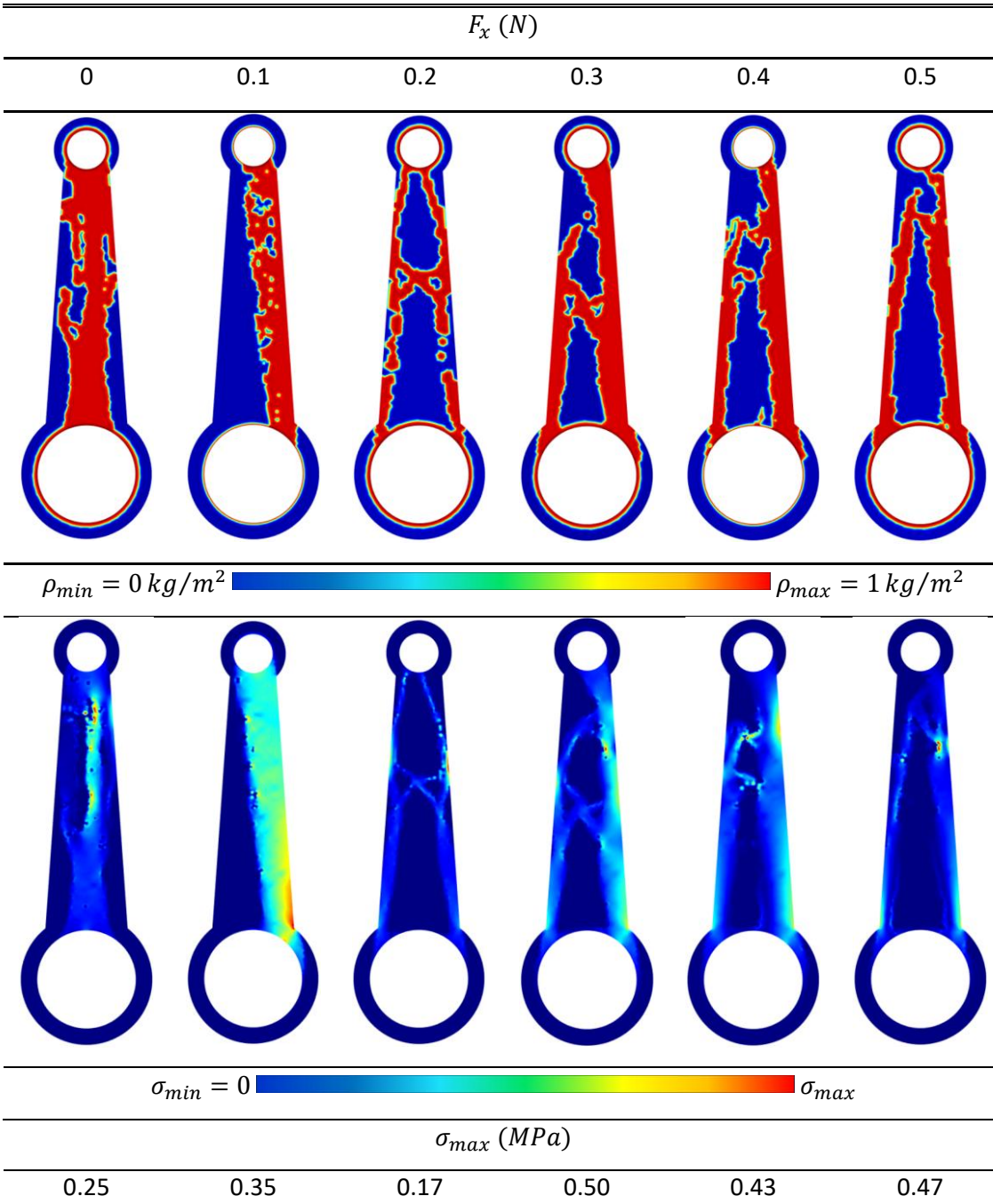

Figure 41 - (a) NNRPIM - Engine rod optimization using strategy (a) and NNRPIM

$F_x\ (N)$					
0	0.1	0.2	0.3	0.4	0.5
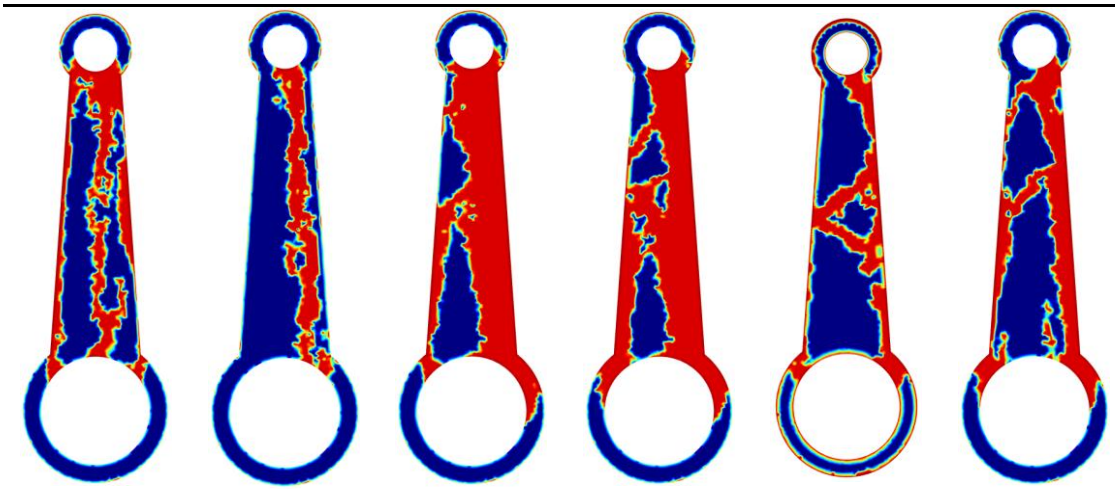					
$\rho_{min} = 0\ kg/m^2$  $\rho_{max} = 1\ kg/m^2$					
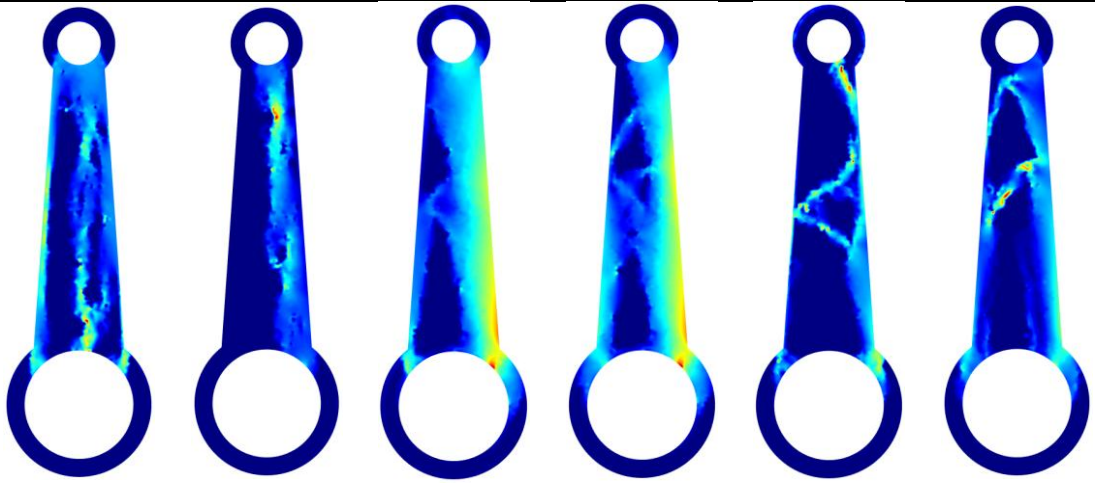					
$\sigma_{min} = 0$  σ_{max}					
$\sigma_{max}\ (MPa)$					
0.32	0.46	0.35	0.40	0.42	0.43

Figure 42 - (b) FEM - Engine rod optimization using strategy (b) and FEM

$F_x\ (N)$					
0	0.1	0.2	0.3	0.4	0.5

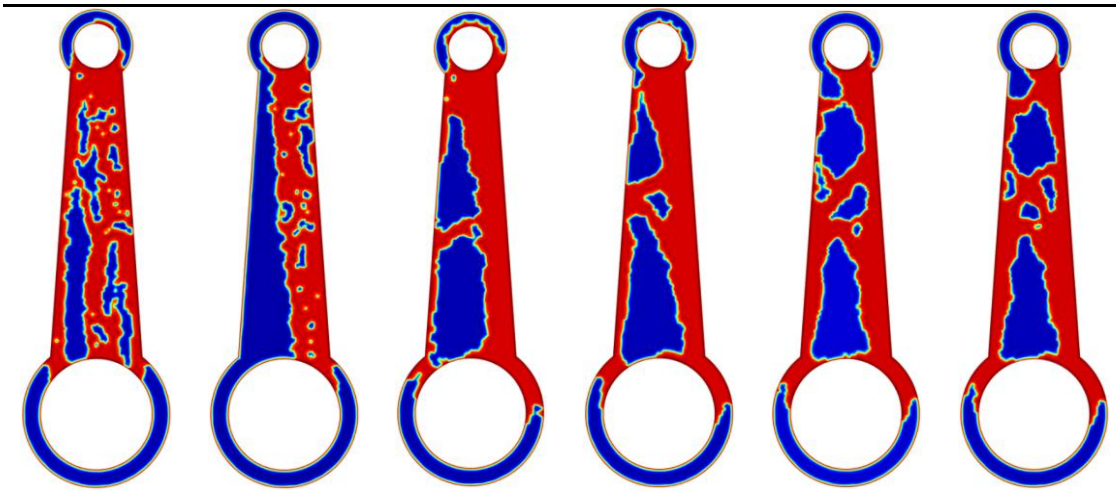

$\rho_{min} = 0\ kg/m^2$ $\rho_{max} = 1\ kg/m^2$

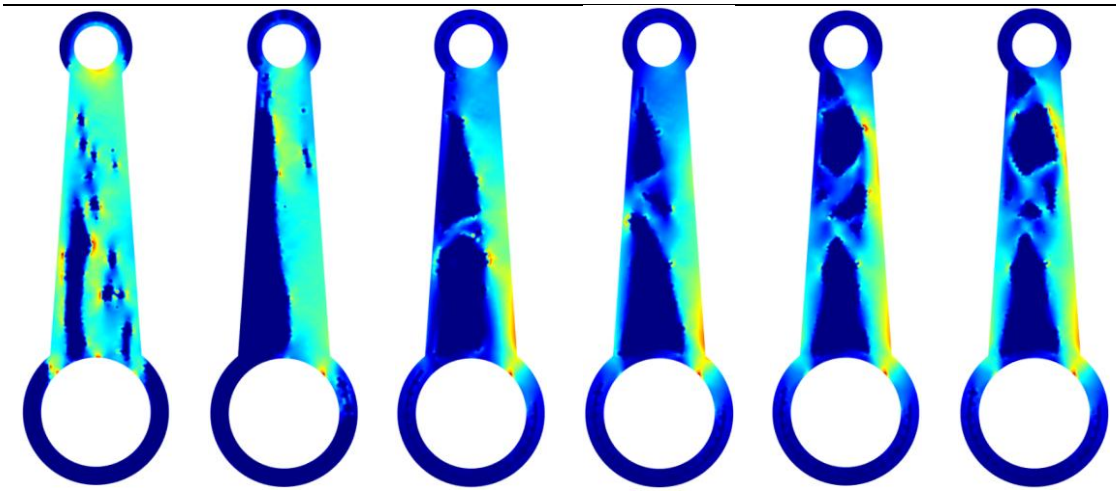

$\sigma_{min} = 0$ σ_{max}

$\sigma_{max}\ (MPa)$					
0.20	0.30	0.43	0.52	0.52	0.53

Figure 43 - (b) RPIM - Engine rod optimization using strategy (b) and RPIM

$F_x\ (N)$					
0	0.1	0.2	0.3	0.4	0.5

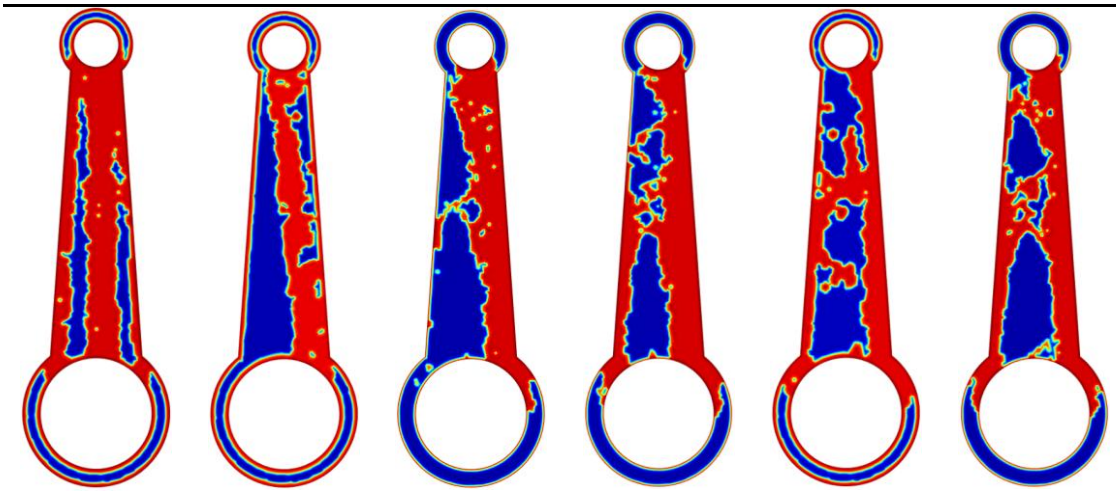

$\rho_{min} = 0\ kg/m^2$ $\rho_{max} = 1\ kg/m^2$

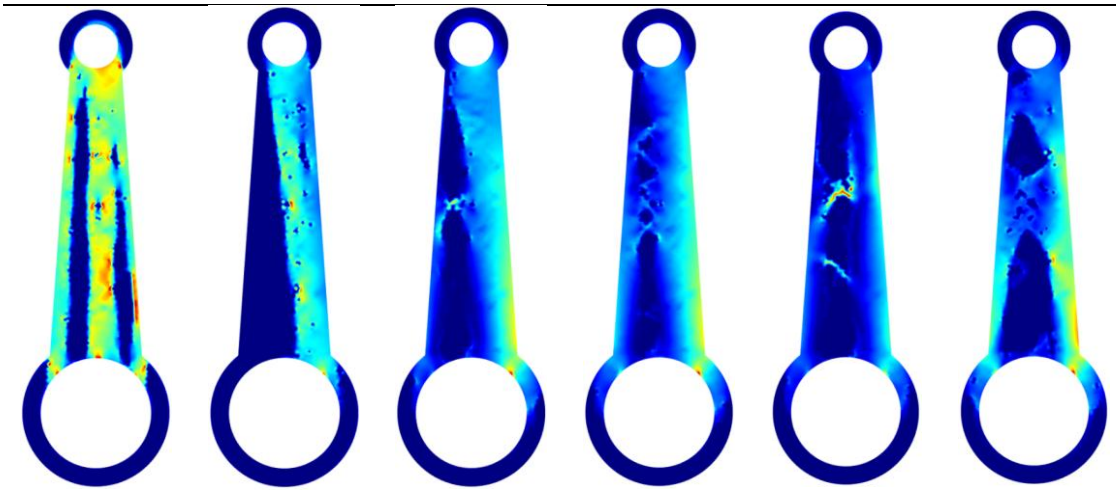

$\sigma_{min} = 0$ σ_{max}

$\sigma_{max}\ (MPa)$					
0.19	0.38	0.43	0.49	0.33	0.51

Figure 44 - (b) NNRPIM - Engine rod optimization using strategy (b) and NNRPIM

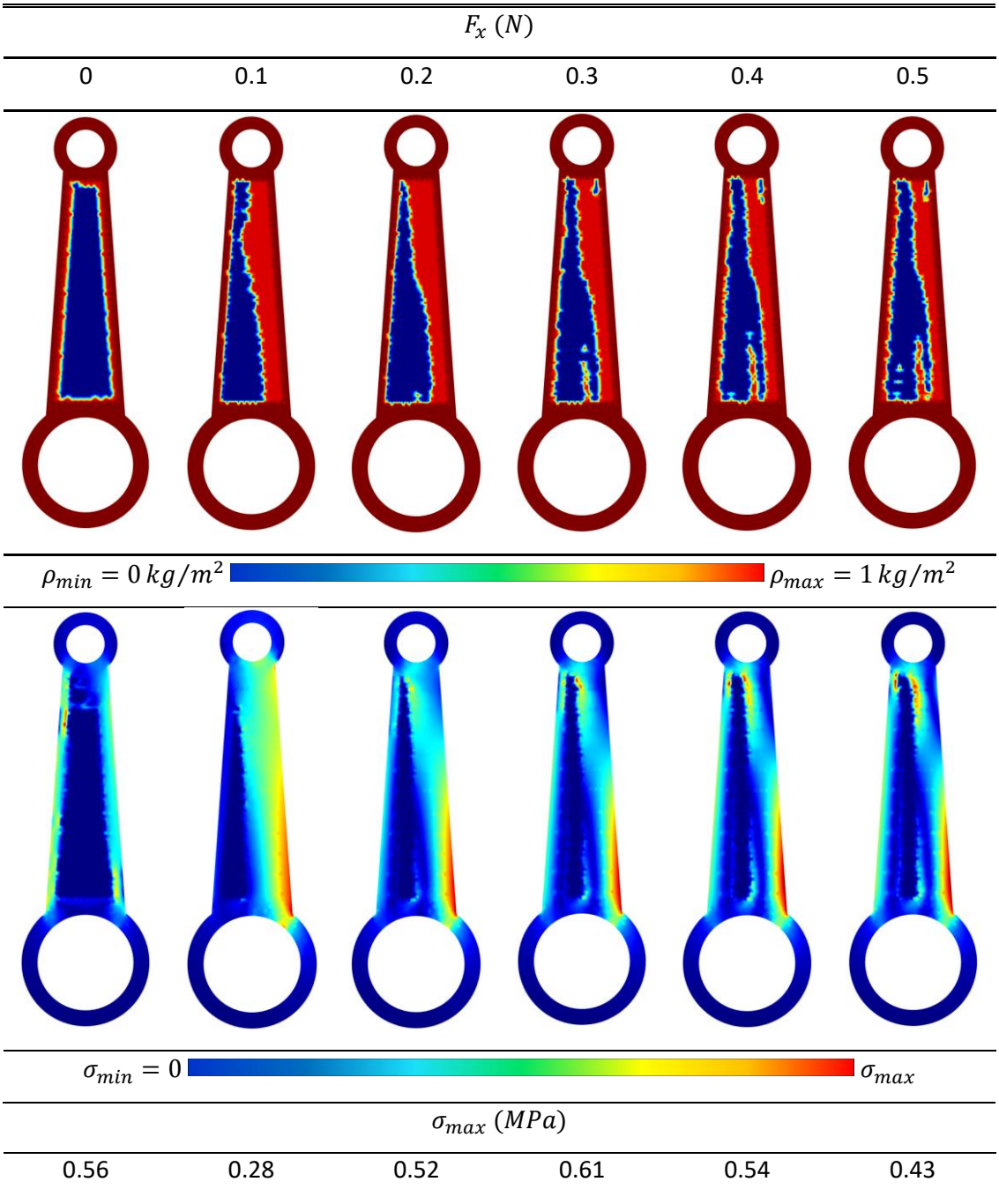

Figure 45 - (c) FEM - Engine rod optimization using strategy (c) and FEM

$F_x\ (N)$					
0	0.1	0.2	0.3	0.4	0.5
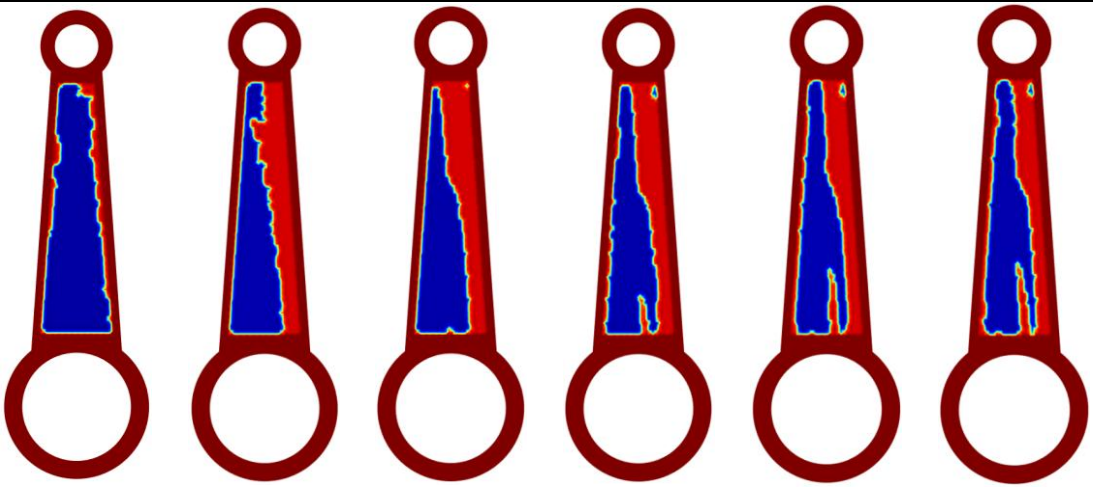					
$\rho_{min} = 0\ kg/m^2$  $\rho_{max} = 1\ kg/m^2$					
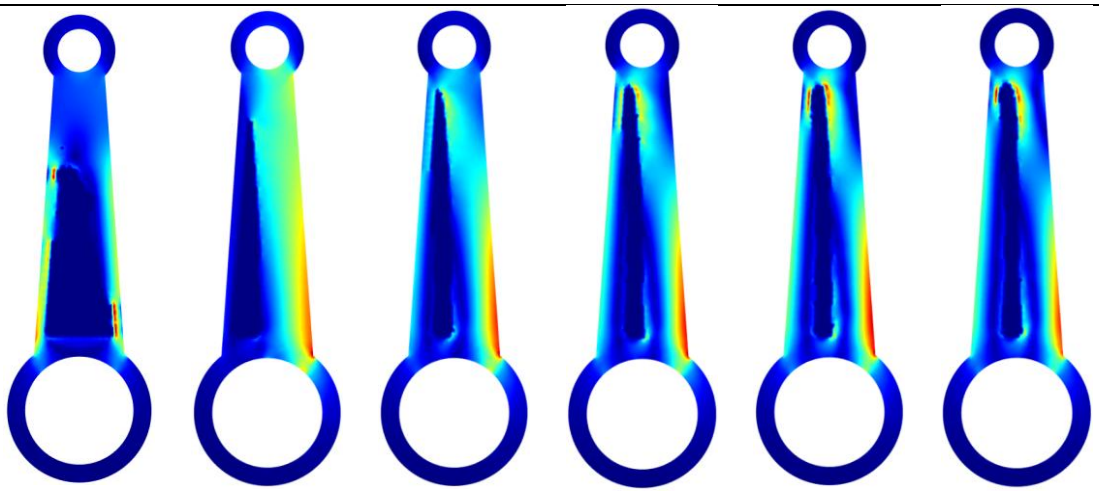					
$\sigma_{min} = 0$  σ_{max}					
$\sigma_{max}\ (MPa)$					
0.50	0.31	0.56	0.65	0.47	0.54

Figure 46 - (c) RPIM - Engine rod optimization using strategy (c) and RPIM

$F_x\ (N)$					
0	0.1	0.2	0.3	0.4	0.5
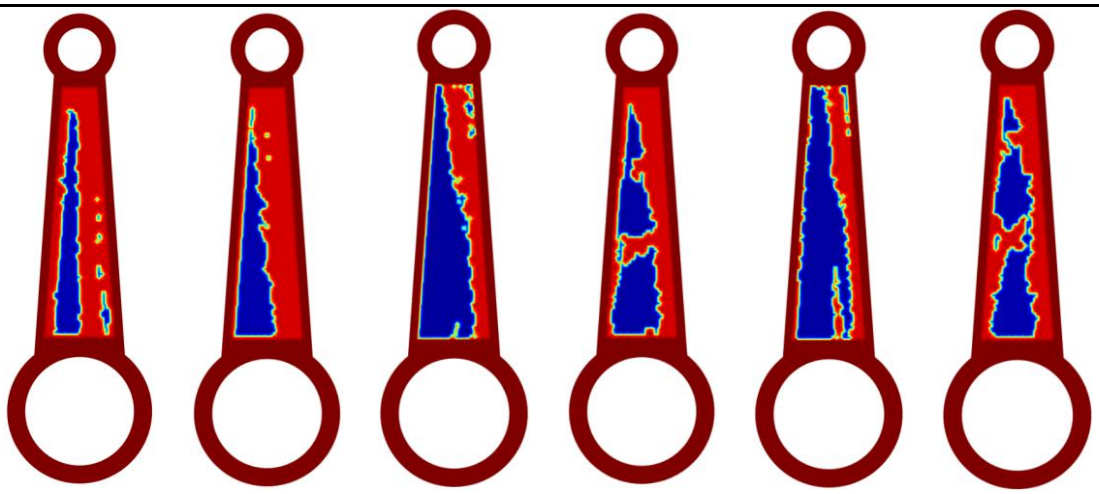					
$\rho_{min} = 0\ kg/m^2$  $\rho_{max} = 1\ kg/m^2$					
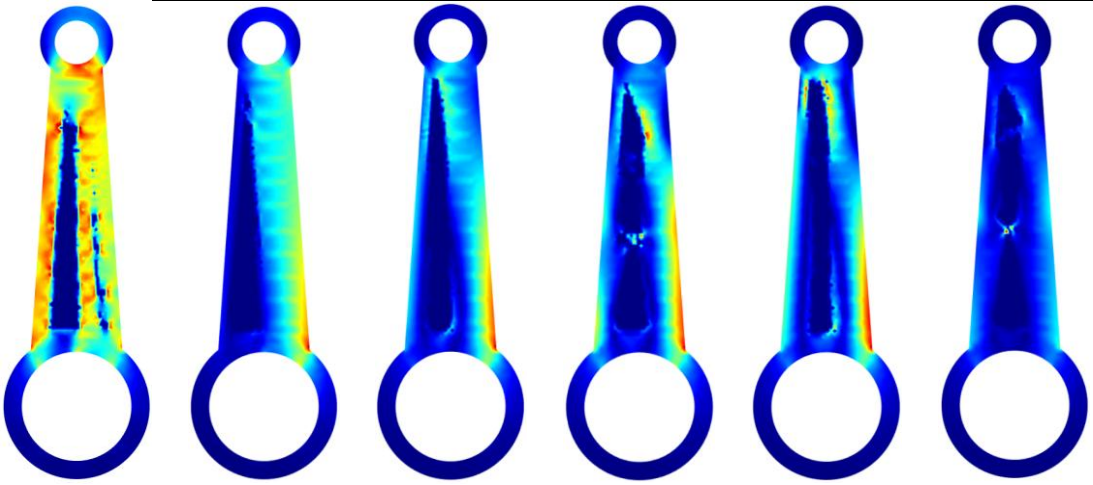					
$\sigma_{min} = 0$  σ_{max}					
$\sigma_{max}\ (MPa)$					
0.31	0.32	0.57	0.41	0.62	0.34

Figure 47 - (c) NNRPIM - Engine rod optimization using strategy (c) and NNRPIM

To facilitate the comparison of the results, the solutions were arranged in a different way. Figure 48 shows the optimized topologies obtained with FEM, RPIM and NNRPIM for the three design domain configurations, considering the most critical loading case with $F_x = 0.5N$. This layout allows for a better visual comparison between the numerical methods and the influence of the design domain definition.

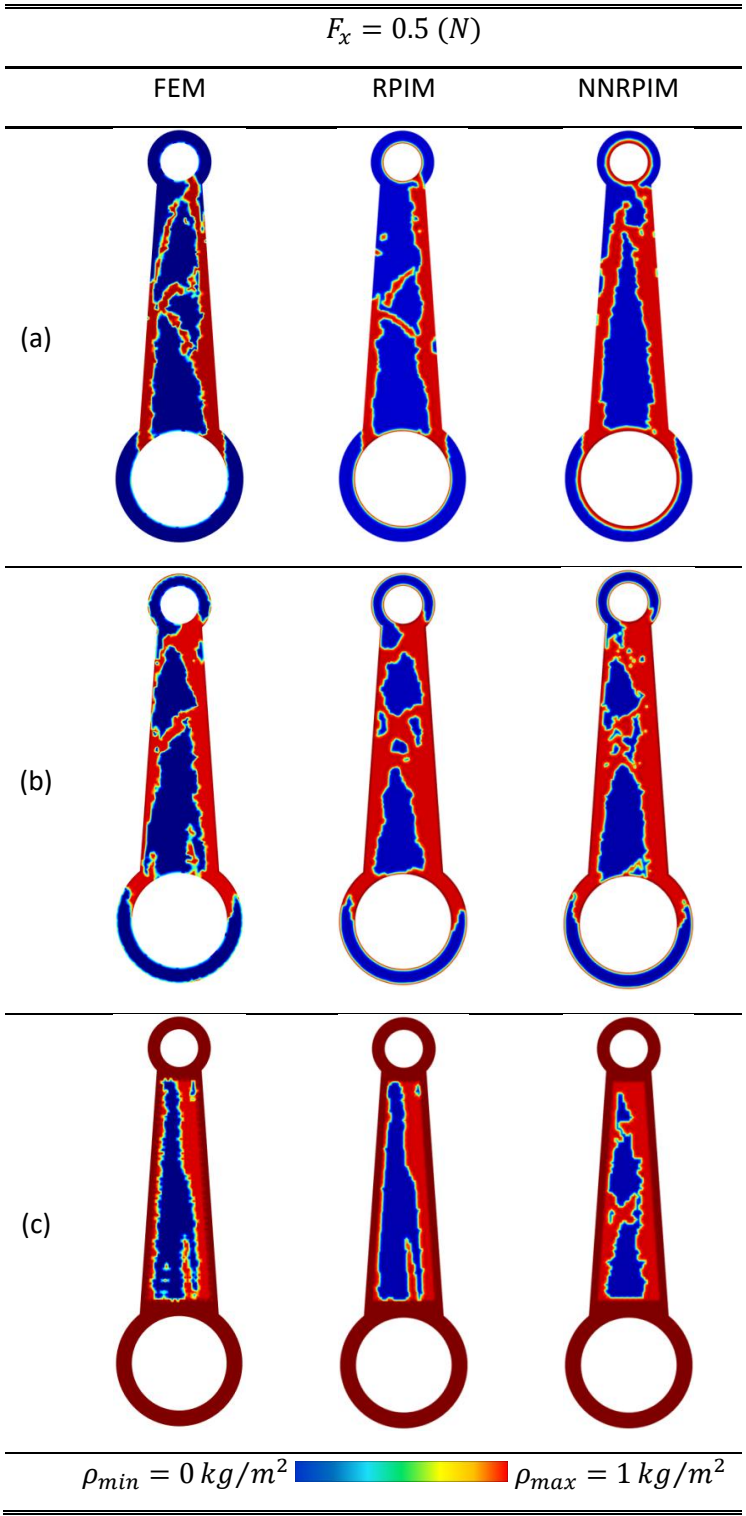

Figure 48 - Engine rod optimization results for Fx=0.5N

4.3.1. Results Discussion

When comparing the three design domain strategies, the approach (c) is the one that diverges the most. In this case the algorithm only that freedom to work with the material in the inner region of the rod, while two “columns” of material were preserved as non-design zones. Since these two “columns” may already be sufficient to withstand the applied loads, the algorithm removed almost all the internal material, resulting in a different and less balanced topology. In hindsight the two preserved “columns” should have been made thinner so the algorithm would be forced to optimize the inner domain in a more efficient way, likely leading to a more optimized design.

In contrast, strategies (a) and (b) produced designs that are more similar to each other, in both these cases the algorithm add less restrictions than in case (c), indicating that perhaps greater freedom of the definition of the design tends to lead to more robust solutions.

Some differences were also observed between the numerical methods (FEM, RPIM and NNRPIM). While some topologies showed some variations depending on the method used, with only a few of them deviating substantially, the general trend suggests that the results converge towards broadly similar solutions.

It should be noted that the connecting rod optimization problem here presented was highly simplified. The loading conditions of an engine rod and significantly more complex involving multiple factors such as inertia effects, bearing contact and alternating tensile and compressive stresses. By simplifying the problem to a two-dimensional static formulation with reduced loading cases, the optimized designs obtained may deviate considerably from a realistic industrial solution. Nevertheless, this simplification provides valuable insight into the capabilities and limitations of the numerical methods and optimization strategies.

It is important to note that, due to the simplifications adopted in the problem formulation, the circular connection zones where rod connects to the piston and crankshaft were removed by the optimization algorithm. This occurs because the contact surface between the rod and the crankshaft was fully constrained, meaning that the nodes in this region had no degrees of freedom. As a result, these areas did not contribute to the structural performance in the simulation, leading the algorithm to eliminate the surrounding material. Their removal in the present study is therefore a consequence of the simplifications introduced, and not a feature of the actual optimized design.

4.3.2. Optimized Design

Based on the algorithm solutions, an optimized topology was designed. The connecting rod geometry was reduced from an initial area of 2162 mm² to an area of 1359 mm², which corresponds to a reduction to 63% of the original area, a significant reduction in material. The optimized geometry is illustrated in Figure 49.

After defining the optimized geometry, numerical simulations were performed to evaluate its structural performance. The model was analysed under the same loading and boundary

conditions as the original connecting rod, and the displacement at critical points as well as the stress distribution fields were extracted. These results allow for a direct comparison of stiffness and stress behaviour between the original and optimized designs. The point used to measure the displacement was point A as shown in Figure 49.

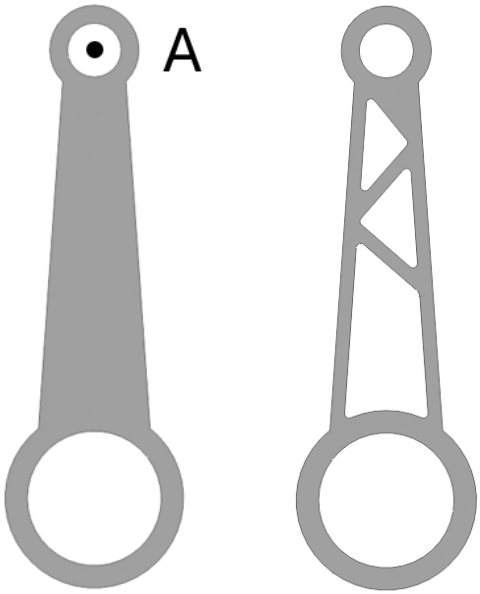

Figure 49 – (a) Original engine rod, (b) Optimized Engine Rod

It is expected that the optimized model will have a lower absolute stiffness compared to the original, as less material is available to carry the loads. However, this reduction in stiffness should be compensated by the corresponding reduction in mass. Therefore, when evaluated in terms of stiffness to mass ratio, the optimized design is expected to show a more efficient structural behaviour than the baseline geometry.

The process required two iterations: in the first trial, the optimized geometry exhibited a lower stiffness than expected. To address this issue, the regions that showed higher stress concentrations were reinforced, and a second iteration was carried out, leading to an improved balance between mass reduction and structural performance. The results obtained are shown in Figure 50, Figure 51 and Figure 52 for design iterations 1, 2 and 3 respectively.

Stress		Displacement	
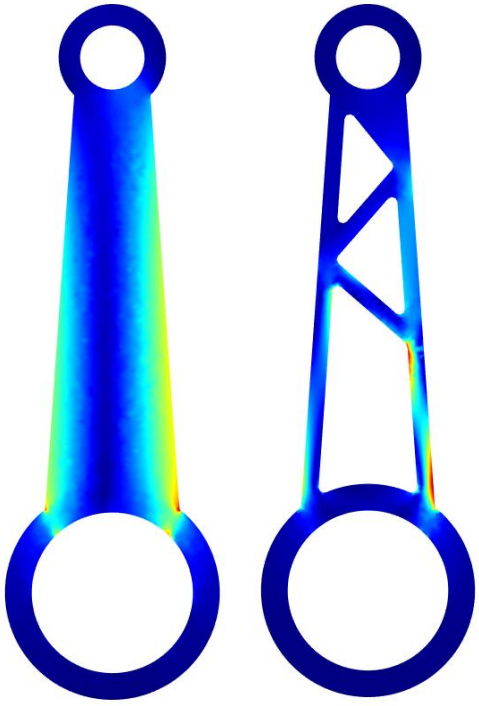		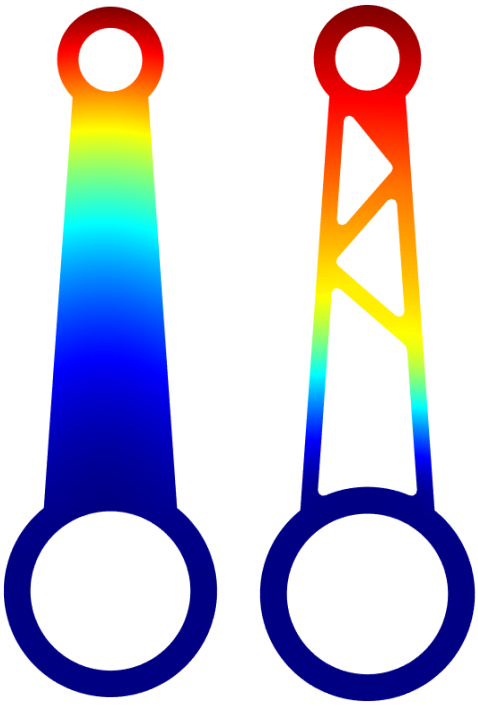	
σ_{min}=0  σ_{max}		$\lvert u\rvert_{min}$  $\lvert u\rvert_{max}$	
σ_{max} (MPa)		$\lvert u\rvert_{max}$ (m)	
0.0714	0.2121	7.24 E-11	1.65 E-10
		Original	Optimized
Mass (kg)		2.162	1.359
Stiffness k (N/m)		1.544 E10	6.776 E9
Specific Stiffness k_n $[(N/m)/kg]$		7.142 E9	4.986 E9

Figure 50 - Engine rod optimization - iteration 1

Stress		Displacement	
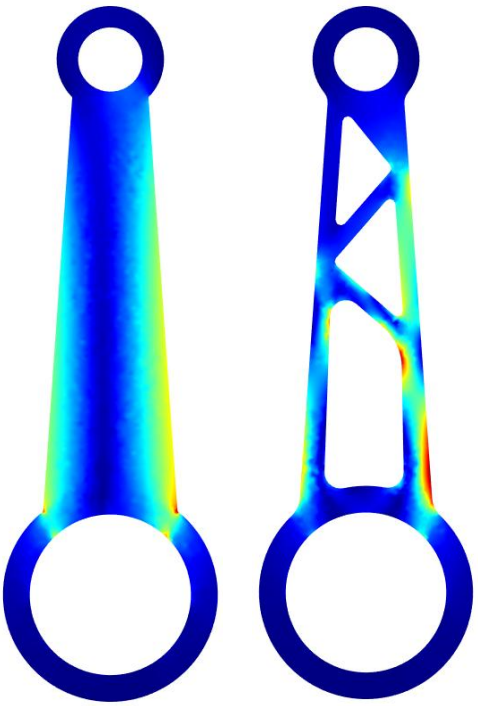		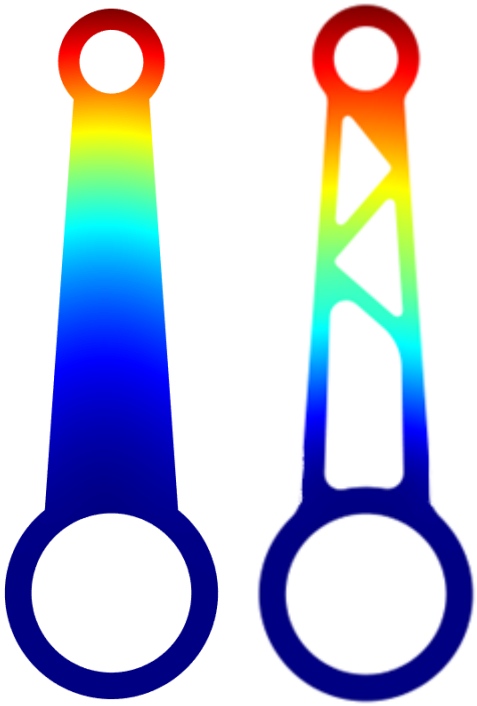	
σ_{min}=0  σ_{max}		$\lvert u\rvert_{min}$  $\lvert u\rvert_{max}$	
σ_{max} (MPa)		$\lvert u\rvert_{max}$ (m)	
0,0714	0,1228	7,24 E-11	1,24 E-10
		Original	Optimized
Mass (kg)		2,162	1,446
Stiffness k (N/m)		1,544 E10	9,016 E9
Specific Stiffness k_n $[(N/m)/kg]$		7.142 E9	6.235 E9

Figure 51 - Engine rod optimization - iteration 2

Stress		Displacement	
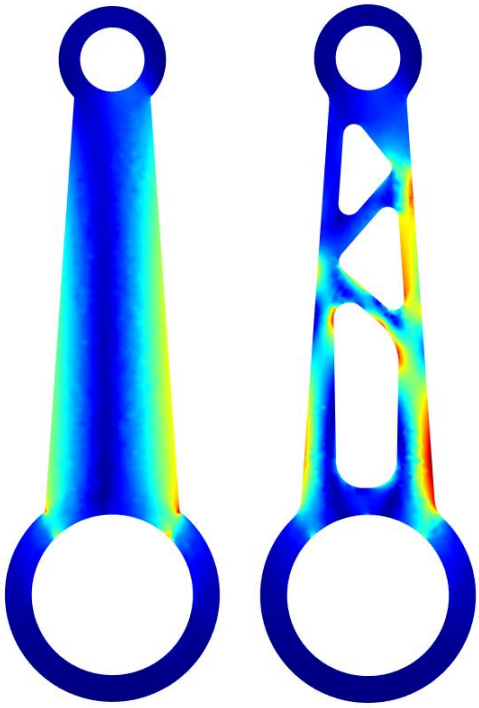		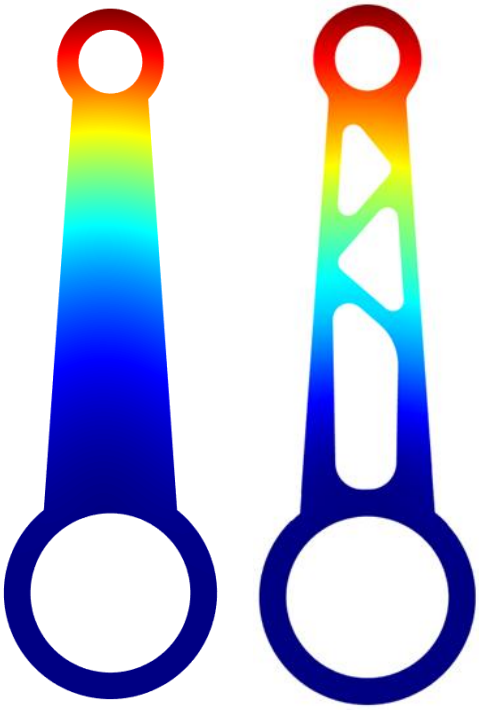	
σ_{min}=0  σ_{max}		$\lvert u\rvert_{min}$  $\lvert u\rvert_{max}$	
σ_{max} (MPa)		$\lvert u\rvert_{max}$ (m)	
0.0714	0.0911	7.24 E-11	1.08 E-10
		Original	Optimized
Mass (kg)		2.162	1.550
Stiffness k (N/m)		1.544 E10	1.035 E10
Specific Stiffness k_n $[(N/m)/kg]$		7.142 E9	6.6779 E9

Figure 52 - Engine rod optimization - iteration 3

4.3.3. Optimized Design Performance Analysis

Although the optimized connecting rod exhibits a significant reduction in material area, the normalized stiffness (stiffness-to-mass ratio) of the original model remained higher than that of the optimized geometry. Several reasons may explain this outcome. First, the large circular end-regions (large end and small end) contribute substantially to the total mass while contributing relatively little to the bending stiffness of the mid-span web; therefore, removing mass primarily from interior regions can reduce absolute stiffness more than expected when these heavy end-regions remain unchanged. Second, the original design may already be close to an efficient topology for the simplified loading considered here — the Von Mises field of the baseline part shows a smooth stress distribution, suggesting a near-optimal material layout. Even though the optimized model did not achieve a higher normalized stiffness than the original design, the material reduction still provides potential advantages. A lighter connecting rod reduces the inertia forces within the engine mechanism, which can improve dynamic performance, lower fuel consumption, and decrease mechanical stresses on other components. These aspects, although not captured in the present static simulations, highlight the practical benefits of mass reduction beyond stiffness considerations alone.

5. Conclusions

This dissertation explored the application of meshless methods, particularly the Radial Point Interpolation Method (RPIM) and the Natural Neighbour Radial Point Interpolation Method (NNRPIM), combined with topology optimization techniques for additive manufacturing. The primary objectives were to investigate the advantages of meshless methods over traditional finite element methods (FEM) and evaluate their effectiveness in structural optimization.

5.1. General Conclusions and Remarks

The convergence study shows that all numerical methods here presented can achieve accurate results, validating their reliability for structural analysis and optimization. In this study RPIM and NNRPIM showed higher convergence rates than FEM, suggesting that meshless approaches can provide more efficient solutions in terms of iteration requirements.

The convergence study demonstrated that all three numerical methods can produce accurate results, validating their reliability to perform static analysis. RPIM and NNRPIM showed higher convergence rates than FEM, suggesting that meshless methods can under certain conditions reach more accurate results with less refinement.

In the benchmark problems, all methods were able to generate geometries close to the reference solution. The results highlighted the influence of mesh refinement and decrease ratio on the quality of the solutions, showing that both parameters strongly affect the clarity and convergence of the optimized geometries. Some with coarse meshes were able to generate the general features of the reference solution, although with less resolution and clarity.

The industrial case study of the engine rod optimization showed the applicability of the methodology in real word problems. The results highlighted the importance and sensitivity of the domain definition. The optimized geometry obtained from the data, despite a significant reduction in mass, did not achieve a higher specific stiffness. This outcome suggests that the original design may already be close to an efficient solution.

Overall, the work shows that meshless methods such as RPIM and NNRPIM can be a reliable alternative to the traditional FEM in structural optimization with the potential to deliver competitive results. However, their robustness still requires further assessment and should be tested more extensively.

5.2. Limitations

Throughout the development of this work, some limitations were faced that affected the scope and depth of the study. One of these limitations was related to the available hardware, which restricted the size and complexity of the problems that could be addressed. Another limitation concerns the software that was utilized. All simulations were performed using FEMAS, a research-oriented code developed in MATLAB. Although FEMAS provides accurate solutions, it is not optimized for computational speed. As a result, the computational times are higher than those expected in a commercial software.

5.3. Future Works

The work here presented opens several paths for future research. A natural extension of this work would be exploring other combinations of numerical methods with different optimization algorithms. Another direction would be to extend the study to three dimensional geometries, since this work was limited only to 2D geometries. This would allow for a more realistic evaluation of the methods and make the simulations more relevant to partial engineering and industrial applications. In this work only 5% and 10% decrease ratios were tested. Testing a wider range of decrease rations would also help clarify the influence of this parameter on the optimized designs. An experimental validation would also be a valuable complement to this work; the obtained geometries could be produced using additive manufacturing processes and afterward be tested to verify and validated the values obtained with the numerical predictions. Another aspect that could be explored in future works is the computational required for each method, this analysis could provide valuable insights into which method is more demanding on hardware and help guide the selection of the most efficient approach.

References

[1] 'Webofscience'. [Online]. Available: https://www.webofscience.com

[2] L. B. Lucy, 'A numerical approach to the testing of the fission hypothesis', *Astron. Journal, vol. 82, Dec. 1977, p. 1013-1024.*, vol. 82, pp. 1013–1024, 1977.

[3] R. A. Gingold and J. J. Monaghan, 'Smoothed particle hydrodynamics: theory and application to non-spherical stars', *Mon. Not. R. Astron. Soc.*, vol. 181, no. 3, pp. 375–389, 1977.

[4] Y. Chen, J. Lee, and A. Eskandarian, *Meshless Methods in Solid Mechanics*. Springer, 2006.

[5] V. G. Patel and N. V. Rachchh, 'Meshless method - Review on recent developments', *Mater. Today Proc.*, vol. 26, pp. 1598–1603, 2019, doi: 10.1016/j.matpr.2020.02.328.

[6] T. Belytschko, Y. Y. Lu, and L. Gu, 'Element-Free Galerkin Methods', *Int. J. Numer. Methods Engineeting*, vol. 37, no. April 1993, pp. 229–256, 1994, doi: 10.1007/978-3-030-06173-9_4.

[7] E. J. Kansa, 'Multiquadrics—A scattered data approximation scheme with applications to computational fluid-dynamics—I surface approximations and partial derivative estimates', *Comput. Math. with Appl.*, vol. 19, no. 8, pp. 127–145, 1990, doi: https://doi.org/10.1016/0898-1221(90)90270-T.

[8] E. J. Kansa, 'Multiquadrics—A scattered data approximation scheme with applications to computational fluid-dynamics—II solutions to parabolic, hyperbolic and elliptic partial differential equations', *Comput. Math. with Appl.*, vol. 19, no. 8, pp. 147–161, 1990, doi: https://doi.org/10.1016/0898-1221(90)90271-K.

[9] S. N. Atluri and T. Zhu, 'A new meshless local Petrov-Galerkin (MLPG) approach in computational mechanics', *Comput. Mech.*, vol. 22, no. 2, pp. 117–127, 1998.

[10] N. Aluru, 'A point collocation method based on reproducing kernel approximations', *Int. J. Numer. Methods Eng.*, vol. 47, no. 6, pp. 1083–1121, 2000.

[11] J. G. Wang and G. R. Liu, 'A point interpolation meshless method based on radial basis functions', *Int. J. Numer. Methods Eng.*, vol. 54, no. 11, pp. 1623–1648, 2002, doi: 10.1002/nme.489.

[12] G. R. Liu and Y. T. Gu, 'A point interpolation method for two-dimensional solids', *Int. J. Numer. Methods Eng.*, vol. 50, no. 4, pp. 937–951, 2001, doi: 10.1002/1097-0207(20010210)50:4<937::AID-NME62>3.0.CO;2-X.

[13] G. R. Liu, G. Y. Zhang, Y. T. Gu, and Y. Y. Wang, 'A meshfree radial point interpolation method (RPIM) for three-dimensional solids', *Comput. Mech.*, vol. 36, no. 6, pp. 421–430, 2005, doi: 10.1007/s00466-005-0657-6.

[14] L. M. J. S. Dinis, R. M. Natal Jorge, and J. Belinha, 'Analysis of 3D solids using the natural neighbour radial point interpolation method', *Comput. Methods Appl. Mech. Eng.*, vol. 196, no. 13–16, pp. 2009–2028, 2007, doi: 10.1016/j.cma.2006.11.002.

[15] V. GM, 'Nouvelles applications des paramètres continus à la théorie des formes quadratiques. Deuxième mémoire. Recherches sur les paralléllοèdres primitifs.', *J. für die reine und Angew. Math.*, vol. 134, pp. 198–287, 1908, doi:

10.1515/crll.1908.134.198.

[16] D. B, ‘Sur la sphére vide. A la memoire de Georges Voronoï. Izv. Akad. Nauk SSSR’, *Otd. Mat. i Estestv. Nauk*, vol. 7, pp. 793–800, 1934.

[17] G. R. Liu and Y. T. Gu, *An introduction to meshfree methods and their programming*. Springer, 2005. doi: 10.1007/1-4020-3468-7.

[18] J. Belinha, *Meshless Methods in Biomechanics - Bone Tissue Remodelling Analysis*. 2014. doi: 10.1007/978-3-319-06400-0.

[19] J. Belinha, ‘Extending the Natural Neighbour Radial Point Interpolation Meshless Method to the Multiscale Analysis of Sandwich Beams with Polyurethane Foam Core’, *Appl. Sci.*, vol. 14, no. 20, p. 9214, Oct. 2024, doi: 10.3390/app14209214.

[20] B. Nayroles, G. Touzot, and P. Villon, ‘Generalizing the finite element method: Diffuse approximation and diffuse elements’, *Comput. Mech.*, vol. 10, no. 5, pp. 307–318, 1992, doi: 10.1007/BF00364252.

[21] J. Belinha, ‘Multiscale Analysis of Sandwich Beams with Polyurethane Foam Core: A Comparative Study of Finite Element Methods and Radial Point Interpolation Method’, *Materials (Basel).*, vol. 17, no. 18, 2024, doi: 10.3390/ma17184466.

[22] J. G. Wang and G. R. Liu, ‘On the optimal shape parameters of radial basis functions used for 2-D meshless methods’, *Comput. Methods Appl. Mech. Eng.*, vol. 191, no. 23–24, pp. 2611–2630, 2002, doi: 10.1016/S0045-7825(01)00419-4.

[23] R. L. Hardy, ‘Theory and applications of the multiquadric-biharmonic method 20 years of discovery 1968-1988’, *Comput. Math. with Appl.*, vol. 19, no. 8–9, pp. 163–208, 1990, doi: 10.1016/0898-1221(90)90272-L.

[24] O. C. Zienkiewicz and R. L. Taylor, *The finite element method: solid mechanics*, vol. 2. Butterworth-heinemann, 2000.

[25] M. P. Bendsoe and O. Sigmund, *Topology optimization: theory, methods, and applications*. Springer Science \& Business Media, 2013.

[26] J. D. Deaton and R. V Grandhi, ‘A survey of structural and multidisciplinary continuum topology optimization: post 2000’, *Struct. Multidiscip. Optim.*, vol. 49, pp. 1–38, 2014.

[27] X. Huang and M. Xie, *Evolutionary topology optimization of continuum structures: methods and applications*. John Wiley \& Sons, 2010.

[28] J.-H. Zhu, W.-H. Zhang, and L. Xia, ‘Topology optimization in aircraft and aerospace structures design’, *Arch. Comput. methods Eng.*, vol. 23, pp. 595–622, 2016.

[29] L. Xia and P. Breitkopf, ‘Recent advances on topology optimization of multiscale nonlinear structures’, *Arch. Comput. Methods Eng.*, vol. 24, pp. 227–249, 2017.

[30] D. J. Munk, G. A. Vio, and G. P. Steven, ‘Topology and shape optimization methods using evolutionary algorithms: a review’, *Struct. Multidiscip. Optim.*, vol. 52, no. 3, pp. 613–631, 2015, doi: 10.1007/s00158-015-1261-9.

[31] A. G. M. Michell, ‘LVIII. The limits of economy of material in frame-structures ’, *London, Edinburgh, Dublin Philos. Mag. J. Sci.*, vol. 8, no. 47, pp. 589–597, Nov. 1904, doi: 10.1080/14786440409463229.

[32] R. Hill, *The Mathematical Theory of Plasticity*. in Oxford classic texts in the physical sciences. Clarendon Press, 1998.

[33] J. Heyman, ‘Plastic design of beams and plane frames for minimum material consumption’, *Q. Appl. Math.*, vol. 8, pp. 373–381, 1951.

[34] J. Heyman and W. Prager, ‘Automatic minimum weight design of steel frames’, *J. Franklin Inst.*, vol. 266, no. 5, pp. 339–364, 1958, doi: https://doi.org/10.1016/0016-0032(58)90306-5.

[35] J. D. Foulkes, ‘The minimum-weight design of structural frames’, *Proc. R. Soc. London. Ser. A. Math. Phys. Sci.*, vol. 223, pp. 482–494, 1954.

[36] D. C. Drucker and R. T. Shield, ‘Design for Minimum Weight.’, 1956.

[37] R. K. LIVESLEY, ‘THE AUTOMATIC DESIGN OF STRUCTURAL FRAMES’, *Q. J. Mech. Appl. Math.*, vol. 9, no. 3, pp. 257–278, Jan. 1956, doi: 10.1093/qjmam/9.3.257.

[38] W. Prager, ‘Minimum-Weight Design of a Portal Frame’, *J. Eng. Mech. Div.*, vol. 82, no. 4, pp. 1010–1073, 1956, doi: 10.1061/JMCEA3.0000010.

[39] W. Prager and R. T. Shield, ‘Minimum weight design of circular plates under arbitrary loading’, *Zeitschrift für Angew. Math. und Phys. ZAMP*, vol. 10, no. 4, pp. 421–426, 1959, doi: 10.1007/BF01601046.

[40] E. T. Onat, W. Schumann, and R. T. Shield, ‘Design of circular plates for minimum weight’, *Zeitschrift für Angew. Math. und Phys. ZAMP*, vol. 8, no. 6, pp. 485–499, 1957, doi: 10.1007/BF01600564.

[41] W. S. Hemp, ‘Theory of structural design’, *Coll. Aeronaut. Rep.*, 1958.

[42] A. S. L. Chan, *The Design of Michell Optimum Structures*. in ARC-22596. College of Aeronautics, 1960.

[43] H. L. Cox, *The Design of Structures of Least Weight*. in International series of monographs on aeronautics and astronautics: Solid and structural mechanics. Pergamon Press, 1965.

[44] P. V Marcal and W. Prager, ‘A method of optimal plastic design’, *J. Mécanique*, vol. 3, no. 4, pp. 509–530, 1964.

[45] W. Prager and R. T. Shield, ‘A General Theory of Optimal Plastic Design’, *J. Appl. Mech.*, vol. 34, no. 1, pp. 184–186, 1967, doi: 10.1115/1.3607621.

[46] G. B. Dantzig, *Linear Programming and Extensions*. Princeton: Princeton University Press, 1963. doi: doi:10.1515/9781400884179.

[47] M. P. Bendsøe and N. Kikuchi, ‘Generating optimal topologies in structural design using a homogenization method’, *Comput. Methods Appl. Mech. Eng.*, vol. 71, no. 2, pp. 197–224, 1988, doi: https://doi.org/10.1016/0045-7825(88)90086-2.

[48] M. P. Bendsøe, ‘Optimal shape design as a material distribution problem’, *Struct. Optim.*, vol. 1, no. 4, pp. 193–202, 1989, doi: 10.1007/BF01650949.

[49] M. Zhou and G. I. N. Rozvany, ‘The COC algorithm, Part II: Topological, geometrical and generalized shape optimization’, *Comput. Methods Appl. Mech. Eng.*, vol. 89, no. 1–3, pp. 309–336, 1991.

[50] G. I. N. Rozvany and M. Zhou, ‘Applications of the COC algorithm in layout optimization’, in *Engineering Optimization in Design Processes: Proceedings of the International Conference Karlsruhe Nuclear Research Center, Germany September 3--4, 1990*, 1991, pp. 59–70.

[51] R. Balamurugan, C. V Ramakrishnan, and N. Singh, 'Performance evaluation of a two stage adaptive genetic algorithm (TSAGA) in structural topology optimization', *Appl. Soft Comput.*, vol. 8, no. 4, pp. 1607–1624, 2008.

[52] R. Balamurugan, C. V Ramakrishnan, and N. Swaminathan, 'A two phase approach based on skeleton convergence and geometric variables for topology optimization using genetic algorithm', *Struct. Multidiscip. Optim.*, vol. 43, pp. 381–404, 2011.

[53] C. Jain and A. Saxena, 'An improved material-mask overlay strategy for topology optimization of structures and compliant mechanisms', 2010.

[54] J. F. A. Madeira, H. L. Pina, and H. C. Rodrigues, 'GA topology optimization using random keys for tree encoding of structures', *Struct. Multidiscip. Optim.*, vol. 40, pp. 227–240, 2010.

[55] G.-C. Luh and C.-H. Chueh, 'Multi-modal topological optimization of structure using immune algorithm', *Comput. Methods Appl. Mech. Eng.*, vol. 193, no. 36–38, pp. 4035–4055, 2004.

[56] M. P. Bendsøe and O. Sigmund, 'TOPOLOGY OPTIMIZATION', in *Optimization of Structural and Mechanical Systems*, WORLD SCIENTIFIC, 2007, pp. 161–194. doi: doi:10.1142/9789812779670_0006.

[57] Y. M. Xie and G. P. Steven, 'A simple evolutionary procedure for structural optimization', *Comput. Struct.*, vol. 49, no. 5, pp. 885–896, 1993, doi: https://doi.org/10.1016/0045-7949(93)90035-C.

[58] C. B. Zhao, G. P. Steven, and Y. M. Xie, 'Evolutionary optimization of maximizing the difference between two natural frequencies of a vibrating structure', *Struct. Optim.*, vol. 13, no. 2, pp. 148–154, 1997, doi: 10.1007/BF01199234.

[59] D. Manickarajah, Y. M. Xie, and G. P. Steven, 'An evolutionary method for optimization of plate buckling resistance', *Finite Elem. Anal. Des.*, vol. 29, no. 3–4, pp. 205–230, 1998.

[60] Y. M. Xie, G. P. Steven, Y. M. Xie, and G. P. Steven, *Basic evolutionary structural optimization*. Springer, 1997.

[61] Q. Li, G. P. Steven, Y. M. Xie, and O. M. Querin, 'Evolutionary topology optimization for temperature reduction of heat conducting fields', *Int. J. Heat Mass Transf.*, vol. 47, no. 23, pp. 5071–5083, 2004.

[62] K. A. Proos, G. P. Steven, O. M. Querin, and Y. M. Xie, 'Stiffness and inertia multicriteria evolutionary structural optimisation', *Eng. Comput.*, vol. 18, no. 7, pp. 1031–1054, 2001.

[63] O. M. Querin, 'Evolutionary structural optimisation: stress based formulation and implementation', University of Sydney Sydney, Australia, 1997.

[64] Q. Li, G. P. Steven, and Y. M. Xie, 'On equivalence between stress criterion and stiffness criterion in evolutionary structural optimization', *Struct. Optim.*, vol. 18, pp. 67–73, 1999.

[65] J. J. McKEOWN, 'A note on the equivalence between maximum stiffness and maximum strength trusses', *Eng. Optim.*, vol. 29, no. 1–4, pp. 443–456, 1997.

[66] X. Huang and Y. M. Xie, 'Convergent and mesh-independent solutions for the bi-directional evolutionary structural optimization method', *Finite Elem. Anal. Des.*, vol.

43, no. 14, pp. 1039–1049, 2007, doi: https://doi.org/10.1016/j.finel.2007.06.006.

[67] X. Y. Yang, Y. M. Xie, G. P. Steven, and O. M. Querin, 'Bi-directional evolutionary method for stiffness optimisation', *7th AIAA/USAF/NASA/ISSMO Symp. Multidiscip. Anal. Optim.*, vol. 37, no. 11, pp. 1449–1457, 1998, doi: 10.2514/6.1998-4900.

[68] L. Xia, Q. Xia, X. Huang, and Y. M. Xie, 'Bi-directional Evolutionary Structural Optimization on Advanced Structures and Materials: A Comprehensive Review', *Arch. Comput. Methods Eng.*, vol. 25, no. 2, pp. 437–478, 2018, doi: 10.1007/s11831-016-9203-2.

[69] Q. Li, G. P. Steven, and Y. M. Xie, 'A simple checkerboard suppression algorithm for evolutionary structural optimization', *Struct. Multidiscip. Optim.*, vol. 22, pp. 230–239, 2001.

[70] X.-Y. Yang, Y.-M. Xie, J.-S. Liu, G. T. Parks, and P. J. Clarkson, 'Perimeter control in the bidirectional evolutionary optimization method', *Struct. Multidiscip. Optim.*, vol. 24, pp. 430–440, 2002.

[71] H. Kim, O. M. Querin, G. P. Steven, and Y. M. Xie, 'A method for varying the number of cavities in an optimized topology using evolutionary structural optimization', *Struct. Multidiscip. Optim.*, vol. 19, pp. 140–147, 2000.

[72] H. Kim, O. M. Querin, G. P. Steven, and Y. M. Xie, 'Determination of an optimal topology with a predefined number of cavities', *AIAA J.*, vol. 40, no. 4, pp. 739–744, 2002.

[73] H. Kim, M. J. Garcia, O. M. Querin, G. P. Steven, and Y. Xie, 'Introduction of fixed grid in evolutionary structural optimisation', *Eng. Comput.*, vol. 17, no. 4, pp. 427–439, 2000.

[74] H. Kim, O. M. Querin, G. P. Steven, and Y. M. Xie, 'Improving efficiency of evolutionary structural optimization by implementing fixed grid mesh', *Struct. Multidiscip. Optim.*, vol. 24, pp. 441–448, 2002.

[75] B. Yunfei, C. Ming, and L. Yongyao, 'Structural Topology Optimization for a Robot Upper Arm Based on SIMP Method', in *Advances in Reconfigurable Mechanisms and Robots II*, X. Ding, X. Kong, and J. S. Dai, Eds., Cham: Springer International Publishing, 2016, pp. 725–733.

[76] Y. Ding, 'Shape optimization of structures: a literature survey', *Comput. Struct.*, vol. 24, no. 6, pp. 985–1004, 1986, doi: https://doi.org/10.1016/0045-7949(86)90307-X.

[77] R. T. Haftka and R. V Grandhi, 'Structural shape optimization—A survey', *Comput. Methods Appl. Mech. Eng.*, vol. 57, no. 1, pp. 91–106, 1986, doi: https://doi.org/10.1016/0045-7825(86)90072-1.

[78] O. C. ZIENKIEWICZ, 'Shape optimization and sequential linear programming', *Optim. Struct. Des. Appl.*, 1973.

[79] M. H. Imam, 'Three-dimensional shape optimization', *Int. J. Numer. Methods Eng.*, vol. 18, no. 5, pp. 661–673, 1982, doi: https://doi.org/10.1002/nme.1620180504.

[80] V. Braibant and C. Fleury, 'Shape optimal design using B-splines', *Comput. Methods Appl. Mech. Eng.*, vol. 44, no. 3, pp. 247–267, 1984, doi: https://doi.org/10.1016/0045-7825(84)90132-4.

[81] M. E. Botkin, 'Shape Optimization of Plate and Shell Structures', *AIAA J.*, vol. 20, no. 2, pp. 268–273, 1982, doi: 10.2514/3.51074.

[82] W. Shu-Yu, S. Yanbing, and R. H. Gallagher, 'Sensitivity analysis in shape optimization of continuum structures', *Comput. \& Struct.*, vol. 20, no. 5, pp. 855–867, 1985.

[83] S. S. Bhavikatti and C. V Ramakrishnan, 'Optimum shape design of shoulder fillets in tension bars and T-heads', *Int. J. Mech. Sci.*, vol. 21, no. 1, pp. 29–39, 1979, doi: https://doi.org/10.1016/0020-7403(79)90074-2.

[84] S. S. Bhavikatti and C. V Ramakrishnan, 'Optimum shape design of rotating disks', *Comput. Struct.*, vol. 11, no. 5, pp. 397–401, 1980, doi: https://doi.org/10.1016/0045-7949(80)90105-4.

[85] B. Prasad and J. F. Emerson, 'Optimal structural remodeling of multi-objective systems', *Comput. Struct.*, vol. 18, no. 4, pp. 619–628, 1984, doi: https://doi.org/10.1016/0045-7949(84)90007-5.

[86] W. Annicchiarico and M. Cerrolaza, 'Finite elements, genetic algorithms and β-splines: a combined technique for shape optimization', *Finite Elem. Anal. Des.*, vol. 33, no. 2, pp. 125–141, 1999, doi: https://doi.org/10.1016/S0168-874X(99)00030-X.

[87] M. Cerrolaza, W. Annicchiarico, and M. Martinez, 'Optimization of 2D boundary element models using β-splines and genetic algorithms', *Eng. Anal. Bound. Elem.*, vol. 24, no. 5, pp. 427–440, 2000, doi: https://doi.org/10.1016/S0955-7997(00)00006-0.

[88] A. D. Belegundu and S. D. Rajan, 'A shape optimization approach based on natural design variables and shape functions', *Comput. Methods Appl. Mech. Eng.*, vol. 66, no. 1, pp. 87–106, 1988, doi: https://doi.org/10.1016/0045-7825(88)90061-8.

[89] D. A. Tortorelli, 'A Geometric Representation Scheme Suitable for Shape Optimization* †', *Mech. Struct. Mach.*, vol. 21, no. 1, pp. 95–121, 1993, doi: 10.1080/08905459308905182.

[90] E. Stavropoulou, M. Hojjat, and K.-U. Bletzinger, 'In-plane mesh regularization for node-based shape optimization problems', *Comput. Methods Appl. Mech. Eng.*, vol. 275, pp. 39–54, 2014, doi: https://doi.org/10.1016/j.cma.2014.02.013.

[91] M. Firl, R. Wüchner, and K.-U. Bletzinger, 'Regularization of shape optimization problems using FE-based parametrization', *Struct. Multidiscip. Optim.*, vol. 47, no. 4, pp. 507–521, 2013, doi: 10.1007/s00158-012-0843-z.

[92] J. Linhard and K.-U. Bletzinger, '"Tracing" the Equilibrium — Recent Advances in Numerical Form Finding', *Int. J. Sp. Struct.*, vol. 25, no. 2, pp. 107–116, 2010, doi: 10.1260/0266-3511.25.2.107.

[93] M. Hojjat, E. Stavropoulou, and K.-U. Bletzinger, 'The Vertex Morphing method for node-based shape optimization', *Comput. Methods Appl. Mech. Eng.*, vol. 268, pp. 494–513, 2014, doi: https://doi.org/10.1016/j.cma.2013.10.015.

[94] H. Azegami, 'Solution to Domain Optimization Problems', *Trans. Japan Soc. Mech. Eng. Ser. A*, vol. 60, no. 574, pp. 1479–1486, 1994, doi: 10.1299/kikaia.60.1479.

[95] B. D. Upadhyay, S. S. Sonigra, and S. D. Daxini, 'Numerical analysis perspective in structural shape optimization: A review post 2000', *Adv. Eng. Softw.*, vol. 155, no. January, p. 102992, 2021, doi: 10.1016/j.advengsoft.2021.102992.

[96] S. D. Daxini and J. M. Prajapati, 'Numerical shape optimization based on meshless method and stochastic optimization technique', *Eng. Comput.*, vol. 36, no. 2, pp. 565–586, 2020, doi: 10.1007/s00366-019-00714-3.

[97] D. Lacroix and P. Bouillard, ‘Improved sensitivity analysis by a coupled FE–EFG method’, *Comput. Struct.*, vol. 81, no. 26, pp. 2431–2439, 2003, doi: https://doi.org/10.1016/S0045-7949(03)00316-X.

[98] J. Zheng, S. Y. Long, and Y. B. Xiong, ‘The topology optimization design of the continuum structure based on the meshless numerical technique’, *Jisuan Lixue Xuebao/Chinese J. Comput. Mech.*, vol. 27, no. 2, pp. 232–237, 2010.

[99] S.-J. Lee, C.-K. Lee, and J.-E. Bae, ‘Evolution of 2D Truss Structures using Topology Optimization Technique with Meshless Method’, *Proc. Int. Assoc. Shell Spat. Struct. Symp.*, no. March, pp. 1058–1065, 2009.

[100] D. C. Gonçalves, J. D. F. Lopes, R. D. S. G. Campilho, and J. Belinha, ‘Topology optimization using a natural neighbour meshless method combined with a bi-directional evolutionary algorithm’, *Math. Comput. Simul.*, vol. 194, pp. 308–328, 2022, doi: 10.1016/j.matcom.2021.11.021.

Declaration of Integrity

I declare that I conducted this academic work with integrity. I did not plagiarize or apply any form of misuse of information or falsification of results throughout the process that led to its preparation. I declare that the work presented in this document is original and my own and has not previously been used for any other purpose. I further declare that I am fully aware of the Code of Ethical Conduct of P.PORTO, ISEP.

NAME: João Tiago Tomás Oliveira

Porto, (September 14, 2025)